

# Design of an accurate and low cost 4D foot scanner for podiatrists

Master thesis by Felix Kwa  
August, 2021

# Design of an accurate and low cost 4D foot scanner for podiatrists

August, 2021

MSc Integrated Product Design  
Medisign Specialization  
Faculty of Industrial Design Engineering  
Delft University of Technology

**Author**

Felix Kwa  
felixkwa@gmail.com

**Supervisory team**

Chair: Dr. Y. (Wolf) Song  
Associate professor Mechatronic Design  
Industrial Design Engineering  
Delft University of Technology

Mentor: Dr. T. Huysmans  
Assistant professor Digital Human Modelling  
Industrial Design Engineering  
Delft University of Technology

# I . Preface

This thesis concludes my studies at the TU Delft. It has been quite the journey, where I had the opportunity to develop myself in ways that I did not expect when I first started my bachelor's in Industrial Design Engineering. I am excited about the outcome of this project and truly blessed that I can share this. I would like to thank everyone who has supported me during this project.

Firstly, I would like to thank my supervisory team. Wolf, I am grateful for the opportunities you have given me in the past year, and your time, energy and banter. Also, for providing me with this incredible project. Toon, thank you for your enthusiasm, guidance, and valuable insights throughout the project. It has been inspiring to present my work to you. Lastly, thanks to the unofficial member of the team, Farzam. I appreciate the energy you have put into my project and all the help you have offered me. You have been a great support and I wish you all the best in your PhD and after.

Also, thanks to Willemijn Elkhuiizen, Lars Fuit, Jeep Alkema, and Wybren ten Cate. For taking time to talk and brainstorm with me, and providing me with valuable insights in the development of this project.

A special thanks to my family. Papa and mama in particular, thank you for providing me with the opportunity to freely develop myself and your unconditional support in everything that I have done. I am forever grateful. Dennis and Lesley, thank you for always cheering me on. Susan, thank you for always being there for me, supporting me through my ups and downs, and inspiring me to excel.

Lastly, I want to thank all my friends for putting up with me in the past years. The numerous hours and late nights of studying together, taking coffee breaks, having inspirational brainstorm sessions, and hanging out together have made my studies an unforgettable time in my life.

I hope you enjoy reading my thesis and that it can contribute to the development of greater things.

**Felix Kwa**  
Delft, August 2021

## II. Abstract

This thesis describes the design and development of an accurate and low cost 4D foot scanner in the context of podiatry. The intention is to make a first step towards the development of an affordable 4D foot scanner with commercial grade performance at a low cost, using commodity hardware. By doing so, 4D scanning can hopefully become more accessible to the general public, and accelerate the development and adoption of ultra personalized footwear and digital manufacturing in healthcare.

Podiatrists focus on the treatment of physical conditions in the lower regions of the human body, which are often related to foot conditions. Personalized footwear solutions (e.g. orthotics) are widely used to relieve a patient of such conditions, which are primarily designed based on static 3D scanning data of the foot. With additional input of motion analyses and professional experience, a podiatrist can adjust the design of an orthotic to fit the patient.

However, the change in foot measurements during different phases of the gait cycle are not accounted for in the design of these personalized solutions, which could vary up to 8 mm. With 4D foot scanning (dynamic 3D scanning), podiatrists will be able to observe and acquire data of the dynamic morphology of a foot during the gait cycle. This should allow the design and development of truly personalized orthotics that are able to support a patient during the entire gait cycle.

To support this vision, a proof of concept of a 4D foot scanner has been developed. The presented proof of concept iterates over a previously built 4D foot scanner (Vidmar, 2020). The proof of concept includes: an optimized embodiment for improved scanning quality and scanning consistency, a trigger system to improve the human-computer interaction of the scanner, and a scalable camera configuration for up to 9 cameras.

The hardware performance of the scanner in combination with the newly designed data acquisition pipeline has been evaluated in terms of acquisition consistency, speed, and memory usage. The outcome is that the scanner is able to manage dynamic data acquisition with a camera configuration of 9. Also, for a camera configuration of 7, the scanner shows a linear trend in memory consumption, acquired frames, and acquisition speeds, which suggests that performance of the scanner is predictable and constant for this configuration. More elaborate analyses should give better insights into the long time performance of the scanner for different camera configurations.

The evaluation of the quality of both static and dynamic scanning data has been done with the implementation of nonrigid ICP. The accuracy of the scanner showed a minimal accuracy error of 2.274 mm. Compared with international 3D scanning standards (minimum accuracy error of 2 mm), the performance of the scanner is considered as a desirable outcome for this graduation project.

### III. Glossary

This glossary contains definitions of the terms used in this report to elaborate on the meaning and context of these otherwise generic terms.

- **Ankle-foot orthotic** = A brace to provide correction and/or support to the foot and ankle.
- **AFO** = See Ankle-foot orthotic.
- **Data preprocessing** = Removing noisy depth data from the raw point cloud data, resulting in a clean point cloud representing the desired object.
- **Dorsal surface** = Instep of the foot.
- **Elements** = Standardized orthotic components that are used in the design of (personalized) orthotics.
- **Foot orthoses** = Commonly known as (foot) orthotics. See orthotics.
- **FPS** = Frames per second.
- **Frameset** = A data object that contains data on a particular frame of a RealSense camera, including the RGB and depth frames.
- **Gait** = The way a person walks.
- **ICP** = Iterative Closest Point Algorithm (Chen & Medioni, 1991; Besl & McKay, 1992).
- **Insoles** = A sole with supporting elements with the goal of improving the gait of a person. It is also used to provide more support in the gait and to relieve pain.
- **Internal memory** = RAM memory.
- **User** = Podiatrist.
- **Operator** = Person who operates the 4D scanner. It is likely that this is the podiatrist. It could also be a trained specialist that operates the scanner, or a person who uses the scanner for research purposes.
- **Orthotics** = Insole that is put in the patient's shoe, used in podiatric treatment.
- **Patient** = A person who is in therapy at a podiatrist.
- **Plantar surface** = Bottom/sole of the foot.
- **Sham** = Insoles with a placebo effect and provide no biomechanical or neurological effect.
- **Sensor** = An image sensor that is embedded in an Intel RealSense camera. This could be either the RGB sensor for colored images, or the stereo depth sensors for depth images.

# Table of contents

<b>I.</b>	<b>Preface</b>	<b>4</b>						
<b>II.</b>	<b>Abstract</b>	<b>6</b>						
<b>III.</b>	<b>Glossary</b>	<b>8</b>						
<b>Discover</b>								
<b>01.</b>	<b>Introduction</b>	<b>12</b>						
<b>02.</b>	<b>Assignment &amp; project scope</b>	<b>14</b>						
<b>Define</b>								
<b>06.</b>	<b>Problem definition</b>	<b>52</b>						
<b>07.</b>	<b>Design challenges</b>	<b>54</b>						
7.1	Camera connectivity	56						
7.2	Synchronized 4D data acquisition	56						
7.3	Scanning pipeline	56						
7.4	Embodiment optimization	57						
<b>08.</b>	<b>Stakeholders</b>	<b>60</b>						
<b>09.</b>	<b>List of requirements</b>	<b>62</b>						
<b>Development</b>								
<b>10.</b>	<b>4D foot scanning concepts</b>	<b>68</b>						
10.1	Concepts	70						
10.2	Costs	71						
10.3	Conclusion	71						
<b>11.</b>	<b>Prototyping showcase</b>	<b>72</b>						
11.1	System configuration	75						
11.2	Cameras	75						
11.3	Scanning plate	78						
11.4	Custom camera mount	81						
11.5	Trigger system (Human Computer Interaction)	83						
11.5.1	Functionality	83						
11.5.2	Positioning	87						
11.6	External lighting	89						
11.7	Pricing	91						
<b>12.</b>	<b>Data acquisition</b>	<b>92</b>						
12.1	Data acquisition pipeline	94						
12.2	Acquisition performance analyses	97						
12.2.1	Frame analysis	97						
12.2.2	Memory analysis	98						
12.2.3	Dynamic acquisition time	100						
12.3	Conclusions	101						
12.3.1	Frame analysis	101						
12.3.2	Memory analysis	101						
<b>13.</b>	<b>Data processing</b>	<b>92</b>						
13.1	Data processing pipeline	104						
13.1.1	From raw data to point cloud	104						
13.1.2	Preprocessing data	104						
13.1.3	Rough alignment	105						
13.1.4	Fine point cloud registration	106						
13.2	Result	107						
13.2.1	Rigid ICP	107						
13.2.2	Nonrigid ICP	108						
13.2.3	Preliminary accuracy validation	109						
13.3	Conclusions	110						
<b>14.</b>	<b>Conclusion &amp; recommendations</b>	<b>112</b>						
14.1	System optimization	114						
14.1.1	Hybrid camera setup	114						
14.1.2	Camera mounts manufacturing	114						
14.2	Optimized data acquisition and processing	114						
14.2.1	Asynchronous data acquisition	114						
14.2.2	Optimized data processing	115						
14.3	Automatic extrinsic camera calibration proposal	115						
14.4	Accuracy validation of the scanner	116						
<b>Appendices</b>								
<b>A.</b>	<b>Project structure</b>	<b>124</b>						
<b>B.</b>	<b>Vidmar's prototype (2020) identification</b>	<b>126</b>						
<b>C.</b>	<b>List of requirements</b>	<b>128</b>						
<b>D.</b>	<b>4D foot scanning concepts</b>	<b>130</b>						
<b>E.</b>	<b>Prototyping showcase</b>	<b>132</b>						
<b>F.</b>	<b>Data acquisition evaluation</b>	<b>145</b>						
<b>G.</b>	<b>Data processing</b>	<b>148</b>						
<b>H.</b>	<b>Camera calibration proposal</b>	<b>148</b>						

## 01. Introduction

Modern footwear is designed for the general population and is currently based on static lasts which assume that the foot consists of rigid segments. This representation does not take the dynamic morphology of the foot into account, which is especially existent in a weight bearing state during the gait cycle. Several studies show benefits in footwear comfort, such as an increased running performance (Luo et al., 2009), the risk reduction of movement-related injury (Mündermann et al., 2001), and comfort being a primary factor for consumers of selecting footwear (Martínez-Martínez et al., 2017). To accommodate for an improved fit, many people opt for the use of additional foot orthoses. This is not only useful for increased comfort, but also to correct one's gait and posture. However, the current development of these orthotics present challenges, originating in the data acquisition of the feet.

As presented by Barisch-Fritz et al. (2014), current methods for retrieving information about feet are based on markers, goniometers, plantar pressure analysis or interpretation, imprints or static 3D scans. These methods have a limited view on the dynamic foot morphology and therefore have a limited applicability. Telfer et al. (2012) shows that it is difficult to reproduce consistent foot orthotics with similar quality due to inconsistent measurement of the medial arch height. Also, due to the overall dynamic morphology of the foot, the actual volume of the foot and the foot orthotics design does not match, with an average difference in volume of more than 20 %. As Boppana and Anderson (2020) presented, a detailed understanding of dynamic foot morphology (4D foot scanning) can enable the design of more comfortable and better fitting footwear, which could also be applied in the development of foot orthoses (insoles). This would be the next development in foot scanning after 3D foot scanning.

The use of 3D scanners is already becoming a general used technology for podiatrists, with prices ranging between €3.500 and €30.000 (Telfer & Woodburn, 2010; Podonova, 2021; Capron podology, personal communication, 11 May, 2021), with varying performance in accuracy. A 4D foot scanner has been developed by 3dMD; it is considered a research prototype, which makes it highly priced and unsuitable for commercial use. These factors prevent the adoption of general use of 4D scanning by podiatrists and therefore also prevent the development of truly personalized foot orthoses.

However, the availability of a high quality, accurate and low cost 4D foot scanner would allow podiatrists to study the intricate dynamic foot morphology during the whole gait cycle. This would enable them to take the dynamic morphology into account during both the weight-bearing and non-weight bearing states, which could have varying foot measurements of up to 8 mm throughout the gait cycle of a person (Tsung et al., 2003). Based on 4D information of a foot, podiatrists should be able to design and develop improved custom foot orthotics that function, and support the patient correctly during their entire gait cycle. To accelerate the development of such truly personalized footwear, this thesis focuses on the development of a proof of concept for a commercially available, accurate and low-cost 4D foot scanner in podiatry.

## 02. Assignment & project scope

The challenge of this thesis is to redesign the previously developed 4D foot scanner prototype from Vidmar's graduation project (2020) into a low cost scanner with improved accuracy and functionality, which is suitable in the commercial workflow of podiatrists. Achieving this goal takes the following aspects of the scanner into account: data acquisition and processing, material selection, mechanical design, and human-computer interaction design.

To accomplish the project goal, the following research questions should be answered:

- Why should 4D foot scanning be introduced in the field of podiatry?
- What is the added benefit of 4D foot scanning over 3D foot scanning?
- How can Vidmar's foot scanner prototype (2020) be improved in terms of performance for static and dynamic foot scans?
- How can the 4D foot scanner fit into a pipeline of personalized digital manufacturing?

The expected outcome of the project is a physical working prototype of the 4D foot scanner, consisting of a walkway, optimized optics, (aesthetic) embodiment of the scanner, verified data acquisition performance of the scanner, a cost analysis, and an introduction to data processing. The physical prototype should showcase the optimized embodiment of the scanner using commodity hardware, as well as increased performance compared to the 4D foot scanner prototype of Vidmar (2020) in terms of camera scalability and acquisition speed.

To fit the Medisign specialisation, the 4D foot scanner is designed to make it commercially available and desirable in the context of podiatrists. Analyses of the proposed optimized scanner in terms of performance, pricing and scanning results support this fit. Also, the

foot scanner should be compliant to medical device standards and other relevant regulations to make the scanner commercially available for healthcare purposes. Recommendations to achieve this compliance are presented as well.

### Project management


The project is a multidisciplinary project that consists of many intricate components of which some should be approached in a different way. Therefore, a hybrid approach is considered, combining Design Council's Double Diamond framework (2005) with the Lean Startup methodology by Eric Ries (2011). Appendix A elaborates on the application of this approach in this graduation project.

### Reading guide

The structure of this thesis corresponds with the four phases of the Double Diamond framework. The Discover phase describes the concept of 4D foot scanning and evaluates existing 4D foot scanners in chapter 3. Chapter 4 presents research on the field of podiatry and 4D foot scanning opportunities to support further development of this thesis. Chapters 5 through 8 focus on the Define phase, where possibilities in the development of 4D foot scanning are discussed. Finally, chapters 9 through 13 present the development, evaluation, and recommendations for further development of the 4D foot scanner.



# Discover phase



The Discover phase of this thesis introduces the concept of 4D scanning and presents the literature which is used to elaborate on the design and prototyping of the 4D foot scanner. This section also includes an elaborate identification of Vidmar's prototype (2020).



## 03. 4D scanning

3.1	What is 4D foot scanning?	P. 18
3.2	Competitive product analysis	P. 20

This chapter introduces the concept of 4D foot scanning to get a general understanding of what 4D scanning is and how it is different from 3D scanning. Chapter 3.2 analyzes existing 4D foot scanners.

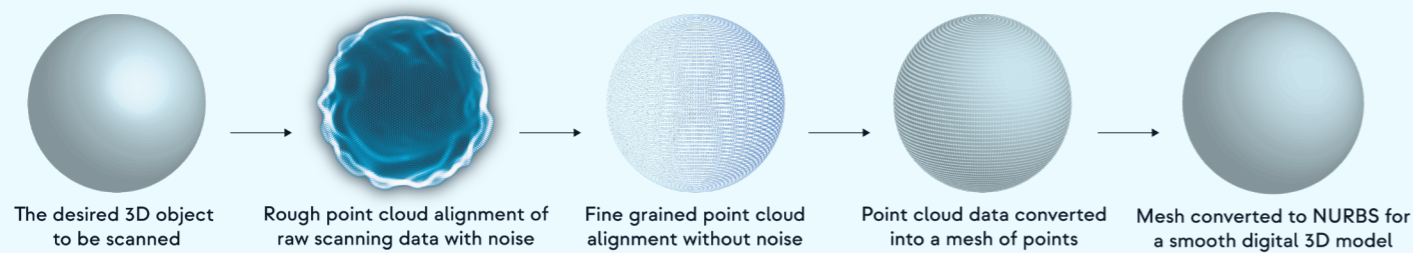


Figure 3.1 - The abstract process of converting a 3D object into a digital model.

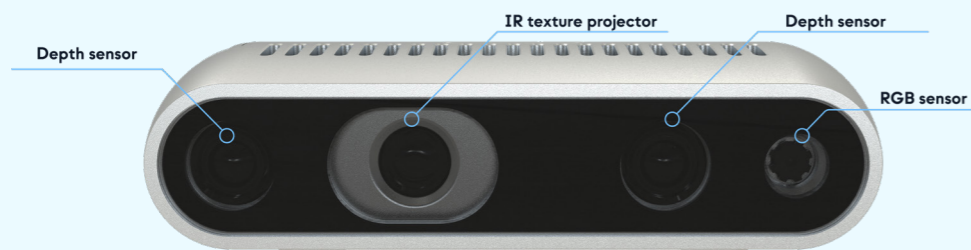


Figure 3.2 - A render of an Intel RealSense D435i camera with its sensors labeled.

### 3.1 What is 4D foot scanning?

4D foot scanning, also known as dynamic 3D foot scanning, is the process of capturing consequent 3D scans of the foot, which allows to observe the dynamic morphology of the foot during the whole gait cycle. The difference between 3D and 4D foot scanning is the ability to extend the 3D scanning process over a certain time period, making time the fourth dimension.

Fundamentally, it consists of the same principles, where the shape of the foot is determined in a 3D space and is represented by point clouds. These point clouds are transformed into a mesh, which then can be smoothed out using NURBS (Non-uniform rational B-spline) to represent curves and surfaces. The results in a 3D model of the scanned object that is usable in CAD modelling. The process is abstractly visualized in figure 3.1. A real world example is given in the following section.

#### 3D scanning

The determination of an object in a 3D space is generally done with depth data, which can be acquired in several ways. A common and accurate (up to sub-millimeter

accuracy (Revopoint, 2019)) method is using stereo depth cameras, such as Intel RealSense cameras, a Microsoft Azure Kinect, or Revopoint's Acusense 3D depth camera. A stereo depth camera setup generally consists of an infrared (IR) laser projector and two infrared cameras (figure 3.2).

When the IR projector projects a (pseudo) random IR pattern onto a scannable object, the stereo camera setup captures the scene. Figure 3.3 shows the result of a static scene capture from both the left and right IR sensors of an Intel RealSense D435i camera. The object of interest here is a 3D printed hand. Figure 3.4 presents the depth image result that is acquired from the photos in figure 3.2 by finding corresponding points in both images. OpenCV's StereoBM algorithm allows the creation of such depth images.

The process of acquiring images with depth data can be repeated for multiple cameras and for different views. Figure 3.5 shows how this is done for two cameras, scanning the same object. From the depth data of these two camera views, a point cloud can be generated (figure 3.6).

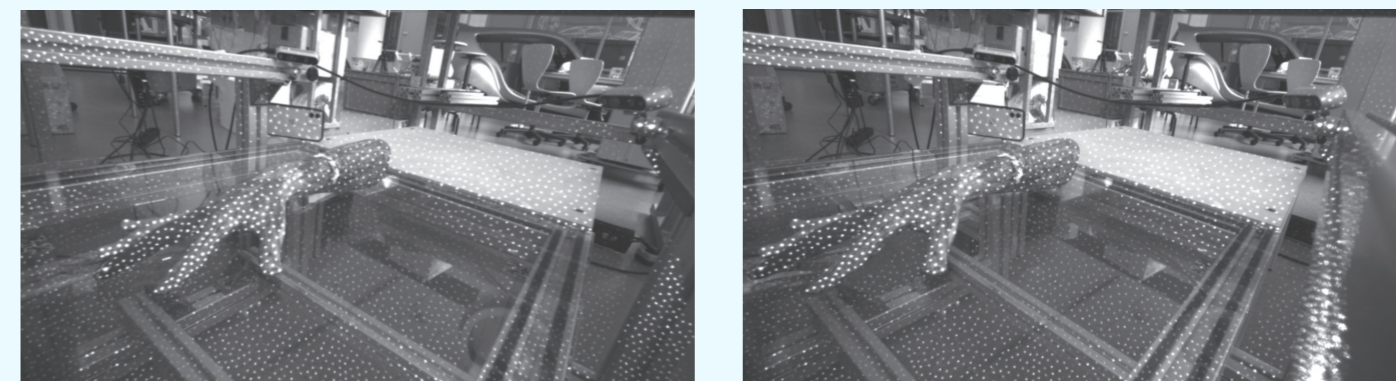


Figure 3.3 - Individual infrared images captured with an Intel RealSense D435i camera. The pseudo random IR pattern that is projected by the built-in IR projector is clearly visible. (left) Infrared image from the left sensor of the camera. (right) Infrared image from the right sensor of the camera.

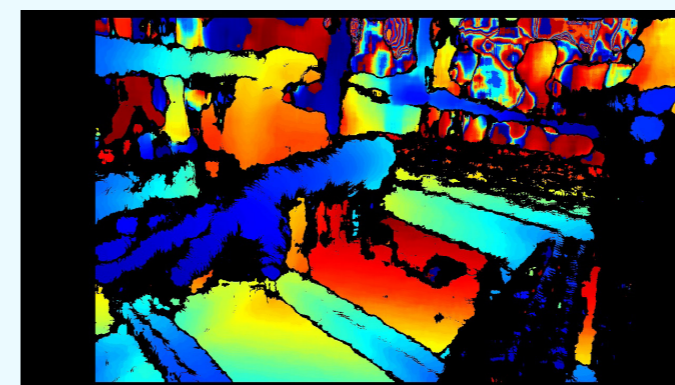


Figure 3.4 - The depth image that is acquired by applying OpenCV's StereoBM algorithm on the images from figure 3.3.

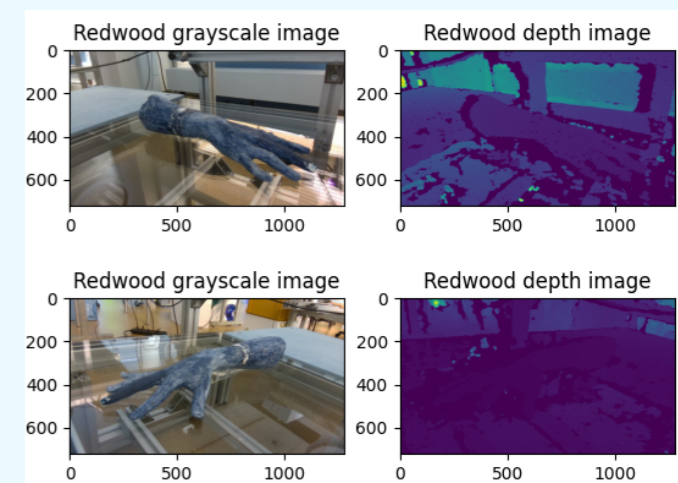


Figure 3.5 - (top row) Capturing a 3D printed hand from the left side; showing both the RGB and depth image. (bottom row) Capturing a 3D printed hand from the right side; showing both the RGB and depth image.

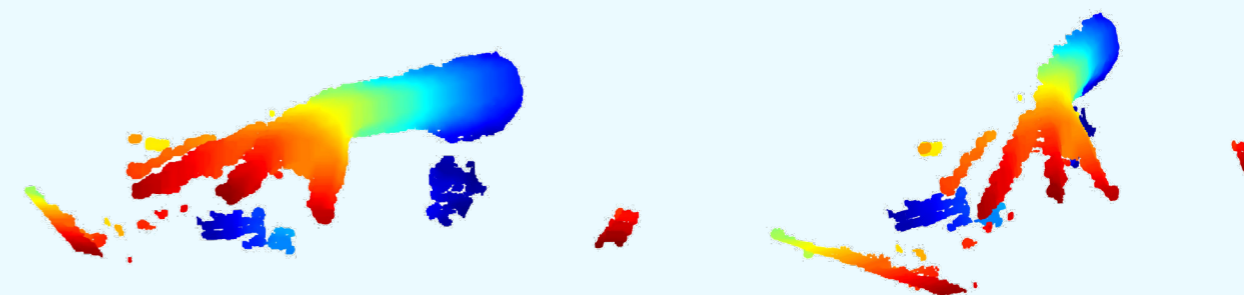


Figure 3.6 - The resulting point cloud that can be generated from the two camera views as illustrated in figure 3.5.



Figure 3.7 - Three frames containing point cloud data of a foot, captured with 4 cameras, observed from an arbitrary point of view in space (Vidmar, 2020).

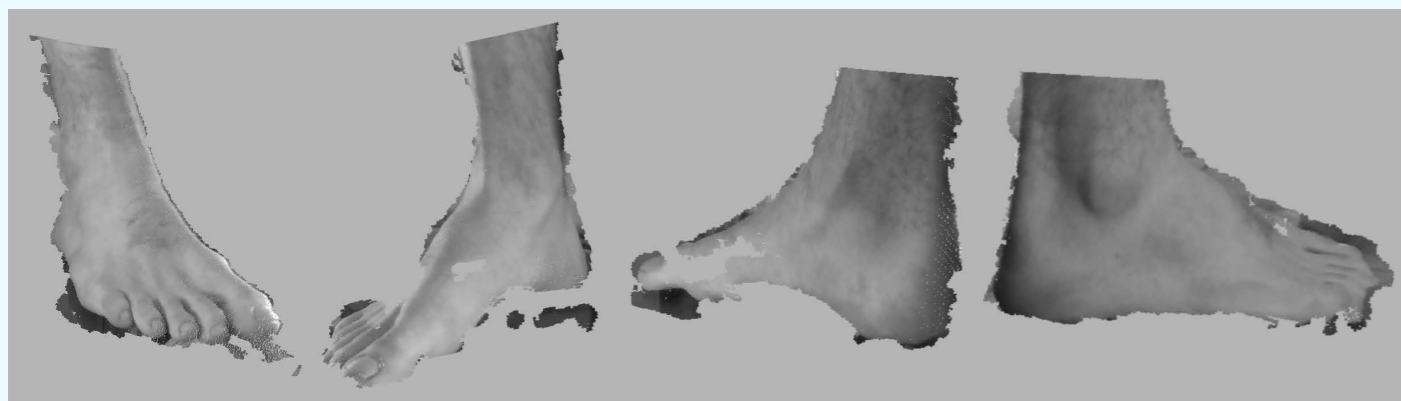


Figure 3.8 - Camera views of a single frame from a dynamic foot scan (Vidmar, 2020).

## 3.2 Competitive product analysis

This section analyses existing 4D foot scanners that are used in research. The insights from this analysis are used in defining development opportunities for a new 4D foot scanner that is focused on commercial use.

### 4D foot scanner by Vidmar (2020)

A previous graduation project (Vidmar, 2020) explored the possibility of developing an affordable 4D foot scanning device from commodity hardware to receive more detailed insights into the dynamic morphology of the human foot. The proposed modular 4D scanning prototype implemented multiple single board computers (Raspberry Pi 4) and four IntelSense D435i stereo cameras, and allowed dynamic data acquisition at 15 fps and a 848 x 480 px sensor resolution.

The scanner's cameras are mounted at the top section of the scanner at arbitrary positions. The modular system architecture of the scanner allows it to capture the foot during a gait cycle. By increasing the amount of cameras,

more aspects of the foot could be reconstructed with possibly a higher accuracy. This modular approach would allow customization for podiatrists, scaling the scanner to their needs of the intended use: larger scanner investment results in a higher scanner accuracy.

The scanner allows a 3D reconstruction of a foot (and parts of the ankle) in motion (figures 3.7 and 3.8). However, the accuracy of these results do not yet meet the performance of comparable existing 4D foot scanners and widely used 3D scanners. As pointed out by Vidmar, weaknesses in the methods of camera calibration and point cloud alignment should be addressed to improve this, since this distorts the scanning result. Since Vidmar's prototype is used as a starting point for further development of the 4D foot scanner, an elaborate analysis is presented in chapter 5.

### 4D foot scanner by Kimura, Mochimaru and Kanade (2009)

Kimura, Mochimaru and Kanade (2009) were able to measure the transformation of the human foot while



Figure 3.9 - Walkway setup using 12 video cameras to capture the foot (Kimura, Mochimaru and Kanade, 2009).

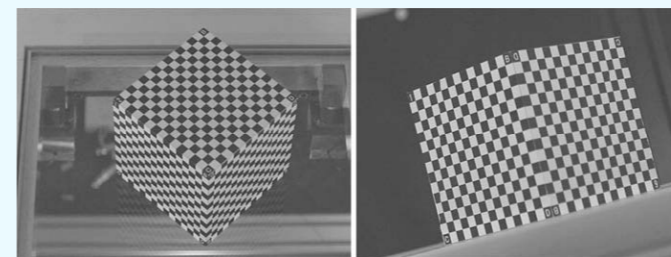


Figure 3.10 - Box with checkerboard pattern used for calibrating the 12 cameras (Kimura, Mochimaru and Kanade, 2009).

walking. In the end, they achieved an accuracy of 1 mm by using 12 video cameras (figure 3.9). This high accuracy was achieved by a combination of camera calibration, post processing and feature extraction. For the camera calibration, they used a box containing the checkerboard pattern on all sides (figure 3.10) in combination with the OpenCV library (Bradski, 2000). The post-processing of the data consisted of bundle adjustment and applying nonlinear optimization using the Levenberg-Marquardt algorithm (Moré, 1978) to reduce the average error to approximately 0.2 pixels. For feature extraction, the foot was marked with a cross-section. The requirement is that the foot is properly marked into sections before the foot is able to be scanned.

### 4D foot scanner by Boppana and Anderson (2020)

Boppana and Anderson (2020) developed a parametric Statistical Shape Model (SSM) of the foot using 4D scans acquired with Intel RealSense D415 cameras. This SSM is able to capture and reconstruct dynamic motion. The scans were made using a treadmill and the DynaMo software (Boppana and Anderson, 2019) (figure 3.11),

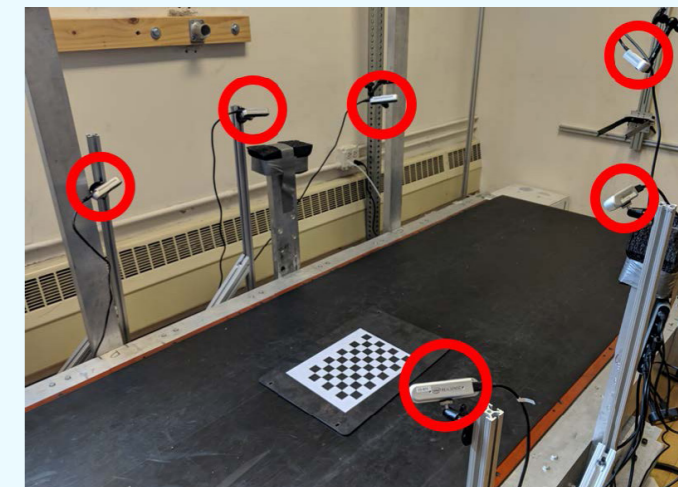


Figure 3.11 - Camera setup on treadmill to capture deformations of foot (Boppana and Anderson, 2020).

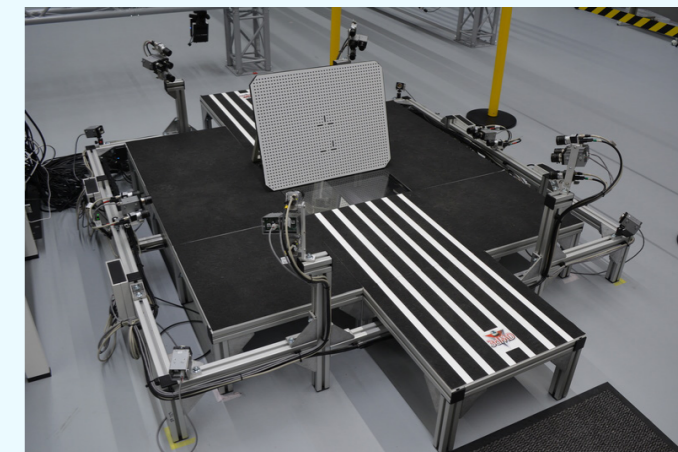


Figure 3.12 - The 3dMDfoot™ System (Max-Plank-Gesellschaft, n.d.).

which allowed them to capture deformations of the dorsal surface of the foot in 90 fps using Intel RealSense D415 cameras. However, this setup does not allow capturing of the plantar surface.

### 4D foot scanner by 3dMD

Currently, only one 4D foot scanner is 'widely' available; 3dMD developed an advanced and high performance 4D foot scanner (the 3dMDfoot™ System) which is predominantly used in a research lab setting and not suitable for the commercial market. The 3dMDfoot™ System (figure 3.12) uses ten pairs of stereo cameras in combination with custom speckle projectors to make static and dynamic scans of the feet. The cameras are able to record with 120 fps and the system has a linear accuracy range of 0.7 mm or better on a frame-by-frame basis. The speckle projector allows for highly accurate stereo reconstruction of the feet during a gait cycle (3dMD, 2021; Max-Plank-Gesellschaft, n.d.).

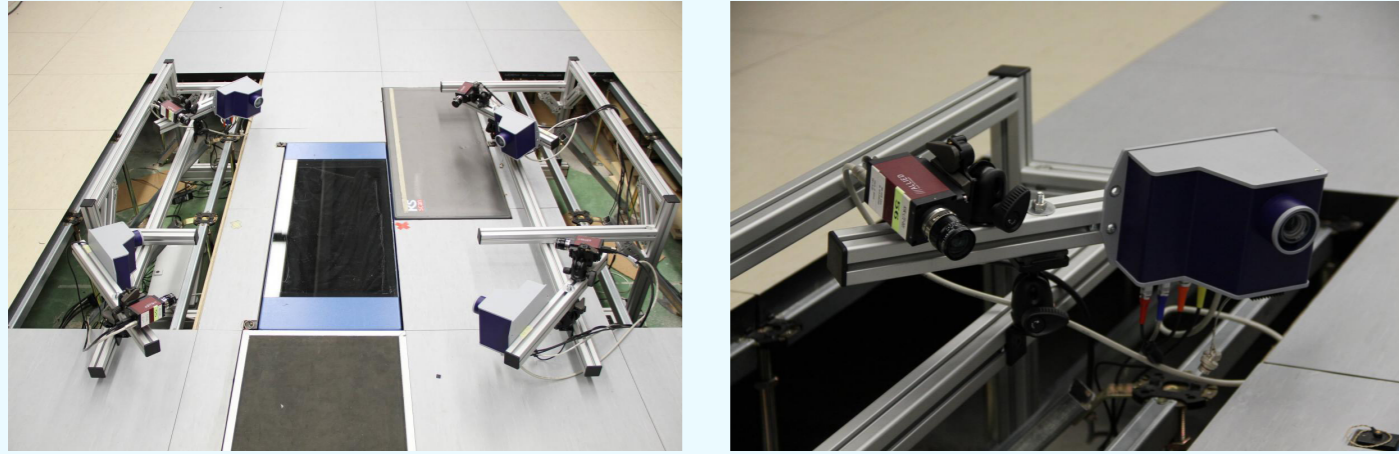


Figure 3.13 - The Thomas More MOBILAB scanner. Equipped with five viALUX scanners and a glass force plate (MOBILAB, n.d.).

#### **Thomas More - MOBILAB**

This scanner of MOBILAB (figure 3.13) is equipped with five viALUX scanners, and is able to record biomedical parameters during the 3D scanning, e.g. ground forces. The ground force is measured by using a glass force plate in combination with one of the viALUX scanners mounted underneath. To capture the rest of the foot, the other 4 viALUX scanners are used.

#### **DynaScan4D - Sportmedizin Tübingen**

Schmeltzpfenning (2009) developed DynaScan4D, which is a multi-sensor system, also equipped with five viALUX scanners, attached to a 4.6 m long and 0.8 m high walkway. The scanner setup is similar as with the MOBILAB scanner, however, this system includes an additional plantar pressure measurement system (EMED, Novel GmbH, Munich), which allows for a more in-depth force analysis.

## 04. The field of podiatry

4.1	Foot scanning in podiatry	P. 26
4.2	Footwear in podiatry	P. 30
4.3	Foot pathology	P. 32
4.4	4D scanning opportunities in podiatry	P. 34

This chapter describes how foot scanning is used in podiatry, the current design and manufacturing process of (custom) podiatric footwear, and foot pathologies that benefit from 4D scanning. Lastly, opportunities for 4D foot scanning are presented.

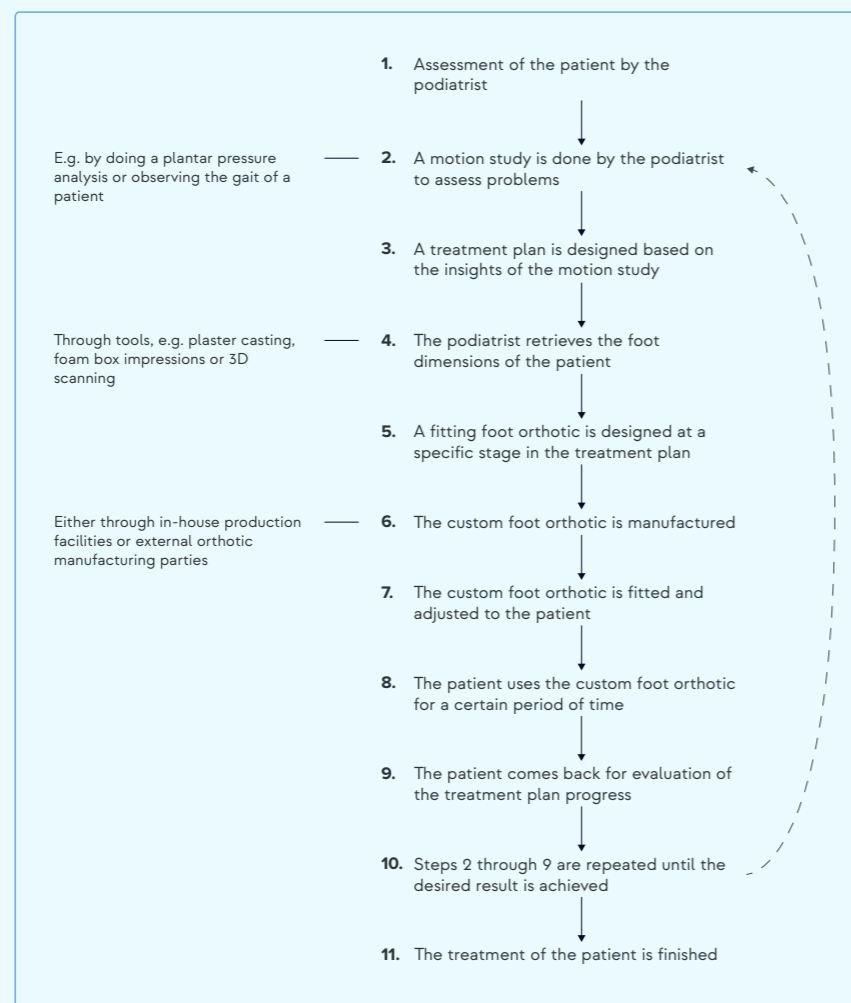


Figure 4.1 - A flow diagram of the steps a podiatrist takes to treat a patient using custom foot orthotics. The diagram is a result of an interview done with podiatrist L. Fuit (personal communication, 18 March, 2021).

Podiatry is a (para)medical field with the focus on treating physical conditions in the lower regions of the human body. Treatment often is related to feet conditions, but conditions in the knees, hips or lower back are also treated.

(Custom) footwear in podiatry can be considered as a means to achieve the desired result in a treatment plan. Podiatrists use a variety of methods to capture the dimensions of a human's foot, which can then be used as input data to design custom footwear solutions. Depending on the type of foot and the patient's problem, the podiatrists has two tasks: 1) to make an assessment on what type of footwear the patient needs in order to achieve the desired outcome at the end of the treatment plan, and 2) to design the supporting and personalized footwear solution.

## 4.1. Foot scanning in podiatry

Carrying out an elaborate motion study of a patient is necessary for a podiatrist to assess a patient's problems. Based on this study, podiatrists develop a treatment plan to achieve the desired result which should relieve the patient from their problems. This treatment plan is an iterative process, where the podiatrist constantly re-assesses the progress of the patient, checks if the progress is still adhering to the treatment plan, and designs a new custom orthotic which suits the new situation. In this process, the podiatrist relies on professional experience and tries to translate the findings of the motion study into an orthotic design that progresses the patient towards the goal.

The general process of a podiatrist and the steps they take to treat a patient using insoles is visualized in



Figure 4.2 - (left) plaster casting the foot in a non-weight bearing state and (right) using a foam box to receive a negative impression of the foot in a weight bearing state (Ottawa Orthotic Lab, n.d.).

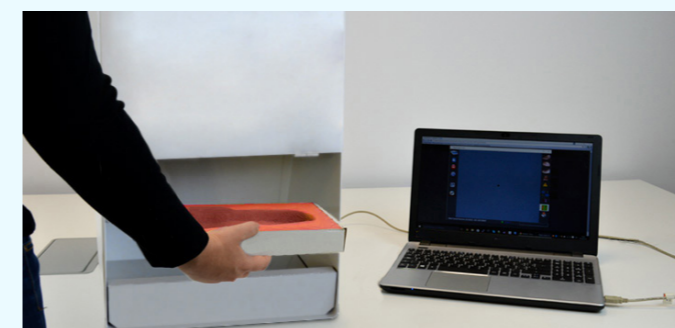


Figure 4.3 - Scanning the used foam box with the Voxelcare 3D Laser Foambox Scanner (Voxelcare, n.d.).

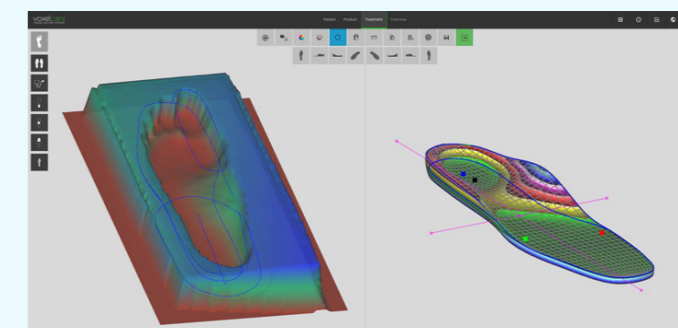


Figure 4.4 - Digital results from the scanned foam boxes using the Voxelcare 3D Laser Foambox Scanner (Voxelcare, n.d.).

the flow diagram of figure 4.1. The process is based on an interview done with podiatrist L. Fuit (personal communication, 18 March, 2021) and only describes the podiatry interaction process with the patient. The primary focus throughout this thesis is on steps 2, 4, 5, and 6 of the podiatry workflow as visualized in figure 4.1, since these steps are related to the usage of dynamic foot scanners and the usability of dynamic foot scanning data.

### Scanning methods

In order to assist the podiatrist in this study, tools to retrieve information about feet are widely used. These tools have evolved over the years and current methods are based on markers, goniometers, plantar pressure analysis or interpretation of imprints (Barisch-Fritz et al., 2014). Using plaster casting, impression foam systems and 3D scanning, a podiatrist is able to capture the shape of the foot in a *static state*, which is used as input for the

manufacturing of the orthotic. The scanning methods can be divided into two types: *indirect 3D scanning* and *direct 3D scanning*. Indirect 3D scans use an additional (physical) medium (e.g. plaster casts or impression foam systems) in the registration of feet shapes, whereas direct 3D scanning can directly register the shape of the feet without an additional step.

### Indirect 3D scanning

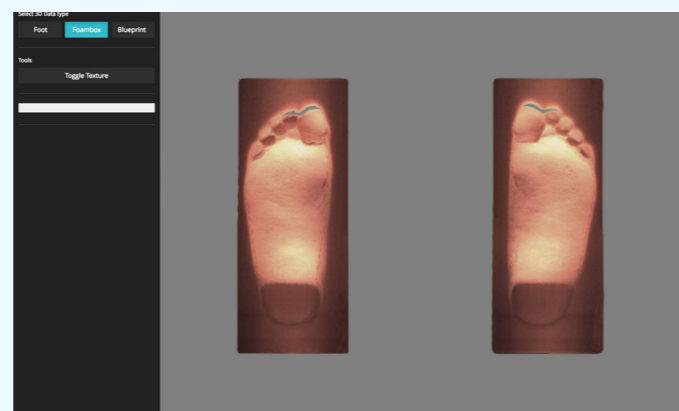
With **plaster casting** and **impression foam systems** (figures 4.2), a negative of the foot is produced. This negative is then either casted into a positive shape of the foot which is used as reference in the orthotics manufacturing, or the negative is scanned with optical 3D (hand) scanners, such as the Voxelcare 3D Laser Foambox Scanner (figure 4.3 & 4.4) or the Artec Eva (figure 4.5) to retrieve the shape of the foot to which the orthotic has to be modelled.



Figure 4.5 - The Artec Eva, a handheld 3D scanner to capture objects (3D Scan Expert, 2017).



Figure 4.6 - The 3D Laser Foot Scanner by Voxelcare, which is able to accurately scan the plantar surface of feet (Voxelcare, n.d.).



### Direct scanning

With 3D scanners, podiatrists are able to accurately (sub millimeter precision) determine the dimensions of the foot and surface texture of the plantar surface. From this data, the podiatrist is able to design custom orthotics, which can be manufactured using subtractive (e.g. CNC machining) or additive manufacturing. There are two main types of 3D foot scanners:

- Scanners that only register the plantar surface of the feet, such as the 3D Laser Foot Scanner by Voxelcare which can also be used to scan a foam box (figure 4.6);
- Scanners that are able to scan the entire shape of the foot, including the dorsal surface and ankle, such as the Tiger 3D scanner by RS scan International (figure 4.7).

When the reproducibility of the indirect and direct scanning methods are evaluated, it can be concluded that none of these scanning methods are meeting all requirements for excellent reproducibility, as mentioned in the study of Telfer et al. (2012). They show that there exists a minimum 20 % discrepancy in accuracy of reproducibility of both the indirect methods, as well as the direct 3D scanning method. Nonetheless, a more experienced CAD operator should be able to achieve improved and usable results, with an overall volume match of > 87 %. when modelling a foot orthotic based on a 3D model of a 3D foot scan. In order to do this, the CAD operators rely on the depth data, as well as the RGB data, since it is easier to find corresponding points with the latter (W. ten Cate, personal communication, 21 April, 2021).



Figure 4.7 - The Tiger scanner of RS scan International (left), which is able to output a 3D model of the foot including the ankle (right) (Materialise Motion, n.d.).

### Foot measurements

Literature (Telfer et al., 2010), international standards (International Organization for Standardization, 2017) and professional insights in podiatry by L. Fuit (personal communication, 18 March, 2021) shows that the primary states in which the foot is currently analyzed are either in a non-weight bearing state, a half-weight bearing state that adheres to the ISO 7250:2017 standards and a full-weight bearing state.

Also, the ISO 7250:2017 standard describes the foot length and foot width as the only relevant foot dimensions in generic footwear design (so not personalized footwear). However, current footwear fitting standards use the foot length, foot width, as well as the arch length (the length between the heel and ball joint of the foot) to fit standardized shoe sizes (ASTM International, 2017). The ASTM standard contains the same foot measurements that are acquired when using the Brannock device (figure 4.8), a widely adopted apparatus that is still used in determining the feet dimensions for (commercial) shoe fitting.

Regarding personalized footwear, it seems that there are no standardized measurements available. Several studies do present additional foot measurements next to the aforementioned standardized measurements to accommodate personalized footwear. Telfer and Woodburn (2010) present the foot length, heel width and ball width in a 3D scanner comparison, where anthropometric changes in the foot under weight bearing

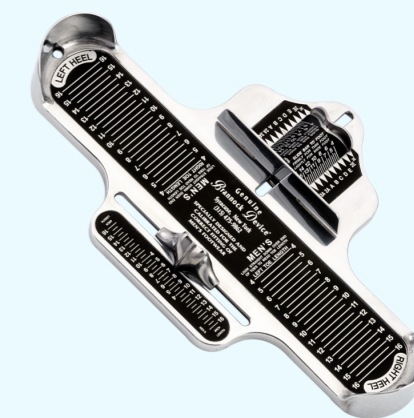


Figure 4.8 - The Brannock Device which is widely adopted in obtaining foot measurements for shoe fitting. (The Brannock Device Co, Inc., 2019). It measures the foot length, foot width and arch length.

conditions are measured. The study by Schmeltzpfening et al. (2009) measured 8 values for the foot length, foot width and structure of the medial longitudinal arch in five different stance phases for three groups classified between the 25th and 75th percentile, categorized by body weight (BMI) and age. The five different stance phases are the heel strike, foot-flat, midstance, heel-off, and the toe-off, as visualized in figure 4.9. The study shows large deformations in absolute values when comparing different stances and measurements. However, group specific changes were not apparent within the gait cycle or between static and dynamic conditions.

As presented by Boppana and Anderson (2020), a detailed understanding of the dynamic foot morphology can enable the design of more comfortable and better fitting footwear. 4D foot scanning could resolve the limitations that current foot scanning methods have, since

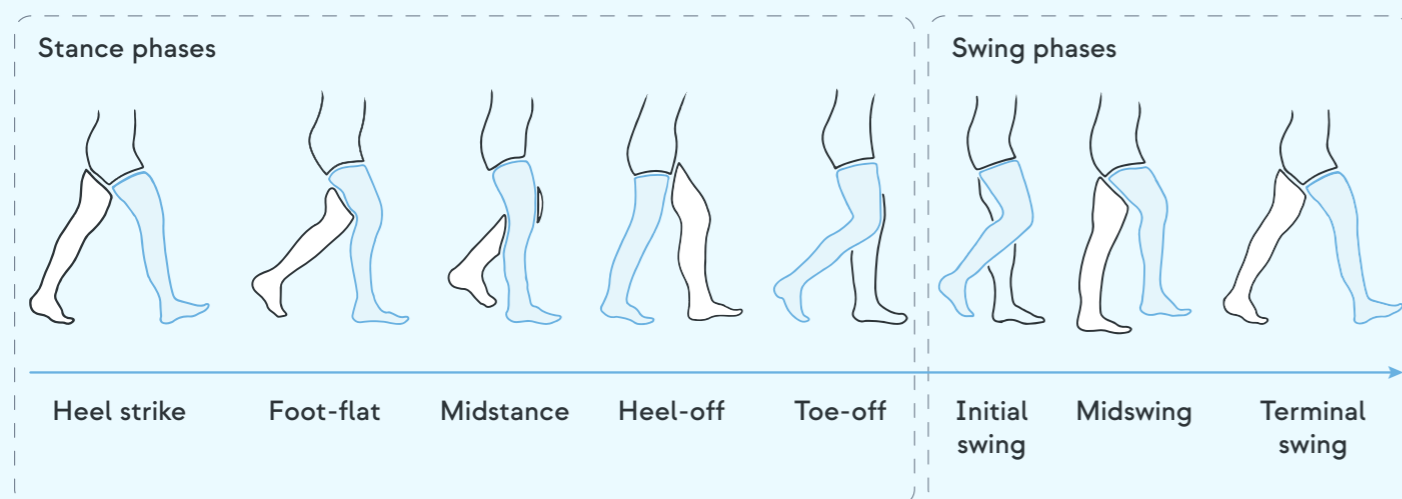


Figure 4.9 - The different stages of a gait cycle.

it enables the ability to capture the dynamic morphology of a foot during the whole gait cycle, where the most relevant phases are considered the stance phases (figure 4.9). In podiatry, 4D scanning could assist in executing motion studies, determining treatment plans for a patient that includes more or all phases of the gait cycle, and improved development of foot orthoses.

## 4.2 Footwear in podiatry

A common footwear product that is used in podiatric treatment are insoles, colloquially known as foot orthotics or orthotics. The production of personalized orthotics is either done in-house, or at orthotics labs who are specialized in producing orthotics and have all manufacturing equipment.

Next to custom-made insoles, there are competing over-the-counter insoles and also 'sham' insoles, which are insoles with a placebo effect and provide no biomechanical or neurological effect. Even though the study of Rasenberg et al. (2016; 2020) shows that these soles might have a similar effect on plantar heel pain (with restricted treatment possibilities for podiatrists), custom insoles show significant results for specific pathology conditions (MacLean, Davis & Hamill, 2008; Hsu et al., 2014; Eslami, 2009).

Generally, there are three methods of producing custom made orthotics (DeskProto, n.d.; L. Fuit, personal communication, 18 March, 2021; Materialise Phits Suite, n.d.):

1. **By hand:** standardized elements are glued onto a base orthotic according to the prescription of the podiatrist. The intermediate result is layered with the desired material to make the whole orthotic smooth. It is then finished by hand, using grinders to smooth out the edges. Designing and manufacturing orthotics is a labor intensive and wasteful process.
2. **Subtractive manufacturing:** using CNC milling to mill out a foam block with the desired density (dependent on the prescription of the podiatrist). With CNC milling, it is possible to directly mill all predetermined elements into the foam as per prescription. Post-processing (cutting away extra material and glueing the top layer of the sole) is needed to retrieve the final orthotic. This manufacturing process is much faster, however, because of the subtractive manufacturing nature of CNC milling it is still a wasteful process. Also, next to a CNC mill, the initial foot has to be digitized into a digital 3D model. For this, 3D scanners are used in the ways described in chapter 4.1.
3. **Additive manufacturing:** with the introduction of 3D printing and increased demand for ultra personalized products, the first steps are made into 3D printing custom foot orthotics. This approach also requires a digital 3D model. With this method, the elements as prescribed by the podiatrists are implemented into the 3D print design of the orthotic. The upside of using additive manufacturing instead of subtractive manufacturing

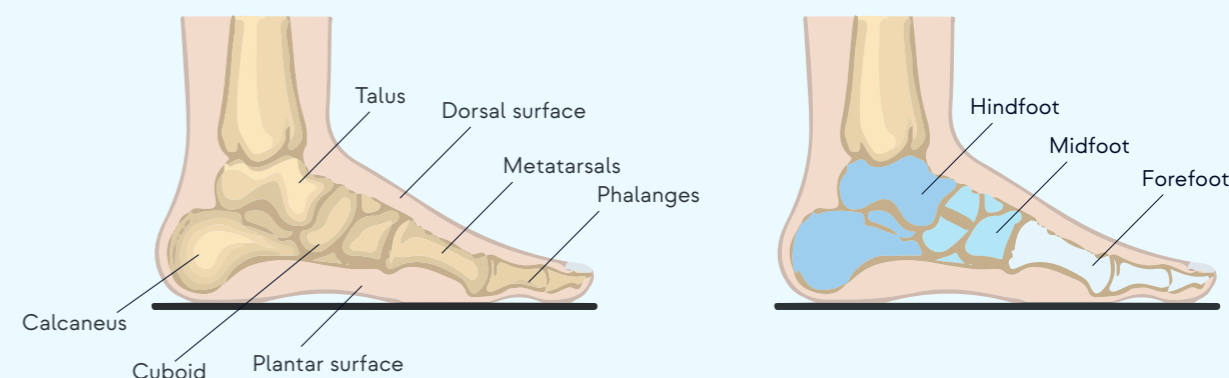


Figure 4.10 - (left) A schematic view of the anatomy of a human foot. (right) A schematic side view of a human foot, classified into three sections: the hindfoot, the midfoot and the forefoot.

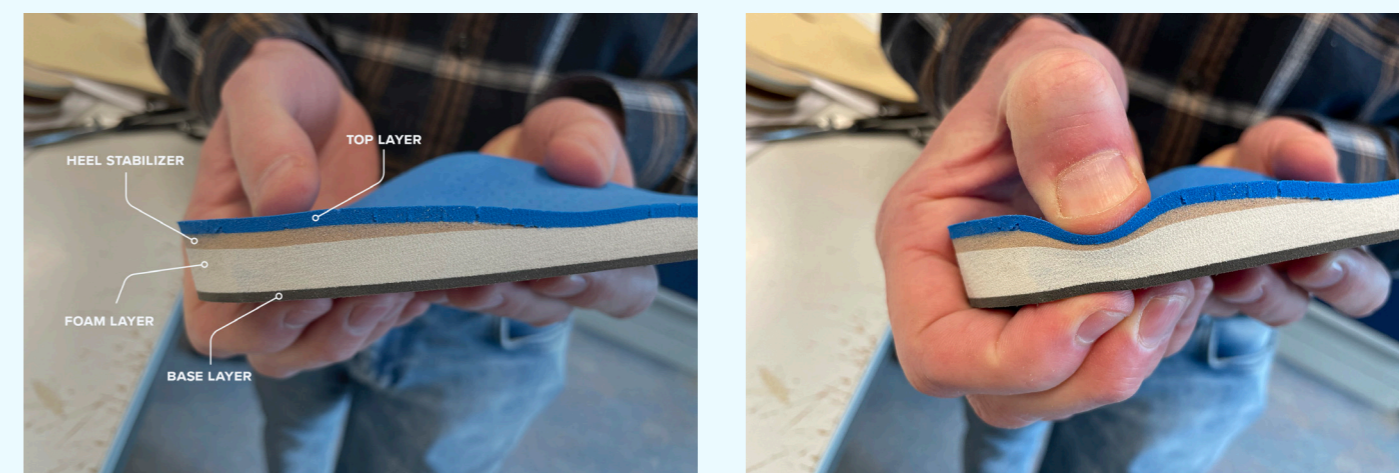


Figure 4.11 - (left) Side view of a custom made orthotic, using CNC milling. Post processing of the sole is done by hand. (right) The deformation of the orthotic when (point) pressure is applied. Notice how the base layer does not deform, providing an even weight distribution of the patient onto the inside sole of the shoe.

(e.g. CNC in the production of foot orthotics is that the weight of the final product can be reduced more with additive manufacturing. Also, there is less residual waste.

An insole consists of three sections, which correspond to the three sections of the foot as visualized in figure 4.10: the hindfoot, the midfoot and the forefoot. The idea is that the insole is able to support the foot during three key moments in a person's gait: the heel strike, the midstance and the toe-off. Depending on the foot pathology, a section might need more support/correction than the other sections.

The whole insole has multiple layers, each having a different function. In general, there are three layer types that make up an insole: 1) a **base layer**, 2) the **custom layer**, and 3) the **top layer**. The amount of layers of an orthotic ranges between three and five layers, depending

on the use case (daily use or activity specific). Figure 4.11 shows the side view of a custom made orthotic, where four different layers can be differentiated. The orthotic is initially CNC milled, and later post-processed by hand:

- The **base layer** can be made out of different types of material, depending on the purpose of the orthotic (casual wear, everyday use, sports). A common material to use for this base layer is polyurethane (Orange Insoles, 2020; PolyLabs, n.d.). It provides initial support and acts as a platform to attach the elements on. The base layer is glued onto the bottom of the foam layer.
- The **custom layer** consists of two parts here. 1) The **foam layer** is the layer that determines the final shape of the foot orthotic since it includes the elements that are added by the podiatrist. It is generally made out of EVA foam (Ethylene-vinyl acetate). The design of this layer is first 3D modelled and then used as input for the CNC mill.





Figure 4.12 - A selection of foam layers with different densities to best accommodate the orthotic specifications of a patient. The foam layers are CNC milled into the 3D modelled design, including the selected elements that are added to the orthotic by the podiatrist.

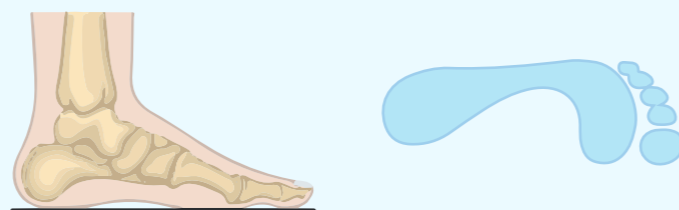
The foam layer comes in a variety of densities (figure 4.12, which is carefully selected depending on the patient's specifications, pathology). 2) A **heel stabilizer** is added to provide more correction and control during the heel strike of the patient's gait. In hand-made insoles, the elements are standardized physical elements that are glued onto the foam layer of the insole. The elements have to be positioned precisely, otherwise the element will have a different supporting function onto the foot than was intended.

- The **cover layer** is a protective layer that has to resist continuous mechanical stress, since this part of the orthotic is in direct contact with the patient's foot. It generally has antimicrobial properties to extend the product's life.

### 4.3 Foot pathology

As previously mentioned, podiatrists are capable of treating patients that have physical problems with foot related complaints, often resulting in pain in feet, ankles, knees or even the spine. Foot pathologies range from small deviations in the bone structure or flexibility in the ligaments, to severe deformities of parts of the foot. Pathologies could have a genetic or congenital origin, but can also be caused by diseases such as a metabolic disease (diabetes).

A selection of pathologies that are relevant to the scope of this project and fit the acquisition capabilities of a 4D foot scanner are discussed in this section.



Normal foot

Figure 4.13 - (left) A schematic side view of a normal foot. Notice the space beneath the plantar surface of the foot, caused by the natural arching aspect of a foot. (right) A plantar surface scan of a normal foot.

#### Flat foot (fallen arches)

A common foot pathology is flatfoot, characterized by the loss of the medial arch and often caused when the tendons in the arch are not pulling together properly (DerSarkissian MD, 2012). This results in an increased weight bearing on the medial border of the foot. Visualised by figure 4.14, an imprint of the plantar surface of a patient's foot has no arch present. Because of the asymptomatic nature of this condition, action is only required when a patient experiences pain or irritation. This can be resolved by prescribing (personalized) insoles that increase the height of the arch (Schiller, 2012). A 3D foot scanner is highly capable of observing the height difference of the plantar surface and can therefore be used to analyse this condition. With 4D foot scanning, it would be possible to study the behaviour of the tendons in the arch and its impact on the rest of the foot in different stances of the gait.



Flat foot (fallen arch)

Figure 4.14 - (left) A schematic side view of the general shape of a flat foot, caused by the lack of longitudinal and transverse arch of the foot. (right) A plantar surface scan of the flat foot.

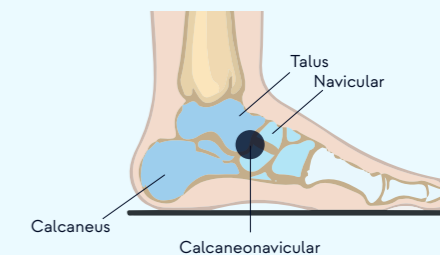


Figure 4.15 - A schematic visualization of the calcaneonavicular coalition.

#### Tarsal coalition

Tarsal coalition is a structural anomaly between multiple tarsal bones, resulting in a rigid flat foot. It is most common with adolescents and while asymptomatic, it primarily causes pain at the calcaneonavicular (figure 4.15, which is the area of the talus, navicular and the calcaneus. (OrthoInfo, 2019). Tarsal coalition pain is often relieved by prescribing (custom) insoles with inserts that increase the arch height of the foot and align the hindfoot. Using 4D foot scanning allows to 1) analyse the plantar surface and design an insole that allows for a larger arch height during the gait, and 2) analyse the rotation of the foot during the gait. Information gained from the latter can help in designing an orthotic with proper hindfoot alignment. Comfort should be taken into account in the design of the orthotics, since rigid elements may cause discomfort (Watts MD & Sink MD, n.d.).

#### Diabetes

For people with diabetes and people with peripheral vascular disease, regular examination of the feet is necessary, since they have an enlarged risk of ulcers and foot deformities (Whitney DPM, 2019). This is troublesome for diabetic patients since they have a decreased healing potential. Wearing shoes that are too loose, or have a fit that is too tight, can result more quickly in skin irritations, ulcers, and poor blood circulation, which could eventually lead to the need of amputation (McKean, n.d.). Currently, the design of orthopedic shoes is often guided by general design rules, such as soft fabric interior, extra padding, air pockets underneath the heel to reduce the impact on the foot during heel strike. In addition, orthopedic shoes generally include a personalized orthotic (insole) (figure 4.16).

The use of 4D foot scanners would allow podiatrist and orthopedics to analyze the whole gait of a diabetic person and the deformation of not only the foot, but also the ankle. With deeper insights into the deformation of the patient's foot, the inside of an orthopedic shoe can be further optimized for improved personalized fit, reducing the amount of friction and pressure on the foot.



Figure 4.16 - A collection of diabetic foot wear, optimized to reduce the development of ulcers and increase walking comfort (Eagle Pharmacy, n.d.).



## 4.4 4D scanning opportunities in podiatry

The field of podiatry is rather conservative in their habits and used methods. Podiatrists in the Netherlands and West Europe are more open to the adoption of new technologies such as 3D scanners and were already adopted as early as 2002 (L. Fuit, personal communication, 18 March, 2021). But even now, practices in the United States are still holding on to the use of plaster casting and foam box impressions (Preferred Foot & Ankle Specialist, 2021; Active Arch, 2021). However, this does not imply that no practices have moved onto 3D foot scanners and digital gait analysis methods such as plantar pressure analysis.

Introducing a commercially available 4D foot scanning solution into the field of podiatry presents improvements in current methods of gait analysis and foot orthotics design, and opens up a multitude of possibilities in personalized footwear and digital manufacturing. Commercial 4D foot scanning could additionally collect dynamic foot data which could be used in the development of data-driven research. For example by using data to train predictive models.

### Gait analysis

As research shows, available commercial 3D scanning methods are limited in their abilities to capture the foot in both a static and dynamic state. Currently available commercial 3D scanners are able to capture and 3D model the foot exclusively in a static state, but not the dynamic morphology of the foot towards that state, e.g. from heel strike to midstance. Also, retrieving an accurate 3D scan of the foot in a non-weight bearing state is difficult and requires additional scanning products, such

as an Artec Eva 3D hand scanner or a 3D foot scanner with a special non-weight bearing setup.

A person's gait can already be analysed with gait analysis software, using for example video streams, markers (Nagymáté, & Kiss, 2019) or plantar pressure analysis to make a force analysis. But combining this with a 3D foot model of the whole foot (including plantar surface) is not yet feasible in a commercial setting.

With the introduction of a commercially available 4D foot scanner, podiatrists will be able to observe a person's dynamic foot deformation while walking in more detail since the gait can be analyzed frame by frame. The higher the frame rate of the 4D scanner, the more accurately a podiatrist can analyze deformation of the foot. Furthermore, 4D gait analyses can be archived and used for future reference in the treatment plan, i.e. progress comparison of patients with the initial gait and adjust the treatment plan based on this comparison. Also, it would be possible to share the gait analysis with other parties such as orthotics manufacturers, general practitioners, hospitals, insurance companies, and other (health related) stakeholders.

### Rapid product development

A podiatrist currently designs the foot orthotics primarily based on insights retrieved from the motion analysis to hopefully move towards the desired outcome as fast as possible. Professional experience highly influences the process of foot orthotics design, but it is always an iterative process where the podiatrist needs to reassess the corrected gait as a result of the orthotics. By adding insole elements onto the users foot while walking during a 4D gait analysis, the podiatrists can analyze the effect of orthotic elements on the gait of the patient before the manufacturing of the actual orthotics. This would help podiatrists to make substantiated claims to support the

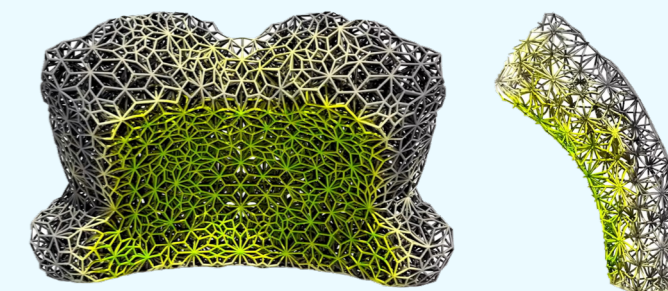


Figure 4.17 - (left) Riddell® Speedflex Precision Diamond Helmet, using Carbon® printing technology (Carbon®, 2019). (right) The lattice structure of the helmet liner, made using generative design in Rhino® Grasshopper®. The green colour represents the exerted force on the lattice structure. The yellow colour shows the distribution of this force throughout the lattice structure (Carbon®, 2019).

decision making in the design process of orthotics. With this, it is expected that less design iterations of orthotics are necessary to achieve the desired outcome for the patient.

Also, 4D foot scans allow for further design and engineering research into the footwear and orthotics design, with for example conducting force analyses using Finite Element Analysis (FEA).

### Personalization in footwear and orthotics

As previously mentioned, the current shoe industry is focused on the static shape of feet, assuming the foot as a rigid part. However, as presented by Tsung et al. (2003), parts of feet can deform up to 8 mm during a gait cycle. Especially when designing shoes for different activities, such as everyday use, athletes and industrial shoes. Again, studies of Luo et al. (2009) and Mündermann et al. (2001) show that increased footwear comfort increases running performance and reduces risk of movement-related injury, respectively. With new possibilities in additive manufacturing and generative design, 4D foot scans could be used to retrieve foot data of the whole gait to design and manufacture optimized personalized footwear, both shoes as well as foot orthotics.

Chapter 4.3 on foot pathologies presents additional opportunities for the use of 4D scanning in not only commercial footwear, but also in podiatry and orthopedic treatment. Many treatment plans involve custom-made orthotics, ranging from insoles to ankle foot orthotics (AFO) or casts, where 4D data could have an informative role in the design. For example, generic or patient specific 4D models could be used to simulate the working

of a digitally designed orthotic. With this, it would be possible to predetermine the effectiveness of an orthotic design before manufacturing.

### Digital manufacturing of personalized footwear

Realizing personalized footwear through digital manufacturing is already achievable with static 3D scanning, as presented in chapter 4.2. But static 3D scanning is mostly able to show the difference between weight bearing and non-weight bearing states, which are essentially the midstance and the swing phases during a gait cycle, respectively. However, a gait cycle consists of four more contact phases that all experience deformation and not all foot problems occur in the midstance and swing phases; e.g. metatarsalgia is a painful phenomenon where inflammation occurs in the ball of the foot, which is often treated/minimized by adding a shock-absorbing orthotic or additional arch support (WebMD, 2020; Mayo Clinic, 2019; Direct Orthotics, n.d.). 4D scanning allows observing, optimizing and manufacturing for these phases, providing support throughout the whole gait of a person, and not only for two states.

### Example of a personalized mass manufacturing pipeline

With the design of the Speedflex Precision Diamond Helmet by Riddell® (figure 4.17, left), Carbon® and Riddell® combined 3D scanning with personal on-field impact data of the head to create a personalized 4D representation of the head. With this, they were able to generate custom 3D printed lattice structures that are optimized for a specific individual (figure 4.17, right).

With this product, Riddell® and Carbon® show the possibilities of utilizing the full spectrum of additive manufacturing: human body scanning, generative design, and 3D printing for large scale manufacturing.

#### **Data collection**

By introducing a way to capture dynamic 3D scanning data of feet, many opportunities for objective data analysis open up. Intricate and accurate dynamic 3D models could be made out of this data to initiate a data-driven approach in footwear and orthotics design. But also dynamic anthropometric models, or machine learning models to predict morphologies after (non-) invasive treatment, could be developed.

#### **Pathology classification**

A large study was carried out by Krauss et al (2008) who used the data generated to categorise the foot into different types: voluminous, flat pointed and slender. This manually intensive task could be easily automated by training classification models to recognize key features of the different foot types.

#### **4D anthropometry**

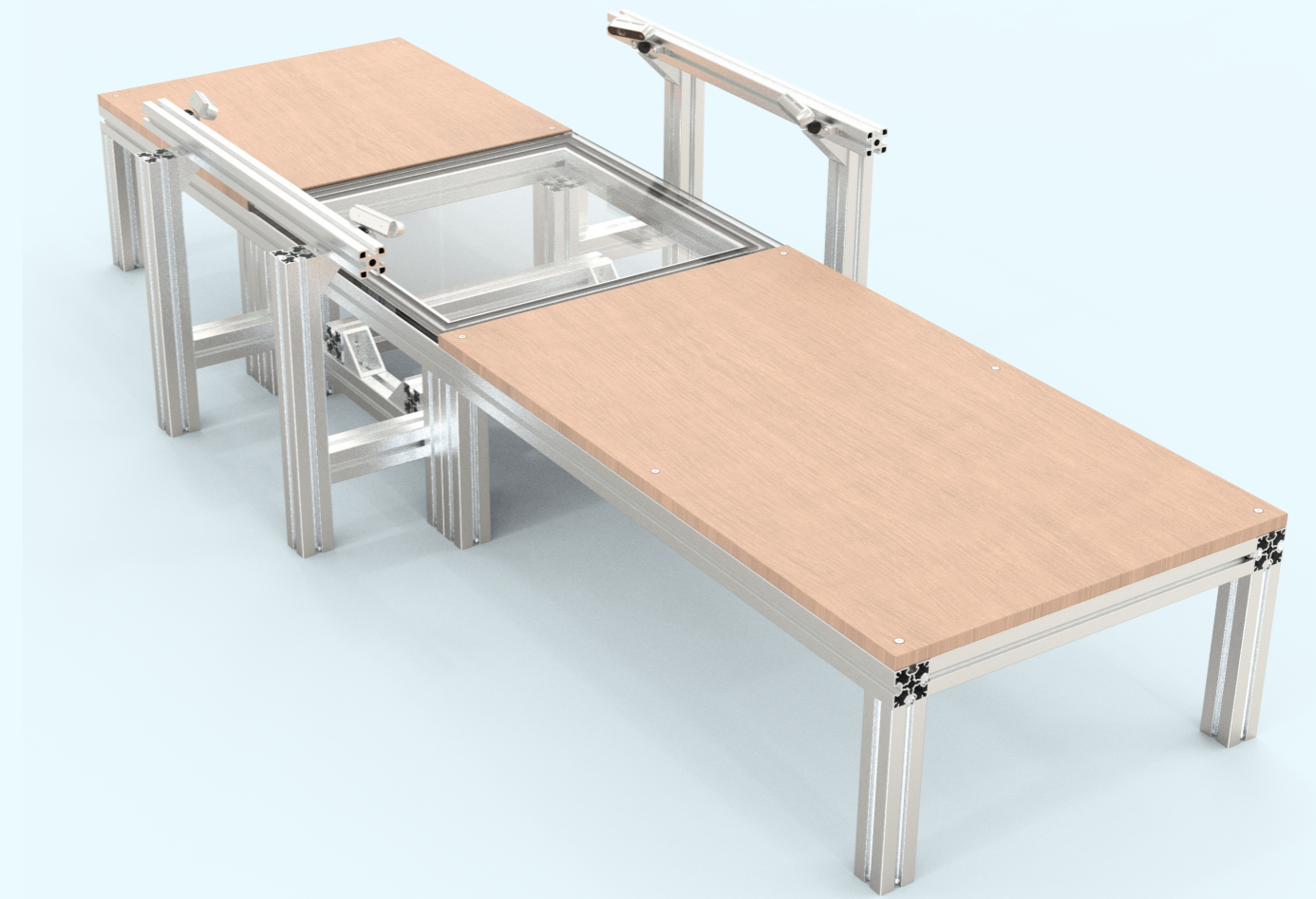
DINED (Huysmans et al., 2020) is an anthropometric database that is able to predict human body measurements from a single database. By using Principal Component Analysis (PCA), which calculates principal components and uses these components to make changes to the initial data, DINED is able to generate a variation of body types from a single database. As with static 3D data, this same method could be applied to a dynamic 3D dataset. This way, gait and deformation simulations of feet with different dimensions can be made from a single dataset, allowing footwear and orthotic designers to study the dynamics of different sized feet more easily.

#### **Predictive physiological effect after treatment**

With the collection of enough 4D data of dynamic foot morphology, it would be possible to use this data in developing predictive models which could help communicating treatment plans of podiatrists to patients. For example a model could be trained to predict the outcome in dynamic foot morphology after a patient finishes a treatment plan. Or perhaps even predict the state of the foot after an invasive surgery operation.

## 05. Prototype identification

5.1	Camera modules	P. 41
5.2	Camera calibration	P. 43
5.3	Data acquisition	P. 45
5.4	Data processing	P. 46
5.5	Camera frame rate	P. 46
5.6	Scanning plate	P. 46
5.7	Scanner component costs	P. 47
5.8	Conclusion	P. 48



As presented earlier, the scope of this graduation project is to develop a cost effective and accurate 4D foot scanner which is usable in the field of podiatry. To accomplish this, Vidmar's 4D scanner prototype (2020) as mentioned in chapter 3.2 is used as a starting point. This chapter evaluates this prototype for the main components of the scanner: camera selection, camera calibration, data acquisition and processing, camera frame rate, and scanning plate.

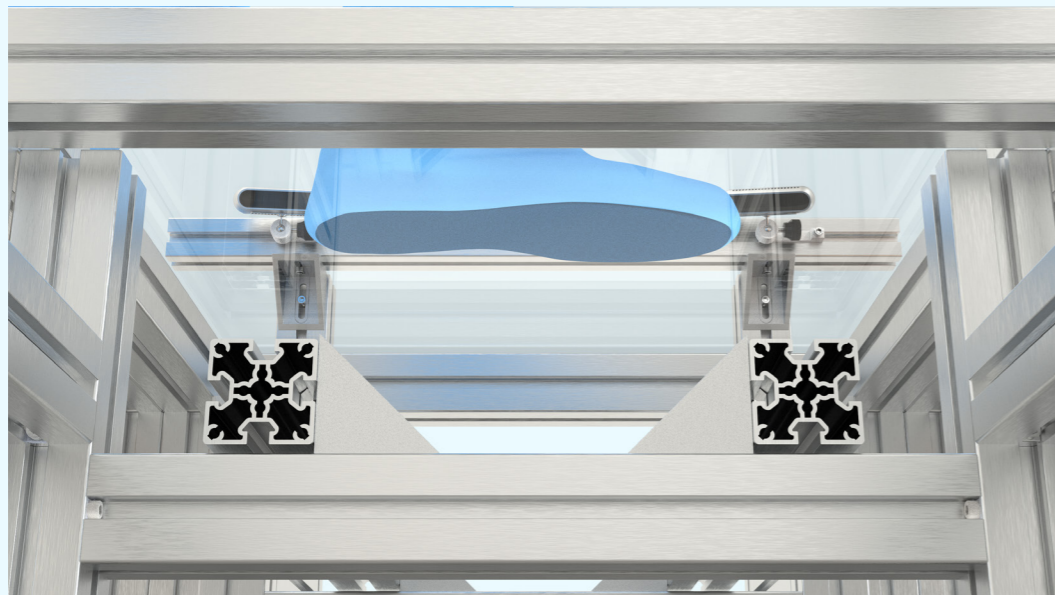
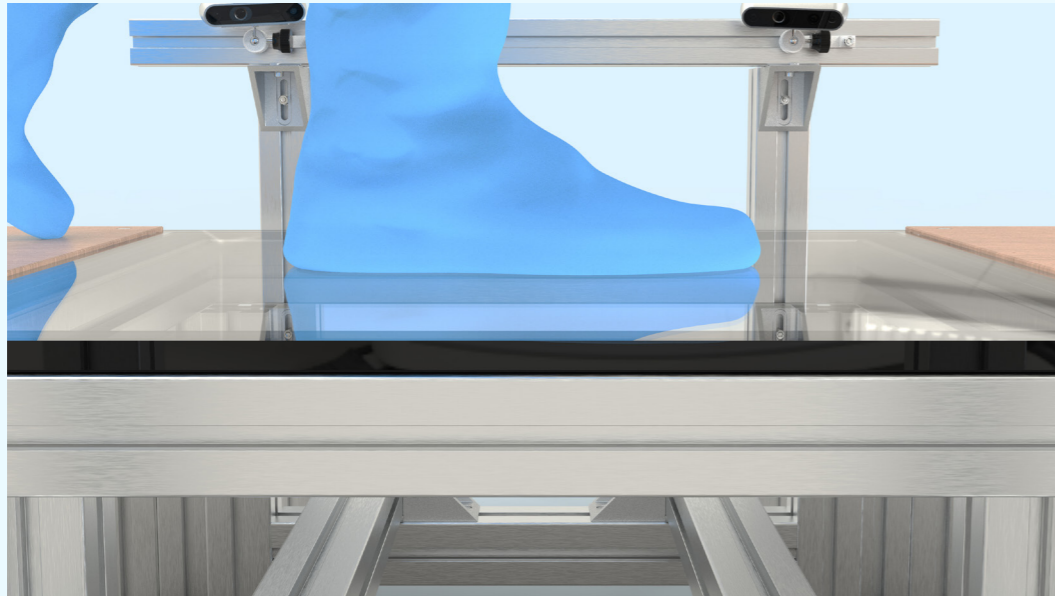


Figure 5.1 shows the bare bones structure of the scanner. Vidmar's final scanning result is presented in figure 5.2, where a 3D printed hand model was used to evaluate the static accuracy of the scanner. This model was used since the dimensions of this hand model were known and could therefore be compared with the scan.

The development of Vidmar's prototype primarily focused on the embedded system design of a modular scanning solution and data acquisition, with a decentralized architecture. Meaning that the data acquisition and data processing are independent of each other. A schematic overview of this decentralized system is presented in figure 5.3. As mentioned by Vidmar in his thesis (2020), decoupling these parts will overcome limitations of a centralized system, such as:

- A fixed amount of PCI expansion slots on commodity PC's limits the flexibility of adding cameras indefinitely;
- Scaling the amount of cameras is likely to cause bandwidth bottlenecks due to limits of commodity hardware;
- Cable management presumably reduces the flexibility of positioning the cameras on the scanner.

To establish the state of the Vidmar's prototype, a function analysis has been made and visualized (figure 5.4). This function analysis only includes the functionalities as presented by Vidmar (2020): camera calibration, data acquisition and data processing.

## 5.1 Camera modules

The camera modules that were used in Vidmar's project are Intel RealSense D435i stereo cameras (2020). These camera modules not only provide promising quality scans, but are also widely commercially available and used in comparable industries for (realtime) computer vision and object detection. Furthermore, they are low cost, and can be configured and operated through the Intel® RealSense™ SDK 2.0 (Intel RealSense, 2021), which is an open source library that allows developers to access the RealSense camera functions. Since the cameras are statically positioned in this scanner, there is no need for the on-board inertial measurement unit

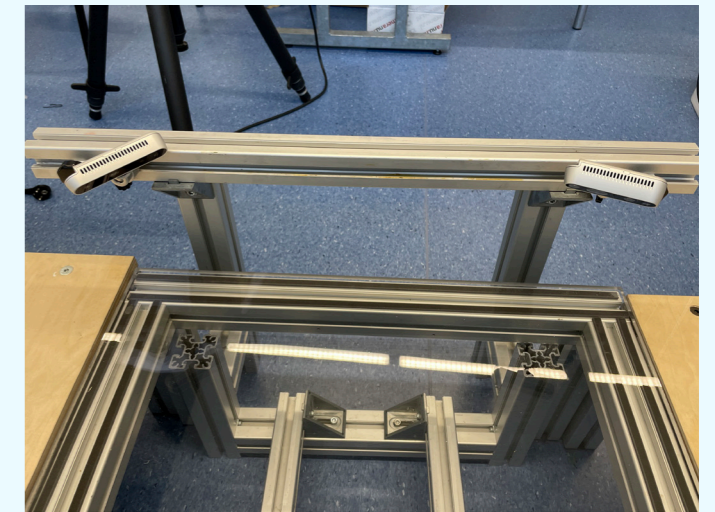


Figure 5.1 - The embodiment of Vidmar's (2020) modular 4D foot scanning prototype. The cameras are mounted onto the scanner using custom 3D printed mounts and the standard Intel RealSense ball mounts. The scanning plate is a 15 mm acrylic plate.

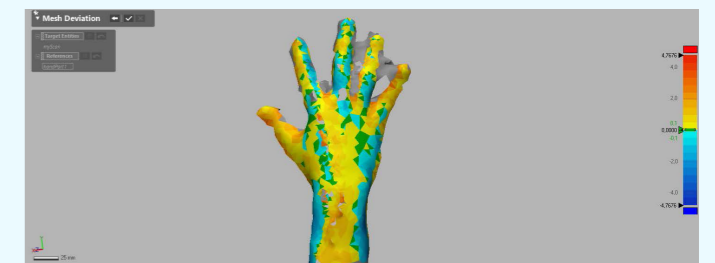


Figure 5.2 - The static accuracy evaluation of a static 3D scan obtained with the developed prototype in mm. The results show an average deviation of 0.58 mm, with errors ranging from -2.8 mm to +4.9 mm.

### Decentralized system

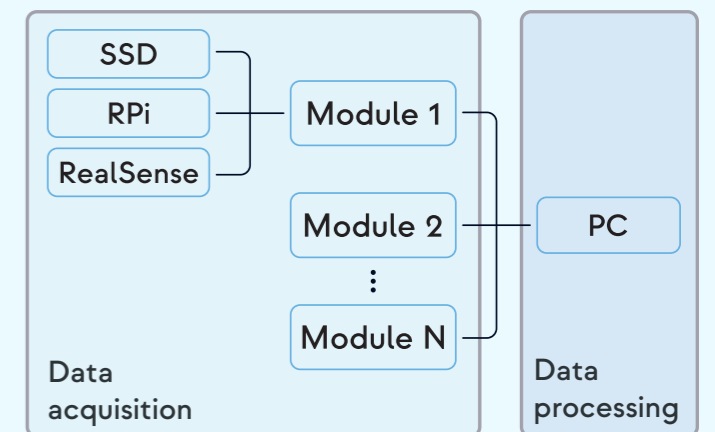


Figure 5.3 - The proposed modular decentralized 4D foot scanner system of Vidmar (2020).

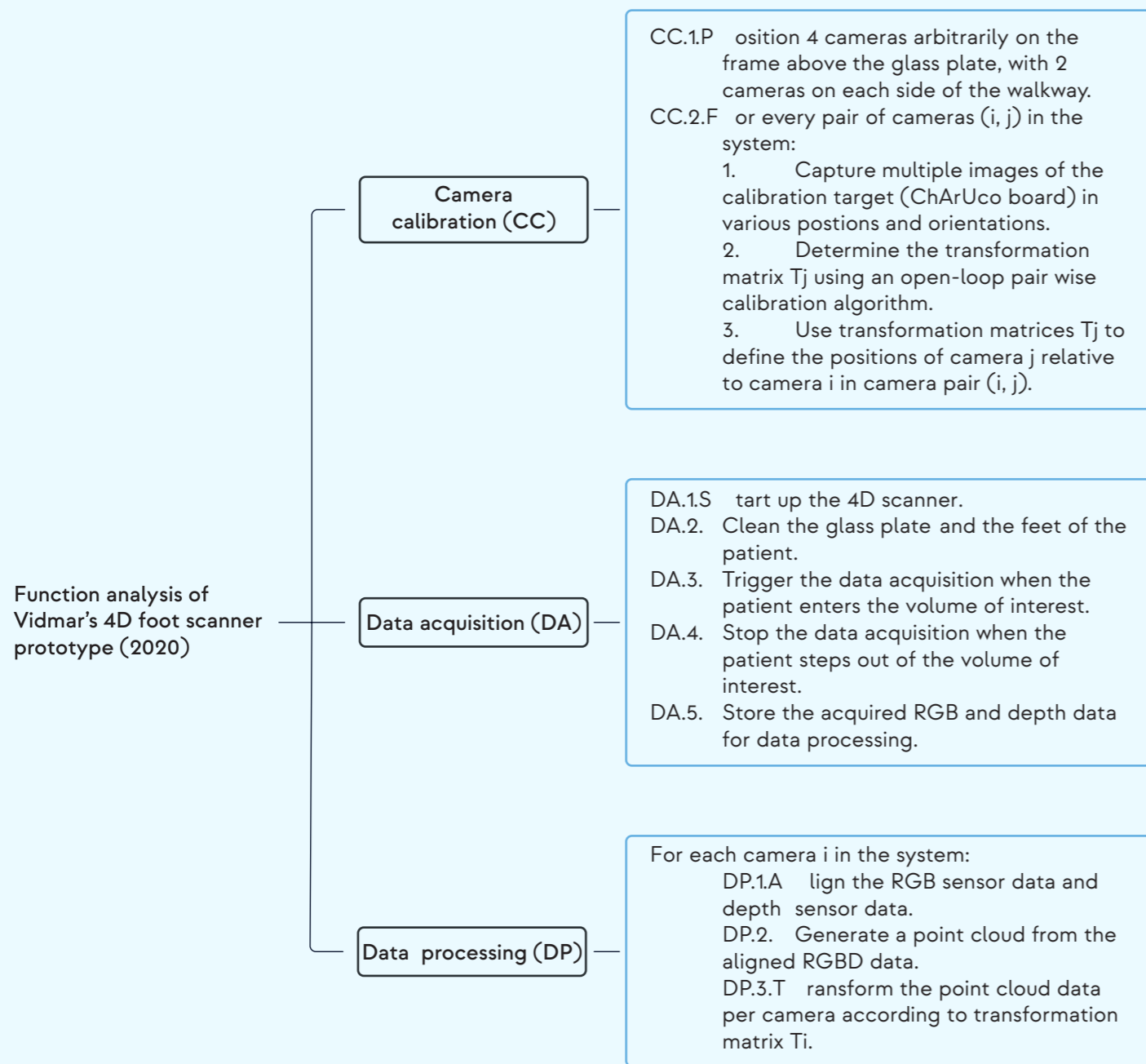


Figure 5.4 - Function analysis of Vidmar's 4D foot scanner prototype (2020).

(IMU), that is capable of detecting rotation and movement of the camera. Therefore, a cheaper solution would be to opt for the D435 (\$ 189) camera, which has the same specifications but excluding the IMU, resulting in a pricing difference of \$20 per camera (the RealSense D435i costs \$ 209).

Boppana and Anderson (2020) showed promising results using the Intel RealSense D415 cameras, which have

similar general specifications as the D435i cameras, but a smaller depth field of view (FOV) and an increased ideal range. Their setup allowed the use of D415 cameras since they positioned the cameras further away from the volume of interest (figure 3.11). Table B.1 in Appendix B lists the differences between the three cameras (D415, D435 and D435i).

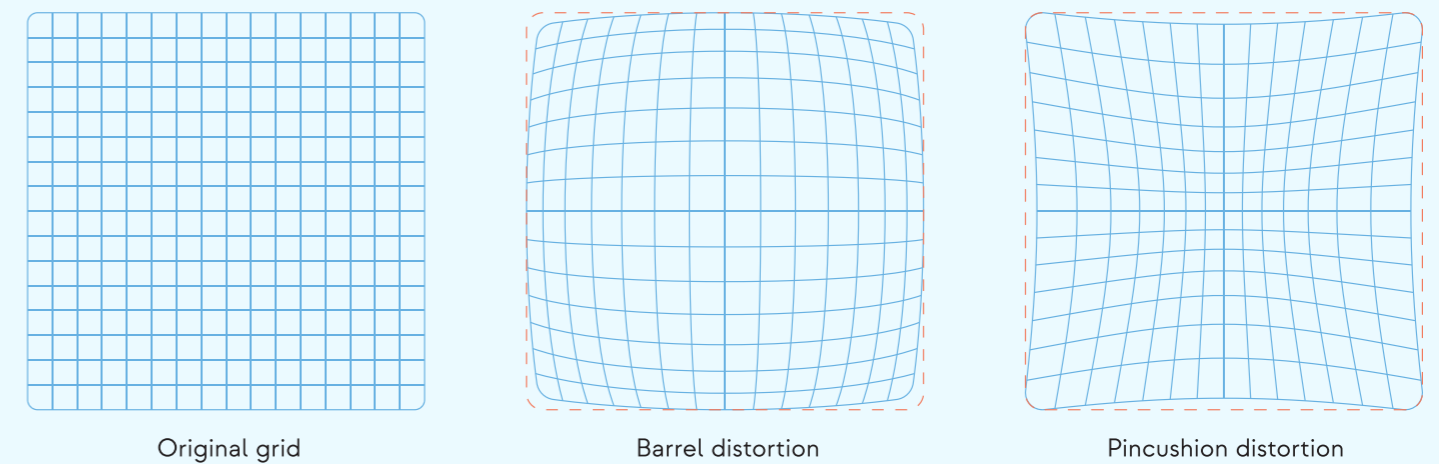


Figure 5.5 - Lens distortion possibilities.

## 5.2 Camera calibration

Retrieving quality results with the foot scanner is highly dependent on the calibration of the cameras. There are two types of calibration: intrinsic and extrinsic calibration.

### Intrinsic calibration

Intrinsic calibration is camera and sensor specific. When using generic off-the-shelf cameras, these are generally intrinsically calibrated in the factory. Custom made solutions require additional intrinsic calibration to achieve quality results. Intrinsic calibration contains parameters such as frame resolution, focal length and optical centers. This information is used to accurately map the camera coordinates onto the image plane, which is needed when constructing point clouds from depth information. These parameters are generally fixed, except when hardware changes to the lens or sensor occur. The intrinsic parameters can be expressed in a 3x3 matrix (Eq. 5.1) with parameters for the focal length ( $f_x$  and  $f_y$ , respectively), and the optical center ( $c_x$  and  $c_y$ , respectively).

$$Camera_{intrinsic} = \begin{bmatrix} f_x & 0 & c_x \\ 0 & f_y & c_y \\ 0 & 0 & 1 \end{bmatrix} \quad (\text{Eq. 5.1})$$

These intrinsic parameters can be used to correct possible lens distortion, where radial lens distortion is a common occurrence and results in either barrel distortion or pincushion distortion (figure 5.5).

### Extrinsic calibration

Extrinsic calibration is required when the 3D position of the camera relative to a certain global space is desired (Zhang, 2014), and contains parameters which describe an affine transformation of a point in a 3D coordinate system. The extrinsic parameters can be formulated in a 4x4 affine transformation matrix (Eq. 5.2) which describes rotation (the upper-left 3x3 sub-matrix) and translation (upper-right 1x3 sub-matrix) of the cameras relative to the global space:

$$Camera_{extrinsic} = T = \begin{bmatrix} a_{11} & a_{12} & a_{13} & a_{14} \\ a_{21} & a_{22} & a_{23} & a_{24} \\ a_{31} & a_{32} & a_{33} & a_{34} \\ 0 & 0 & 0 & 1 \end{bmatrix} \quad (\text{Eq. 5.2})$$

In the context of a 4D foot scanner, multiple point clouds are made from different camera views. The extrinsic parameters are used here to find the transformation matrices between these camera views and to transform and align the point clouds from different views into a global three-dimensional Euclidean space (which per definition only includes affine transformations). Using transformation matrices simplifies the act of aligning the multiple point clouds.

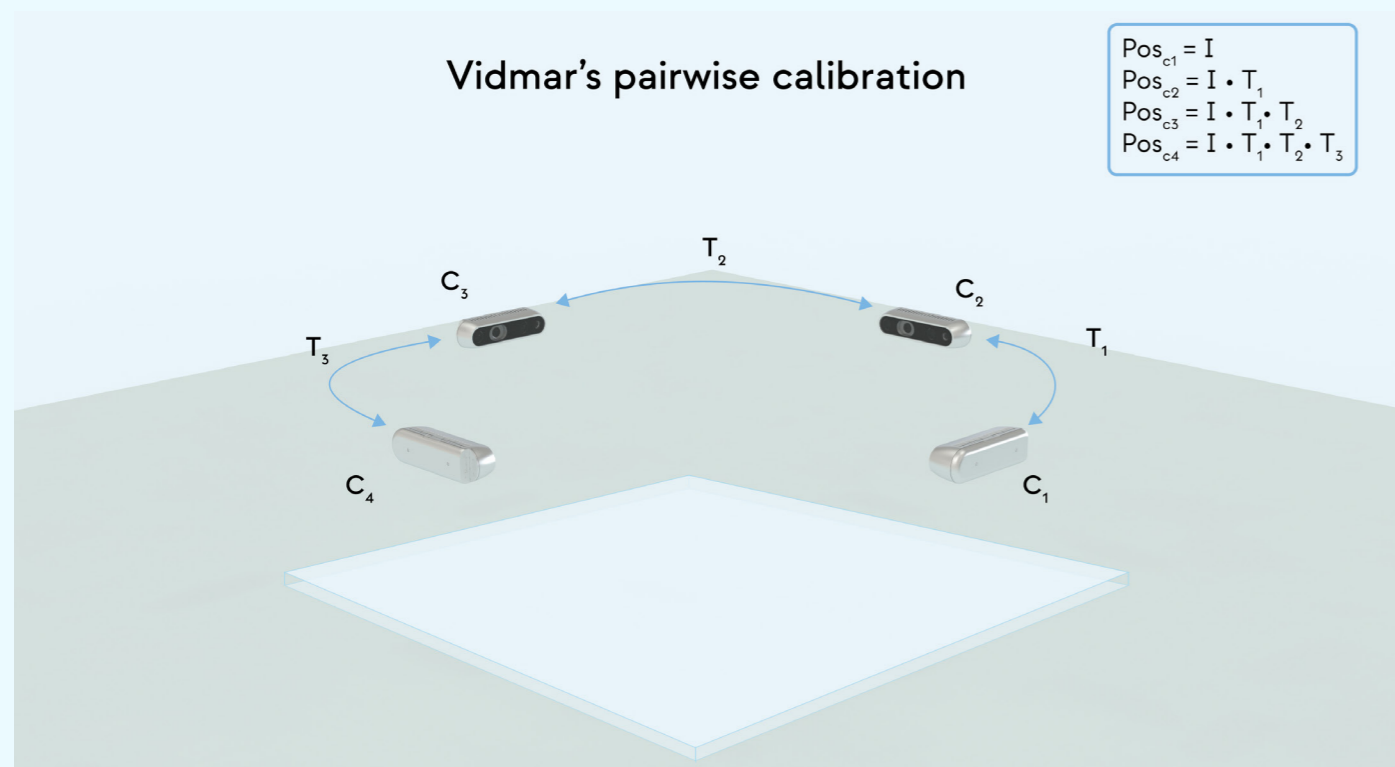


Figure 5.6 - Vidmar's pairwise extrinsic camera calibration approach.

### Vidmar's pairwise extrinsic camera calibration

In his thesis, Vidmar (2020) proposes an open-loop pairwise camera calibration method to be used to calibrate the extrinsic parameters of the cameras (figure 5.6). This approach was chosen since not all arbitrarily positioned cameras of the foot scanner are able to view the whole chessboard that is normally used for calibration. By calibrating the cameras pairwise, the relative transformation matrices between the camera pairs can be calculated, which then can be used to determine the physical location of a camera relative to the other camera in the pair.

Instead of a regular chessboard as used commonly in computer vision and calibration, a ChArUco board was used. Because of the unique identifiers on the chessboard, this board allows partial views and therefore, the dimensions of the board can be determined by all cameras. The ChArUco board can also be used for intrinsic calibration (OpenCV, 2021).

For the pairwise approach, Vidmar (2020) repositioned the ChArUco board for each pair in several ways, so the cameras would register the ChArUco board from multiple views (figure 5.7). This is needed to cover a

large percentage of the pixels of the camera, which is important in camera calibration. When adding more cameras to the scanner setup, the calibration time will take N times longer, since it is dependent on the amount of cameras and pairs in the system.

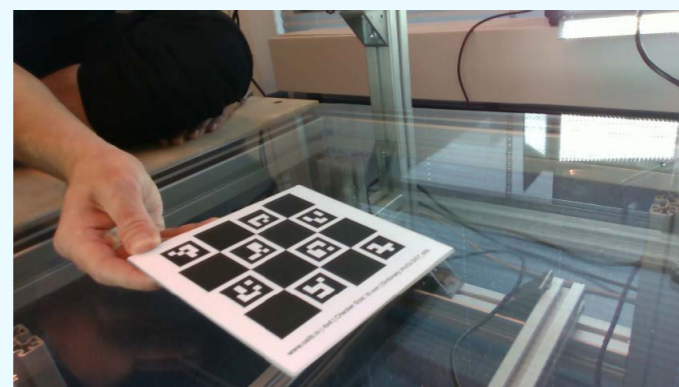


Figure 5.7 - Camera calibration using ChArUco target (Vidmar, 2020).

### Algorithm 1: RGB-D data acquisition (pseudocode)

- 1: Find connected device
- 2: Enable color stream
- 3: Enable depth stream
- 4: Set depth unit, exposure time, laser power for both streams
- 5: **while** *streaming* **do**
- 6:     wait for color+depth frame pair
- 7:     write color frame to a file
- 8:     write depth frame to a file
- 9: **end while**

## 5.3 Data acquisition

Algorithm 1 describes in pseudocode the data acquisition software pipeline that Vidmar (2020) used. It assumes a low-cost modular system architecture, where each module consists of a Raspberry Pi 4 and an external SSD for data storage for each camera module. This allows the system to have scalable capabilities depending on the desired performance and camera views, since each camera depends on the hardware capabilities of the Raspberry Pi, which drives each module. A challenge here is to synchronize all cameras to a global clock and initiate the system simultaneously so the independent camera views match their frame number with the other cameras in the system.

In total, four arbitrarily placed cameras on the frame above the transparent plate and around the volume of interest were presented. With this setup it is possible to (partially) capture the upper half of the foot, primarily focusing on the dorsal surface of the foot. The aluminium frame of the scanner also allows the positioning of additional cameras at the bottom to capture the plantar surface of the foot. Even though a modular system architecture was proposed, no documentation was found about implementing more than four cameras in the scanner. To acquire the whole foot (top part of the foot and also the plantar surface), it is likely that a minimum of five cameras are needed; four cameras to capture the top part of the foot, and one to capture the plantar surface. Thus, adding more than four cameras should be explored in order to properly acquire 4D foot data.

### Algorithm 2: data processing (pseudocode)

```

1:  for frameset = 1, 2, ..., N do           // N = Number of RGB-D framesets
2:      result ← null
3:      for each rgb_d_frame ∈ frameset do
4:          Parse the color and a depth frame pair (rgb_d_frame)
5:          Register depth to color
6:          Project resulting RGB-D frame to a 3D point cloud
7:          Transform point cloud with transformation matrix T of camera pair
8:          Append to result
9:      end for
10:     Write result to disk
11: end for

```

## 5.4 Data processing

Algorithm 2 describes in pseudocode the data processing software pipeline that Vidmar (2020) used. Trivial data processing was done, where the goal is to end up with understandable data from an outsider's perspective. Currently, the final resulting point cloud is only depending on pairwise calibration to transform and match point clouds from different camera views. Determining the accuracy of the scanner was done using third-party software (Geomagic Design X).

## 5.5 Camera frame rate

The proposed system had a frame rate limitation of 15 frames per seconds (fps) due to bandwidth restrictions. Because of this lower framerate, the scanner is only suitable for foot scanning at walking pace. Boppana and Anderson (2020) set their treadmill to an average speed of 1.4 m/s, based on the study of Browning et al. (2006), and showed the possibilities of connecting multiple Intel RealSense D415 cameras (six cameras) while carrying out data acquisition on 90 fps.

$$\text{Number of acquired frames} = \frac{\text{distance}_{walk} [m]}{\text{pace}_{walk} [m/s] \cdot \text{stance phase of gait cycle} [\%]} \cdot \text{frame rate}_{camera} [fps] \quad (\text{Eq. 5.3})$$

The dimensions of the transparent scanning plate on Vidmar's prototype are 600 x 600 mm. However, because this plate is supported by a frame with a thickness of 50 mm on all four sides, the effective dimensions of the plate when using bottom and top camera placement are 500 x 500 mm, or 0.5 x 0.5 m. With a scanning system framerate of 15 fps and a perfectly timed scanning sequence, the amount of frames for either phase (stance or swing) could be maximized.

As presented in the study of Mentiplay et al. (2018), the angular speed of the leg is the largest during the swing phase of the gait cycle, and the lowest during the stance phase. As suggested by the ankle angular velocity graph, and the study by Root et al. (1977), the swing phase is approximately 38 % of the whole gait cycle, whereas the stance phase amounts to 62 % of the gait cycle.

An estimation of the amount of frames per sequence can be made with equation 5.3. Assuming constant angular velocity of the hip during the gait cycle, the number of frames for registering the stance phase would amount to a total average frames per sequence of 8.

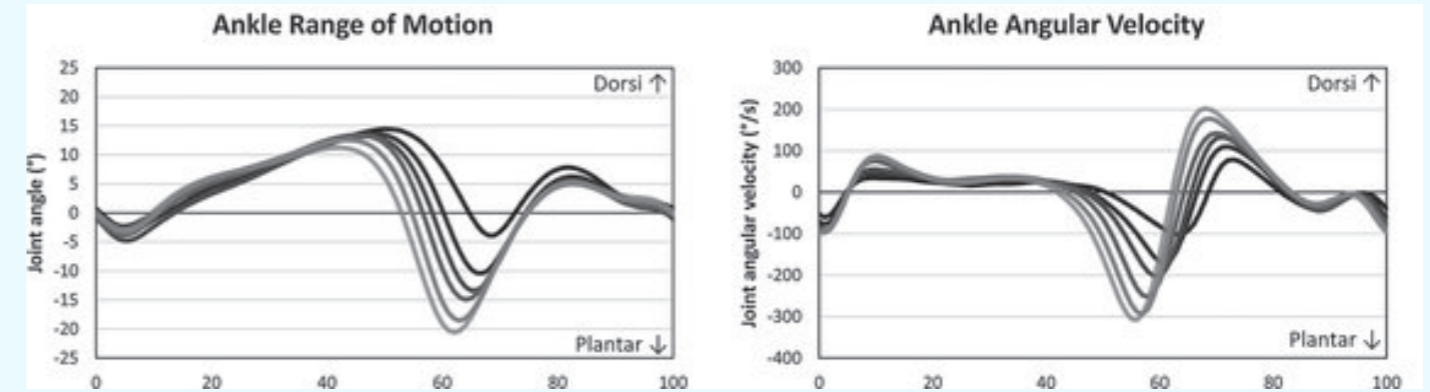


Figure 5.8 - The sagittal plane joint angle and angular velocity of the ankle during walking at various speeds. The x-axis projects the percentage of the gait cycle (Mentiplay et al., 2018).

It is expected that this number of frames is higher in practice, since the angular velocity of the hip is lower during the stance phase than during the swing phase (figure 5.8).

The study of Murray et al (1964) focuses on the walking patterns of normal men, and presents an average gait cycle duration of men between 0.98 and 1.07 seconds. Averaging this range, this amounts to 1.025 seconds per gait cycle, and 0.64 seconds for the total stance phase of 'normal men'. The study also shows that, for sixty normal men ranging from twenty to sixty-five years and in height from sixty-one to seventy-four inches, the stride length did not relate systematically with age. Thus, since the stance phase in a gait cycle amounts to 62 %, the stance phase duration of 'normal men' is approximated to 0.64 seconds.

With this information, combined with the ability to capture 15 frames per second (which is 0.067 seconds per frame), the amount of frames per sequence can be calculated using equation 5.4, which results in 9 frames per sequence.

$$\text{frames per sequence} = \frac{\text{stance duration} [s]}{\text{frame rate}^{-1} [fps]} \quad (\text{Eq. 5.4})$$

The calculation seems to be close to the calculation where the angular velocity is assumed to be constant. Therefore, it is assumed that 8 to 9 frames per acquisition can be captured with a frame rate of 15 for each camera. If the frame capture abilities of the scanner can be

improved, the scanner will be able to capture more states of the foot, which would allow for a more detailed motion analysis.

## 5.6 Scanning plate

In order to be able to register the plantar surface of a patient during a 4D scan, a camera/multiple cameras should be able to directly observe the plantar surface of the foot. It is preferred that the plantar surface can be registered before the heel strike and after the toe-off. As mentioned before, detailed data of a patient's plantar surface enables a podiatrist to design a fitting insole for a patient.

The transparent 600 x 600 mm, 15 mm extruded acrylic scanning plate (figure 5.1) is strong, but extremely bendable and susceptible to scratching, since it is a rather soft and flexible material (Granta EduPack, 2021).

Considering current 3D foot scanners (e.g. 3D Laser Foot Scanner by Voxelcare, Tiger scanner of Materialise Motion, iQube by Future Technology Systems) it seems that the industry standard for withstanding a maximum load is 200 kg. Since the 4D foot scanner could in theory also be used as a 3D foot scanner, the scanner should at least match this load bearing requirement.




## 5.7 Scanner component costs

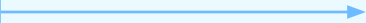
A total overview of the costs of Vidmar's scanner (2020) is included in table B.2 in Appendix B.2. The overview includes 5 cameras instead of the presented 4 cameras from Vidmar to give a more realistic cost representation of the scanner when enough cameras are connected to the system. The total component costs of the scanner amount to € 3.738.63, which is in the lower range of the prices that were mentioned in chapter 1. However, those prices are commercial prices, which include additional costs such as a profit margin, development, manufacturing costs, and transportation costs, but also marketing, insurance and storage.

## 5.8 Conclusion

In conclusion, the 4D foot scanner prototyping made by Vidmar (2020) is a solid foundation for further development. However, there are parts of the scanning process that need to be improved in order to end up with a proper 4D foot scan. Chapters 7 and 9 elaborate on the design challenges and requirements, respectively, that need to be achieved to end up with the desired project outcome: a proof of concept for 4D foot scanning within the context of podiatry.



# Define phase



The Define phase of this thesis describes the problem definition that is defined based on the evaluation of Vidmar's 4D foot scanning prototype (2020), the design challenges to improve upon this prototype, requirements to which the final scanner has to comply, and preliminary concepts.

## 06. Problem definition

The Exploration section presents many opportunities for developing a 4D foot scanner in the context of podiatry. Also, the function analysis of Vidmar's prototype (2020) from chapter 5 can be interpreted as a baseline state of the prototype. However, improving upon the accuracy of Vidmar's 4D foot scanner is an interdisciplinary problem which can be approached in numerous ways. Therefore, this chapter presents a problem definition to prioritize the focus of this project.

As mentioned in chapter 5, the implementation of post-processing software, such as an ICP algorithm (Iterative Closest Point), is expected to increase the quality and accuracy of the final scans. However, the data acquisition abilities of Vidmar's scanner prototype are questionable.

With 4 arbitrarily placed cameras above the scanning plate, it is not yet possible to capture the whole foot, since at least one more camera has to be added below the scanning plate to capture the plantar surface. Also, the maximized overlap between point clouds is likely too small to register a complete foot (described in chapter 12). Another point of concern is the frame rate of 15 fps, which would be able to only capture around 9 frames per acquisition for a 'normal man' subject walking at a pace of 1.4 m/s. With 8 stages in the gait cycle, and a non-linear angular velocity of the leg during the gait cycle, it is not possible to acquire an entire gait cycle in one acquisition run.

Furthermore, reproducible positioning of the cameras and their mounts is desired. Since the cameras are positioned close to the walkway, there is a risk that the camera modules are repositioned after use of the scanner. By designing camera mounts that can reproduce the initial position of the camera modules, no additional extrinsic calibration is needed when the position of the cameras is accidentally disturbed.

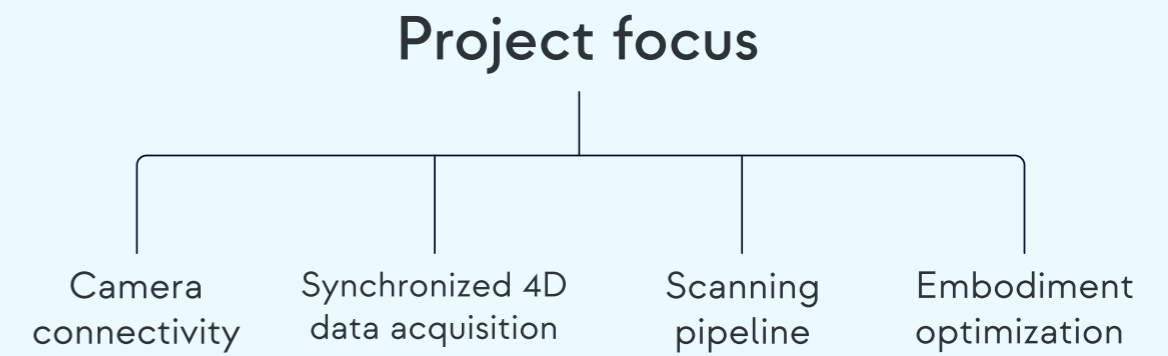
Lastly, the scanning plate is made out of acrylic, which deforms when a force is applied. This is highly undesirable when capturing the plantar surface, since

physical deformation of the scanning plate results in optical deformation and thus in deformed scanning results. In conclusion, a truly scalable data acquisition solution is not yet verified.

Without reliable and adequate 4D data acquisition and thus insufficient data, it will be difficult to construct (accurate) 3D foot models. Therefore, data acquisition first needs to be validated for a sufficient amount of cameras to capture a whole foot, before moving onwards to data processing. For this reason, this thesis prioritizes the development of the fundamentals of 4D foot scanning, which is to make 4D data acquisition possible for 5 or more cameras. In this context, this project can be considered a proof of concept for commercial 4D foot scanning.

## 07. Prototype identification

7.1	Camera connectivity	P. 56
7.2	Synchronized 4D data acquisition	P. 56
7.3	Scanning pipeline	P. 56
7.4	Embodiment optimization	P. 57



With the problem definition in mind, additional design challenges are formulated to support the development of the 4D foot scanner prototype and to fit it within the defined scope of this project. Attention is given to the following areas during development of the scanner:

- Camera connectivity
- Synchronized 4D data acquisition
- Scanning pipeline
- Embodiment optimization

## 7.1 Camera connectivity

Camera connectivity to a computer system, either desktop or single board computers (e.g. Raspberry Pi), is crucial in this scanning system. To acquire scanning data of a complete foot from different camera views simultaneously, the computer has to be able to manage the connections to all the connected cameras in a stable state. As stated before, the scanner would need at least five cameras to acquire scanning data of a complete foot. Therefore, the challenge is set to achieve simultaneous connectivity of five cameras or more.

The amount of cameras that can be connected and managed to one single system is restricted in three ways: The amount of PCIe ports that are available on the scanners' operating hardware; The maximum bandwidth that is tolerated by the operating hardware; The amount of power each camera demands from the system to be sufficiently powered. The final prototype has to take these limitations into consideration.

## 7.2 Synchronized 4D data acquisition

The scanning system relies on the simultaneous and continuous data acquisition of multiple cameras; i.e. all cameras acquire the same amount of frames within a predefined amount of time at the (exact) same time. With this, an arbitrary camera in the system captures the foot in the same position as the other cameras in the system for the same frame number.

Synchronized data acquisition is needed to properly align the point clouds from different camera views. If

the cameras are not able to simultaneously acquire the foot, the depth data of the feet for one camera will not match the other cameras in the system, which will make it difficult to generate an accurate 3D model of a complete foot. The amount of time between each frame acquisition per camera could influence the total accuracy of the 3D model of the foot.

Also, synchronized acquisition will benefit the processing of the data and usability of the scanner, since a specific frame for all cameras can be chosen to generate a point cloud from. If the frames of multiple cameras do not match, the operator has to manually guess the corresponding frames for each camera.

Therefore, to make the system manageable so that a specific frame number of one camera matches the frame number of any other arbitrary camera in the system, the time it takes to acquire one frame for all cameras should be:

$$t_{acquisition} [s] < \frac{1}{frame\ rate [fps]} \quad (\text{Eq. 7.1})$$

For instance, if the cameras are initiated with a framerate of 30 fps, the acquisition time should be within 33 ms for all frames of the camera chain. If all cameras are able to acquire a frame within 33 ms, then all cameras are able to acquire a frame within the same frame iteration.

## 7.3 Scanning pipeline

Acquiring RGB-D data from multiple cameras can be a quite demanding task on the hardware section of the scanner. There are two bottlenecks that should be considered:

- The bandwidth of the established connection between the cameras and the computer.
- The amount of available PCIe ports on the computer.

The challenge is to take these bottlenecks into consideration when selecting the hardware to run the whole system, and in the designing of the data acquisition pipeline.

An estimation of the data rate per sensor per device that is connected to the scanner can be made using equation 7.2. This data rate of each used sensor is dependent on three variables that are fixed during the initialization process of starting up the scanner: the number of pixels, the bits per pixel, and the frame rate of the sensors. The number of pixels is a product of the sensor resolution. The bits per pixel are dependent on the pixel format that is used during the initialization of the sensors. Worth noting is that the device data rate only estimates

$$device\ data\ rate [bit/s] = \sum_{i=1}^N n\_pixels_i \cdot bits\_per\_pixel_i \cdot frame\ rate_i \quad (\text{Eq. 7.2})$$

the bandwidth of the camera streams. It does not take any overhead communication into account such as the required bandwidth to establish communication between the cameras and the scanner.

The actual device data rate of the system is evaluated in Chapter 12.2. Limitations of the bandwidth are elaborated in appendix E.1.

## 7.4 Embodiment optimization

The quality of the data acquisition is not only dependent on the hardware and software. The embodiment design of the scanner has potential to assist in improving the quality of the scanning data as well in several ways.

### Scanning plate

The scanning plate used in Vidmar's prototype (2020) is a 15 mm extruded acrylic plate. Despite the thickness of the plate, the flexible properties of the material causes the

plate to bend when a load is applied towards the middle of the plate. Bending of the scanning plate will have a barrel distortion effect on the camera view when trying to capture the plantar surface of the foot. To prevent this, the final scanner should include a transparent and more stiff scanning plate. This would result in a more accurate and clean acquisition of the plantar surface.

There are several design considerations for choosing a suitable scanning plate. A study by Nilsson and Thorstensson (1989) shows that the peak amplitude for vertical reaction force increases for walking and running depending on the speed, ranging from 1.0 to 1.5 body weight (b.w.) and 2.0 to 2.5 b.w., respectively. Therefore, considering that the scope is focused on 4D foot scanning during walking in the context of podiatry, the scanner (and the glass plate) should be able to withstand a maximum load of 300 kg. By adding a safety factor of 33 %, an additional 100 kg is allowed, amounting to a total maximum load of 400 kg, 3924 N or approximately 4 kN. Furthermore, the biomechanical study of Vaverka et al. (2015), which assesses the gait analysis based on the ground reaction force, presents that the heel strike provides the largest ground reaction force during a gait cycle.

In addition, the study of Strzalkowski et al. (2018) determined a mean heel area of 38.8 cm<sup>2</sup>, or 3880 mm<sup>2</sup>. However, unfortunately this study does not present supporting data on the number of participants or anthropometric data (e.g. weight, height).

Concluding, the heel area in combination with the maximum desired load should be taken into account when selecting a scanning plate.

### Camera mounts

In Vidmar's setup, the cameras are mounted to the frame of the scanner with the RealSense provided ball mounts. These mounts are freely rotatable with 3 degrees of freedom (DoF) and can be fixed into a certain position.

The downside of ball mounts is that they are susceptible to movement even when fixed. Influences such as vibrations during walking, or a nudge to the camera could offset the position of the camera. Another drawback of ball mounts is that they cannot be accurately positioned. If the camera is moved (accidentally), it will be a challenge to reposition the camera to the exact same position.

By introducing a new camera mount that can be positioned with higher precision, cameras could be accurately positioned back into their initial place after being repositioned. Repositioning of the cameras should be done for example after a camera is accidentally bumped during a physical interaction with the scanner.

With control of the angle position of the cameras, it is easier to experiment with different camera views and to repeat the same positions. Lastly, it is helpful if the system depends on extrinsic camera calibration for initial alignment. If cameras are accidentally repositioned, the camera mount can be repositioned without recalibrating the system.

#### **Integrated reference points**

During a scanning process, the cameras are able to capture not only the target object, but also the surroundings. In this case, the embodiment of the scanner could be used as an advantage. Integrating unique reference points into the embodiment of the scanner could possibly support the extrinsic calibration process of the cameras and alignment process of the point clouds.

Benefits of integrated reference points would be:

An increased user experience, since extrinsic calibration can be done automatically;

More consistent scanning quality, since the scanner would be able to run regular automatic calibration sequences after a certain amount of scans.

Extrinsic calibration could be implemented as a closed-loop optimization algorithm that minimizes the error between the scanned distance and the known location of the integrated reference points.

## 08. Stakeholders



Figure 8.1 - The stakeholders that are related to this project.

Stakeholders of this project are determined based on the scope of the project. The stakeholder diagram in figure 8.1 visualizes the degree of involvement in this project. At the core are the stakeholders that are directly associated with this graduation project. This core consists of three stakeholders: the TU Delft (the graduate student, and the supervisory team), podiatrists and patients. The second and third layers consist of stakeholders

that are indirectly involved or that can benefit from the development of a low cost 4D foot scanner, i.e. potential users and target groups such as digital production partners, footwear manufacturers and researchers. In the future, orthopedic footwear solutions or articulate prosthetics that are designed after insights of 4D scanning data.

## 09. List of requirements

The problem definition and project goal have been translated into requirements and ambitions for the design of the 4D foot scanner within the context of this project. The requirements are divided into the following seven categories:

- Physical scanner specifications (PS)
- Camera system (CS)
- Data acquisition (DA)
- Data processing (DP)
- Scanning plate (SP)
- Medical Device and EU Regulations (MDR)
- Test and Calibration (TC)



### Physical scanner specifications (PS)

- PS.1: The commercial price of the scanner should not exceed €35,000.
- PS.2: The scanner should be accessible to users with a weight of up to 200 kg.
- PS.3: The scanner should include a walkway that is level with the scanning area.
- PS.4: The scanning volume should be large enough to accommodate considerable human variability. A volume of at least 2100 mm in height (Z axis), width of 1200 mm (Y axis) and depth of 1000 mm (X axis) is recommended (International Organization for Standardization, 2018).

### Camera system (C)

- C.1: The frame onto which the cameras are mounted should not be in direct connection with the frame on which the patient is walking with a maximum speed of 1.4 m/s (Boppana and Anderson, 2020)). Direct contact will cause vibrations that could move through the frame and influence the static position of the cameras during the gait analysis.
- C.2: The scanner should be able to capture the plantar surface of the foot during a 4D scanning sequence.
- C.3: The scanner should be able to capture the whole foot during the stance phase of the gait cycle in one scanning sequence.
- C.4: The scanner should be able to manage at least 5 cameras during 4D data acquisition.
- C.5: The scanner system should include camera mounts that can fix the position of the camera modules.
- C.6: The camera mounts should be able to assist in repositioning the camera modules back to their original position after the position of the camera modules is adjusted.
- C.7: The camera should be tested to determine if it is operating, and to determine its field of view. If there are multiple cameras, the output of each camera should be tested individually, before the images are registered (International Organization for Standardization, 2018).

### Data acquisition (DA)

- DA.1: The foot measurements of the final 3D mesh model, as a result of the static 3D scans of the foot, should have a minimal accuracy of 2 mm to conform to ISO 20685-1:2018 regulations.
- DA.2: The foot measurements of the mesh, as a result of the dynamic 3D scans of the foot, should have a minimal accuracy of 2 mm to conform to ISO 20685-1:2018 regulations.
- DA.3: The scanner should be able to capture the foot of a patient as a dynamic 3D scan where the patient is walking with an average pace of 1.4 m/s (Boppana and Anderson, 2020).
- DA.4: The static scanning process should not take longer than 20 s, to minimize movement artefacts (International Organization for Standardization, 2018).
- DA.5: The scanner should store the acquired scanning data in a raw numerical format for offline processing.
- DA.6: For each camera, the scanner should store each frame as RGB image and depth image (with a jet colormap applied for ease of depth interpretation) in JPEG format.
- DA.7: The acquisition time of all cameras in the system should be within one over the framerate of the system. E.g.: if the framerate of the system is 30 fps, the maximum system acquisition time should be within 0.033 seconds, or 33.33 ms.
- DA.8: The acquisition speed of one camera for one frame should be within the system acquisition time divided by the number of connected cameras. E.g.: if the framerate of the system is 30 fps and the system consists of 3 cameras, the acquisition speed of one camera per frame should be within 0.011 seconds, or 11.11 ms.

### Data processing (DP)

- DP.1: The processing software should be able to align RGB and depth data for reference purposes, as mentioned by W. ten Cate (personal communication, 21 April, 2021).
- DP.2: The processing software should be able to perform initial point cloud alignment.

- DP.3: The processing software should be able to isolate the depth data from the foot and clean up scanning noise.
- DP.4: The processing software should be able to clean up the depth data by applying additional filters.
- DP.5: The processing software should be able to smooth out the surface of the scanned foot by applying additional filters.
- DP.6: The processing software should be able to generate a point cloud of the raw data which is stored during data acquisition for a specifically selected frame.

### Scanning plate (SC)

- SC.1: The scanning plate should be able to withstand a dynamic point pressure of 4000 N, based on the study of Strzalkowski et al. (2018).
- SC.2: Deformation of the scanning plate should be minimized through material choice of the scanning plate.
- SC.3: To avoid disturbing the depth perception of the Intel RealSense camera, the scanning plate should not reflect infrared light.
- SC.4: The scanning plate should be as scratch resistant as possible.

### Medical Device and EU regulations (MDR)

- MDR.1: The definite foot scanner should comply with ISO 7250-1:2017 requirements.
- MDR.2: The definite foot scanner should comply with ISO 7250-2:2017 requirements.
- MDR.3: The definite foot scanner should comply with ISO 20685-1:2018. 3D body scanning requirements.

### Test and calibration (TC) - (International Organization for Standardization, 2018)

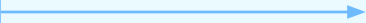
- TC.1: The scanner hardware should be calibrated when first delivered, and should be recalibrated periodically. The frequency of calibration should be related to the type of scanner and the frequency of use. Calibration should always be verified after moving the scanner.

- TC.2: The hardware should be tested with an object of known dimensions. While many different objects can be used, it is helpful to use an object some of whose dimensions are similar to those found in humans. The test object can be useful in verifying the scanning volume. As the test procedures recommended below involve placing the test object at various points within the scanning volume, it is helpful to have a test rig that can place the object precisely and reliably.
- TC.3: The following test measurements should eventually be made on a test object:
  - point-to-point distance;
  - arc length;
  - cross-section circumference.

The development of a commercial 4D foot scanner comes with a list of regulations and standards that the scanner has to adhere to in order to be used in a commercial and healthcare environment (NQA, n.d.). The most prominent ISO standards that the scanner needs to conform to, relevant to 3D body acquisition, measurement aspects and commercialization, are: **ISO 7250-1:2017/7250-2:2017, ISO 20685-1:2018, and ISO 13485:2016**. Further elaboration on these regulations and standards is provided in Appendix C.1.



# Development phase



The Development phase of this thesis highlights the prototype that has been made for this graduation project. The prototype is a proof of concept which showcases the possibilities of 4D data acquisition with low-cost commodity hardware. This would be the first development step towards a commercial ready 4D foot scanner in the context of podiatry.

## 10. 4D foot scanning concepts

10.1	Concepts	P. 70
10.2	Costs	P. 71
10.3	Conclusion	P. 71

Keeping the goal of developing a low-cost and accurate 4D foot scanner for podiatrists in mind, two concepts arose, which are detailed in this chapter. As pointed out in chapters 6 and 7, priority in development is given to the following areas of the foot scanner: the camera connectivity, the synchronized 4D data acquisition, the scanning pipeline, and the embodiment optimization.

The embodiment optimization includes an improved scanning plate, and newly designed camera mounts. Both concepts share the same configuration for this development area, since these are aspects of Vidmar's prototype that should certainly be improved. The proposed concepts vary in the other development areas and are presented in section 10.1.

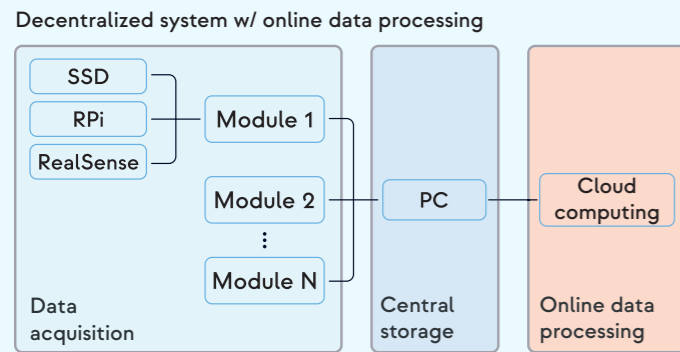


Figure 10.1 - Concept 1: A decentralized system with online data processing.

Centralized system w/ offline data processing

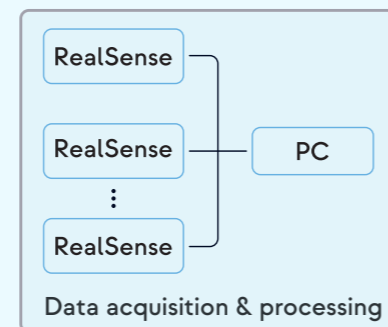


Figure 10.2 - Concept 2: A centralized system with offline data processing.

## 10.1 Concepts

### Concept 1

The scalable modular decentralized system which is presented by Vidmar (2020) is interesting for the context of this project since a scanner is configurable according to the preference of the podiatrist. A podiatrist would be able to choose their desired 4D foot scanner camera configuration and can always extend the performance of their initial configuration with more camera modules. Naturally, the price of the scanner would depend on the desired camera configuration. As has been established before, a bare minimal camera configuration would be 5 cameras, but it is most likely desirable for the data processing of the scans to have a larger camera configuration.

Concept 1 adds onto the existing 4D foot scanning prototype of Vidmar (2020). A schematic representation of the system configuration of concept 1 is visualized in figure 10.1. Compared with figure 5.3, concept 1 moves the data processing from the PC to the cloud. This way, no large initial investment into processing hardware is needed. However, adding online data processing to the system has two disadvantages:

- The transfer of data from the central storage to the cloud computing service takes time. Therefore, a quick scan-and-process workflow will be hard to realize.
- For a single acquisition, data needs to be transferred three times in order to end up with processed data (modules to PC, PC to cloud, cloud to PC). Added additional camera modules, increases the time complexity of the system linearly.

- Cloud computing is an additional variable cost component next to the costs of procuring the physical scanner.

### Concept 2

Concept 2 proposes a centralized system with offline data processing, as visualized in figure 10.2. Characteristic of this system is that it removes the implementation of scalable modules, which also removes the need for an extra SSD and Raspberry Pi 4 for every camera module and therefore reduces the cost. By adding the cameras directly to the PC, synchronization issues can be resolved more easily, since all cameras can be initiated from the same system. Also, a podiatrist can always choose to make use of cloud computing services for online data processing if needed.

System comparison between concept 1 and concept 2		
Concept	Advantages	Disadvantages
Concept 1	No investment in local processing hardware. Commodity hardware can be used for the Desktop PC.	The transfer of data from the central storage to the cloud computing service takes time. Therefore, a quick scan-and-process workflow will be hard to realize. For a single acquisition, data needs to be transferred three times in order to end up with processed data (modules to PC, PC to cloud, cloud to PC). Added additional camera modules, increases the time complexity of the system linearly.
	The system can be easily scaled up, depending on the desired configuration of the podiatrist.	Cloud computing is an additional variable cost component next to the costs of procuring the physical scanner. Synchronization between camera modules is challenging.
Concept 2	Faster processing pipeline, since the data is processed locally. No transfer times have to be taken into account.	Limited scalability due to hardware bottlenecks (e.g. available PCIe lanes on PC, bandwidth bottleneck during acquisition)
	Simplified system architecture: no individual modules with syncing complications	
	Extra USB PCIe card can be added to distribute camera connectivity load Option for cloud processing is always available	Investment costs into processing hardware

Table 10.1 - A system comparison of concept 1 and concept 2.

Cost comparison table - Vidmar (2020), Concept 1 & Concept 2				
Concept	Remarks	Product segment	Costs per segment (€) incl. VAT	Total concept costs (€) incl. VAT
Vidmar (2020)	Custom camera mounts not included.	Acquisition modules	€1,707.10	<b>€3,738.63</b>
		Desktop PC	€1,206.95	
		Embodiment components	€824.58	
Concept 1	Custom camera mounts and cloud computing not included.	Acquisition modules	€1,707.10	<b>€3,787.82</b>
		Desktop PC	€1,206.95	
		Embodiment components	€873.77	
Concept 2	Custom camera mounts not included.	Acquisition modules	€1,035.25	<b>€3,151.92</b>
		Desktop PC	€1,242.90	
		Embodiment components	€873.77	

Table 10.2 - Cost comparison of Vidmar (2020), concept 1 and concept 2.

Disadvantages of this system is that the scalability of the scanning system is limited due to hardware bottlenecks, such as the number of available PCIe lanes on the PC, and the bandwidth bottleneck during data acquisition. Another considered disadvantage is that the purchasing costs of the scanner are likely to be higher compared to concept 1. This is because the PC of concept 2 has to be powerful enough to process the acquired data, whereas the PC of concept 1 can be any generic PC with enough data capacity to store the acquired data.

Table 10.1 compares the advantages and disadvantages of both the concepts with the focus on the proposed systems.

## 10.2 Costs

Table 10.2 presents a comparison overview of the costs of both concept 1 and 2, compared to the system of Vidmar (2020). Since the hardware components of the Desktop PC are relatively old, their price is indicated by their last retail price.

To make a fair comparison, the camera configuration for all concepts was set at 5 connected cameras. This is also related to requirement C.4, stating that a scanner setup should have a minimum camera configuration of 5 cameras. Also, for both concepts, the same Desktop PC is used in the comparison. With the exception of an additional USB PCIe card that is added to the Desktop PC configuration of concept 2.

Compared with the prototype of Vidmar (2020), the scanning plate which is included in the embodiment

components is replaced with a glass plate.

As mentioned in the remarks, the custom camera mounts are not included in the estimation of the scanner costs.

Also the cloud computing costs are not included for concept 1, since these costs vary depending on the usage of the cloud computing service. It is therefore expected that the scanner costs including the cloud computing will increase for concept 1.

## 10.3 Conclusion

From comparison table 9.1 and the cost comparison of table 9.2, concept 2 has preference over concept 1. Not only is concept 2 cheaper than both concept 1, as well as the prototype of Vidmar (2020), but the advantages also outweigh the advantages of concept 1. Note that the same Desktop PC configuration is used for all concepts. Since concept 2 relies on offline data processing in a centralized system, it is recommended to upgrade the hardware of the Desktop PC for faster processing.

## 11. 4D foot scanning concepts

11.1	System configuration	P. 75
11.2	Cameras	P. 75
11.3	Scanning plate	P. 78
11.4	Custom camera mount	P. 81
11.5	Trigger system (Human Computer Interaction)	P. 83
11.5.1	Functionality	P. 83
11.5.2	Positioning	P. 87
11.6	External lighting	P. 89
11.7	Pricing	P. 91

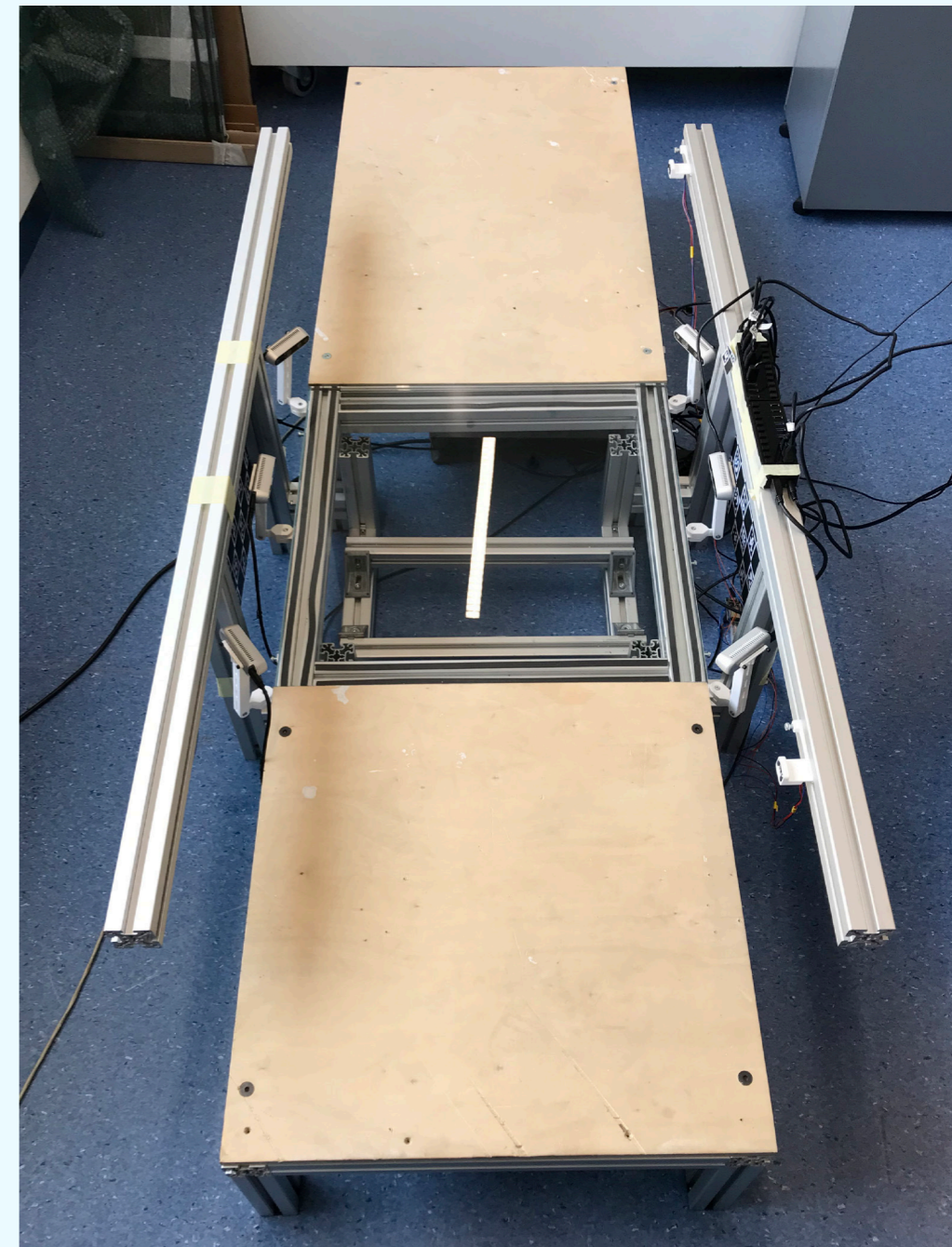


Figure 11.1 - A photo of the 4D foot scanning prototype in its final configuration.

This chapter presents the 4D foot scanning prototype that has been built during this graduation project. The scanner used the embodiment of Vidmar's (2020) 4D foot scanner prototype as a starting point. From there, further development and iterating was done on the sections as described in chapters 6 and 7. The result is a scanner that is able to acquire 4D foot scanning data, both in a static and dynamic setting. The physical working prototype is shown in figure 11.1.

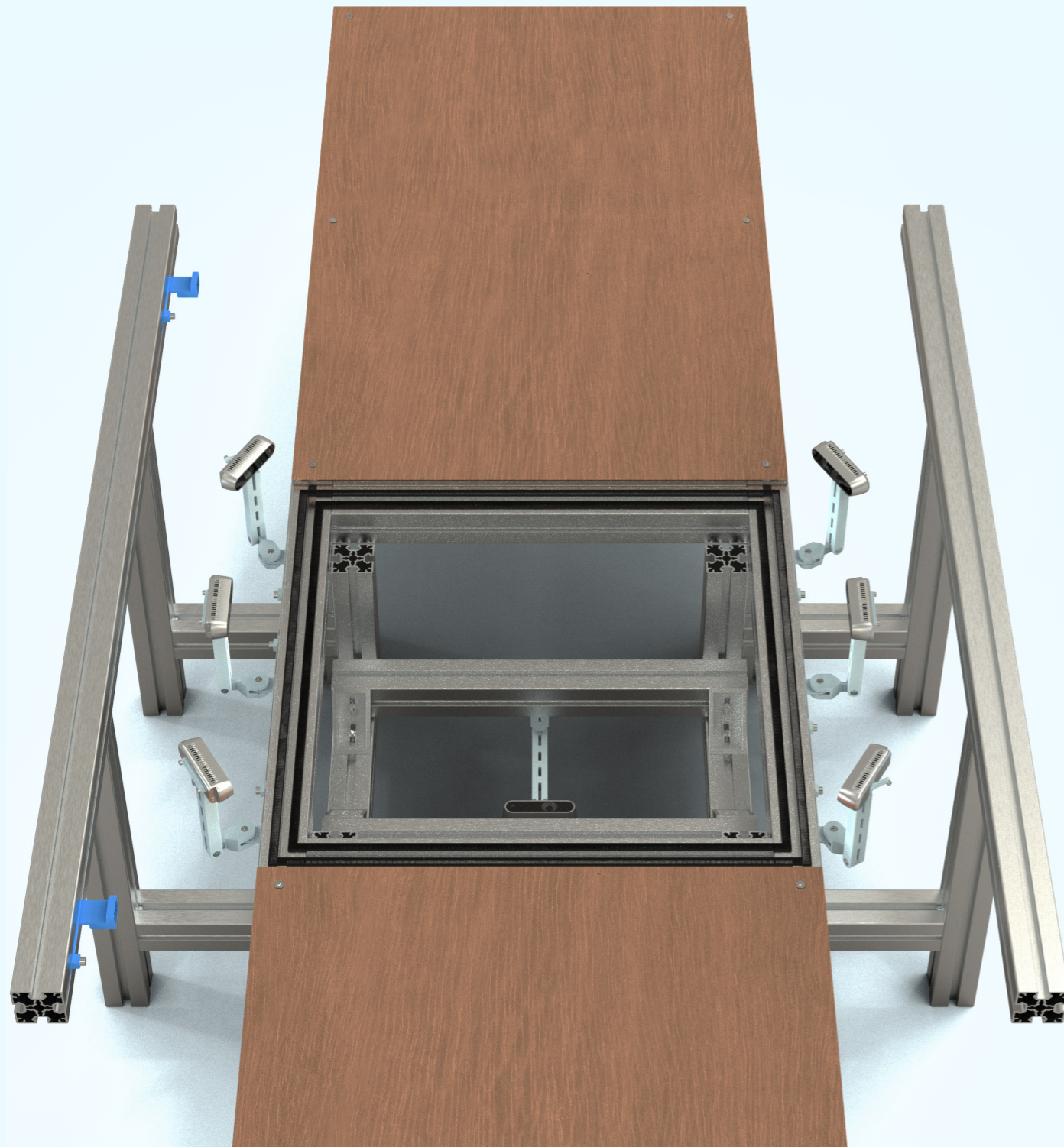


Figure 11.2 - A rendered image of the final scanner prototype, with the cameras placed around the glass scanning plate.

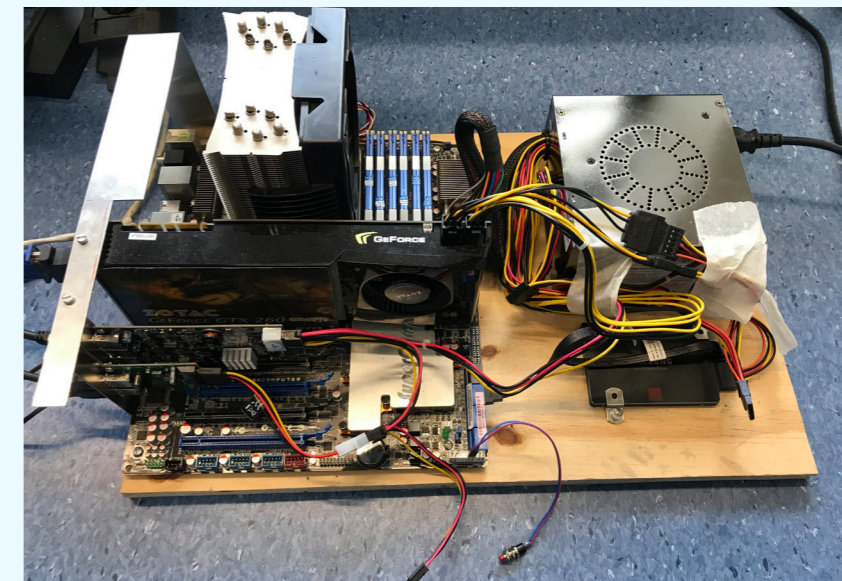


Figure 11.3 - The floor computer used in the scanner for data acquisition and processing.

### Dimensions

Compared to the scanner of Vidmar (2020), the walkway measurements of the physical model are the same: a 600 x 600 mm walkway platform, a 600 x 1000 mm walkway platform, and a 600 x 600 mm glass scanning plate platform. In the render of figure 11.2, both walkway platforms are 600 x 1000 mm to provide enough room for the patient to stand and walk comfortably on the scanner.

All scanner functionalities are programmed using Python 3.8. The scanner utilizes the pyrealsense2 library, which is a wrapper library for the Intel RealSense SDK 2.0 to access functionalities of the Intel RealSense™ cameras.

## 11.1 System configuration

Since the goal is to develop a proof of concept of 4D data acquisition, the data acquisition and processing is done with the custom-built computer from Vidmar's project (2020), shown in figure 11.3. The computer consists of: an Intel i7 920 processor, 4 GB DDR3 RAM, a 4-port StarTech USB 3.1 Gen 2 PCI expansion (PCIe) card, a 2-port StarTech USB 3.1 Gen 1 PCI expansion card, and a Samsung EVO 850 SSD disk.

The cameras are connected to the scanner via two Sabrent 7-Port USB 3.1 hubs (HB-B7C3), which provide 60 W (12 V, 5 A) of external power. The Sabrent USB hubs connect to the system via one of the USB PCIe cards via USB 3.1, which has a maximum data rate of 5 Gbps.

With this configuration, a single Sabrent USB hub is able to manage a 6 camera configuration. When connecting more than six cameras to the scanner, it is important that each USB hub is connected to their own USB PCIe card, and one USB PCIe card has at most 6 connected cameras, to prevent bandwidth issues.

Vidmar's (2020) modular single board computer system design was discarded for development of the scanner, because of their inconvenient setup. The bottleneck with using Raspberry Pi modules in a prototyping environment is that they have to be initiated simultaneously and configured individually, which increases the complexity of running easy scans.

## 11.2 Cameras

The final scanner is able to manage and control 9 Intel RealSense D435i cameras simultaneously. However, testing and scanning was mostly done with a 7 camera configuration, since positioning of the cameras was more convenient. A possible camera positioning configuration is shown in figure 11.4. The cameras are positioned around and beneath the transparent scanning plate, and both the RGB and depth sensor streams are initialized with a 848 x 480 px resolution and frame rate of 30 frames per second.

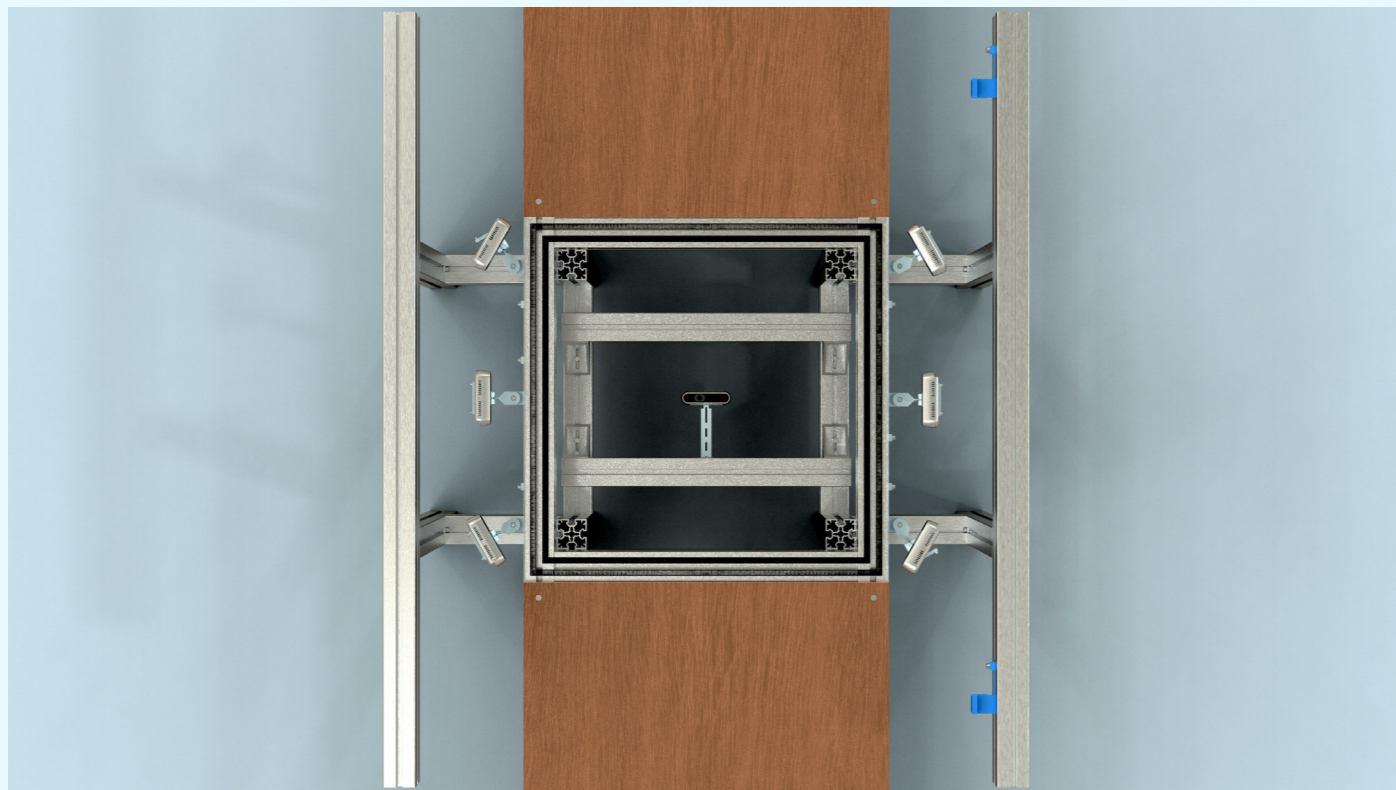


Figure 11.4 - The 4D foot scanner with a camera configuration of 7 cameras, where the cameras are positioned around the glass scanning plate.

### PCIe ports

Connecting multiple Intel RealSense cameras to commercially available off-the-shelf computers is a challenge. A Dell XPS 15 9560 laptop (Intel Core i7-7700HQ processor, 32 GB RAM, GTX GeForce 1050i graphics card and a Toshiba 1 TB SSD) shows stable performance with up to four connected cameras, but fails to maintain connection with more cameras connected.

Using the floor computer (figure 11.3) with the 4-port StarTech USB 3.1 Gen 2 PCIe card, the system shows stable camera performance for up to 6 cameras with active RGB and stereo streams for all cameras, with aforementioned initialization specifications. This PCIe card is connected to the system via a PCIe 4x slot.

The addition of another 2-port StarTech USB 3.1 Gen 1 PCIe card allows it to even connect 9 cameras with active sensor streams for all cameras with aforementioned initialization specifications. This PCIe card is connected to the system via a PCIe 4x slot. Due to a lack of cameras, a larger camera configuration is not tested.

### Bandwidth

Simultaneous data acquisition of all cameras puts a strain on the bandwidth capabilities of the hardware. This strain is distributed by the addition of the two USB PCIe cards. The 4 USB port StarTech USB 3.1 Gen 1 PCIe card has two USB controllers and is capable of acquiring data with speed of up to 10 Gbps per USB controller, in total of 20 Gbps. However, the maximum data rate of a USB 3.1 port is 5 Gbps. Therefore, since the hub is only connected to one USB port, the maximum bandwidth is limited to 5 Gbps.

Because of the PCIe 1x connection, the 2 USB port StarTech USB 3.1 Gen 2 PCIe card has a maximum data rate of 5Gbps. Appendix E.1 contains further clarification on the bandwidth limitations with USB connected cameras.

Because of the PCIe 1x connection, the 2 USB port StarTech USB 3.1 Gen 2 PCIe card has a maximum data rate of 5Gbps. Appendix E.1 contains further clarification on the bandwidth limitations with USB connected cameras

Bandwidth consumption per sensor at 30 fps							
Type of sensor	Image resolution (pixels)	Frame rate (fps)	Image format	Number of pixels per sensor	Bits per pixel	Device data rate [bps]	Device data rate [Mbps]
RGB sensor	848 x 480	30	BGR8	407040	24	293068800	293.069
Depth sensor	848 x 480	30	Z16	407040	16	195379200	195.379

Table 11.1 - The bandwidth consumption per sensor at a frame rate of 30 fps.

Bandwidth consumption per camera configuration		
Camera configuration	Calculated bandwidth consumption [Mbps]	Calculated bandwidth consumption [Gbps]
1	488.448	0.488
4	1953.792	1.954
6	2930.688	2.931
7	3419.136	3.419
9	4396.032	4.396

Table 11.2 - The bandwidth consumption per camera configuration, based on the camera initialization as shown in table 11.1.

An estimation of the total device data rate of the scanner can be made using equation 7.2, in chapter 7.3.

Both the RGB and depth sensors for all cameras are initiated with frame rate of 30 fps. The sensor resolution is set to 848 by 480 pixels, which amounts to a total of 407.040 pixels.

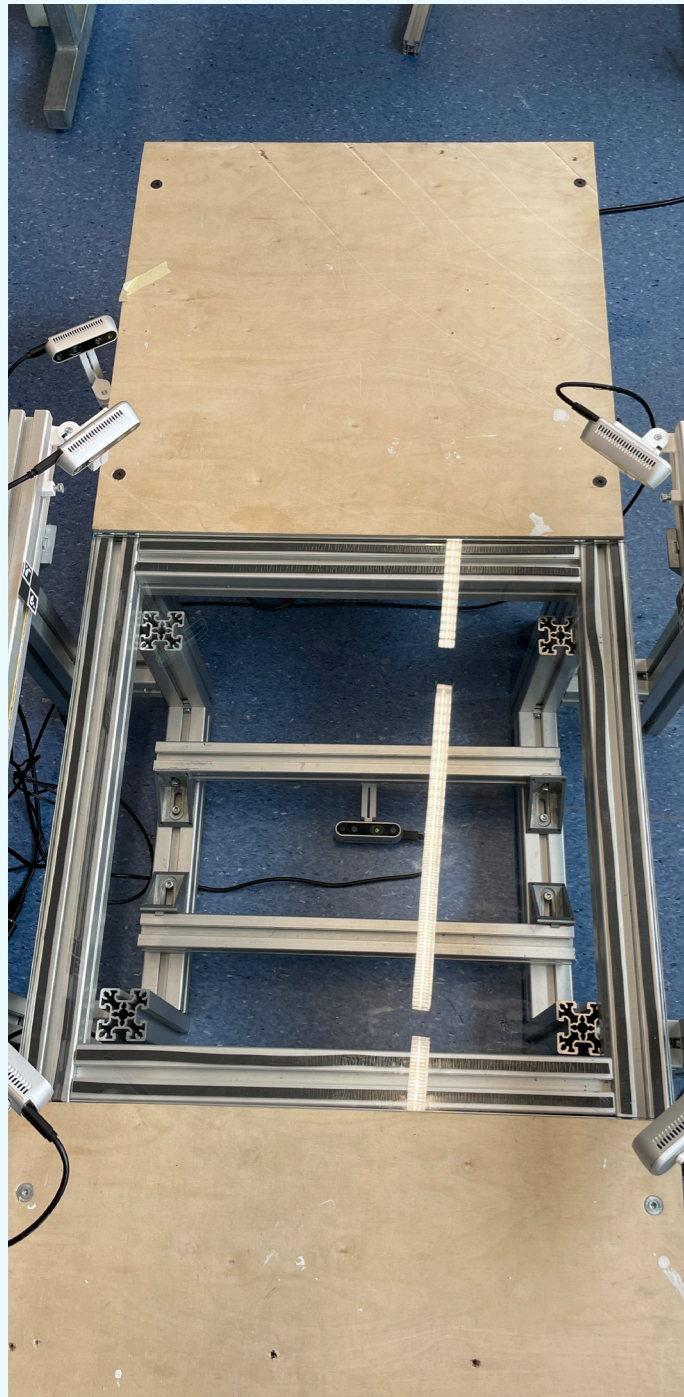
The RGB sensor is initiated with a BGR8 format, meaning that 8 bits are used per color per pixel. Thus, every pixel in the RGB frame is represented by 24 bits (Basler, 2021). The depth sensor is initiated with the Z16 format, which needs 16 bits per pixel (The Linux Kernel, n.d.).

As presented in table 11.1, for each camera, the data rate consumption of the color sensor stream amounts to 293.069 Mbit/s, and the data rate of the depth sensor stream amounts to 195.379 Mbit/s. Table 11.2 presents the bandwidth consumption for different camera configurations. The 4 camera configuration is mentioned because Vidmar's 4D foot scanner included 4 cameras. The 6 camera configuration is mentioned because this is the maximum number of cameras that a single USB PCIe card is able to manage.

Remarkable is that the camera configuration with 7 cameras has an estimated bandwidth of 3.419 Gbit/s, whilst both USB PCIe cards are able to manage a camera configuration of up to 6 simultaneously initialized cameras. As mentioned before, for both USB PCIe cards, the maximum bandwidth is still bounded by the maximum bandwidth over USB 3.1, which is 5 Gbps. The bottleneck of connecting more than 6 cameras to a single USB 3.1 port is either not possible because of a limited number of PCIe lanes, or because an exceeding bandwidth consumption caused by overhead communication of the cameras.

### External power

Experimenting with powered and unpowered USB hubs shows more stable connectivity of multiple cameras when an external power supply is used. From testing, the 60 W external power supply is able to support at least 7 cameras. An explanation for this is that the current supply is not sufficient for a multi camera setup of more than 4 cameras. Elaboration on the power consumption of the cameras can be found in Appendix E.2.



### 11.3 Scanning plate

Within the context of podiatry, the requirement was made to support users of up to 200 kg in the context of walking. To answer this requirement, the final scanner is fitted with a tempered ClearVision low-iron glass plate from AGC's Planibel Extra Clear glass collection (figure 8.5). This type of glass is known for its high light transmission rate (92% for 6 mm).

The glass plate has a nominal thickness of  $12 \pm 0.3$  mm and a width and height of  $600 \pm 2$  mm and  $600 \pm 3$  mm, respectively. These dimensions match the scanning plate support platform of Vidmar's (2020) 4D foot scanner setup.

Glass was chosen over polycarbonate (PC) or polymethyl methacrylate (PMMA) because of their sensitivity to scratching. It is desired to have a durable scanning solution, which also includes the quality of the scanning surface. Since glass has excellent scratch resistant properties and the scanning plate has constant interaction because users walk on it, glass is chosen over other materials.

Based on these specifications, a dynamic force analysis was done by M. Spijker (personal communication, 15 April, 2021) to validate the use case of the glass plate. The conclusion is that the glass plate can easily hold 200 kg users. Appendix E.3 includes the dynamic force analysis of the glass plate within the use context, along with in-depth properties of the glass and glass related design considerations.



Figure 11.5 - The tempered soda-lime low-iron glass scanning plate.





Figure 11.6 - Two different camera mount sizes. (left) a high mount to position the camera above the scanning surface of the scanner when mounted on the side of the scanner. (right) a lower mount to be positioned on the side beams that run along the side of the scanner walkway.

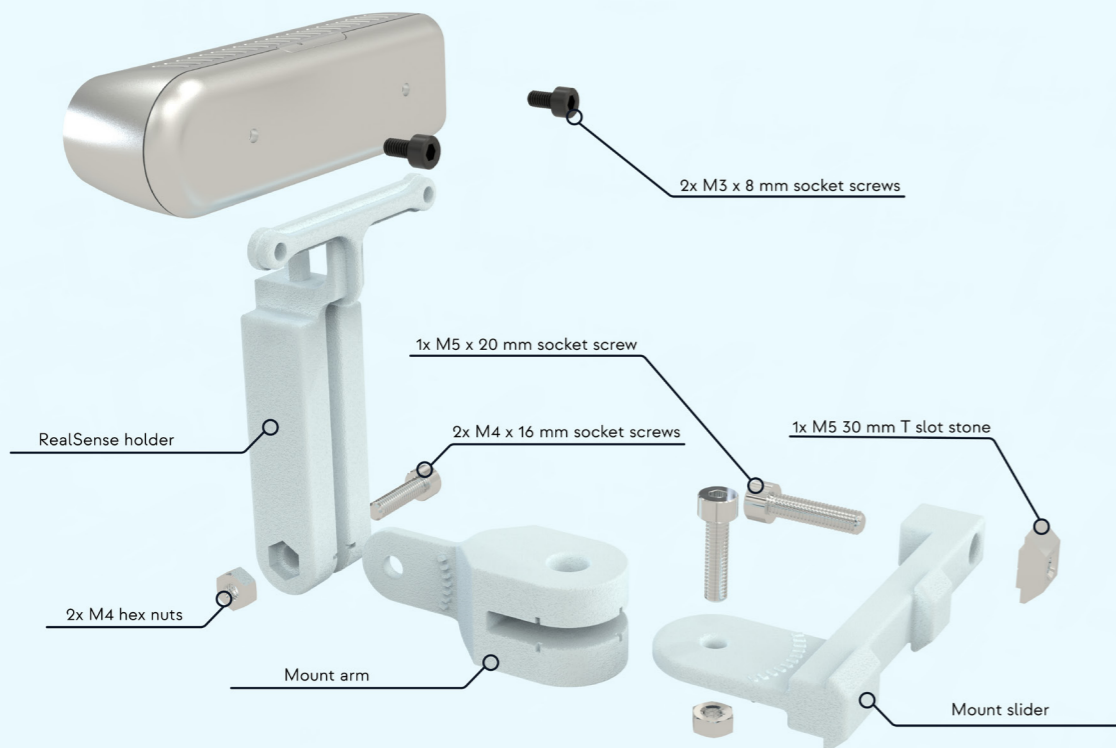


Figure 11.7 - An exploded view of the camera mount with all its components labeled.

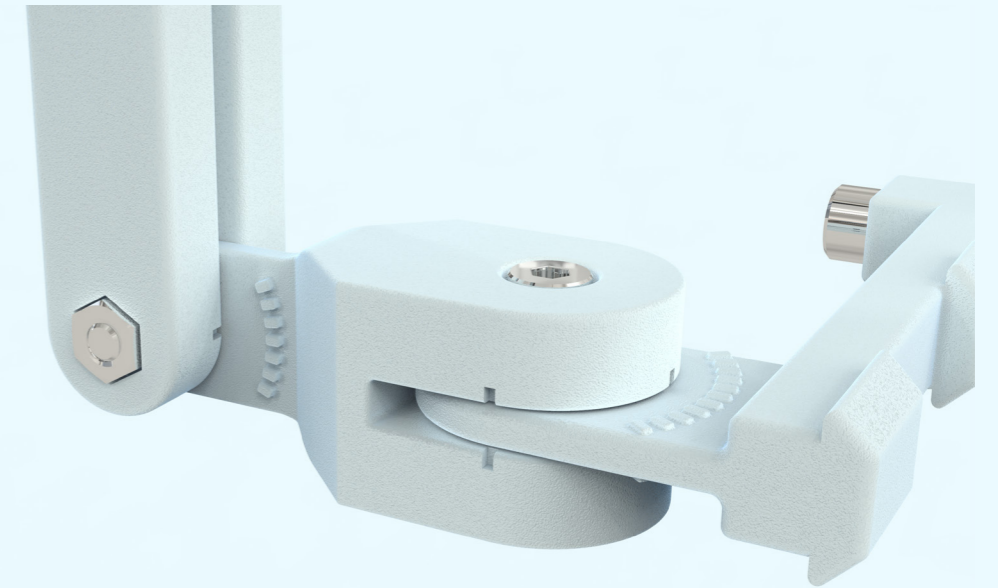


Figure 11.8 - A close up of the extruded ridges on the 3D printed parts of the camera mount.

## 11.4 Custom camera mount

The purpose of redesigning the camera mounts was to be able to position and reposition the cameras more precisely compared to the camera ball mounts that are included with the Intel RealSense cameras. In case the cameras are (accidentally) repositioned, the camera position can be restored again to its former position. This function not only helps in achieving scans with consistent views over time, but also allows the operators to experiment with different camera positions and replicate these positions more accurately.

If extrinsic camera calibration is implemented in the future, accurate camera positioning could also be helpful. If the camera positions are changed after calibration, the system generally has to be recalibrated. However, if the cameras can be repositioned to their original position, extrinsic recalibration is not needed as often or might not even be needed at all after initial extrinsic calibration.

The result is a camera mount that has 2 Degrees of Freedom (DOF), which minimizes the complexity of rotation along the y-axis which is not needed in the scanner setup. The camera mounts are designed in such a way that it can be configured with different camera holder lengths (figure 11.6). The mount can be attached to the outside of the aluminium frame of the scanner with the longer holder. This is to increase the distance between the scannable object and the cameras, which is a good thing since this prevents the user from moving too close to the cameras during data acquisition. Also, the cameras are not positioned in the same walking area of the user anymore, which leaves more room open for the user to walk comfortably along the walkway.

The camera mount consists of three parts that can be 3D printed using Fused Deposition Modelling (FDM) printing. Connecting the parts is done using off-the-shelf fasteners, as shown in the exploded view (figure 11.7). Appendix E.4 elaborates on this.

The parts of the mount contain small extruded indicators on the rotational points where the parts connect to other parts (figure 11.8). The ridges can be aligned with the small cut outs in the connecting part. By aligning the indicators on one part with the cutouts on the connecting other part, an operator should be able to replicate the relative position of the two parts. The step size of the indicators is 6.43 degrees (equal distribution of 71 mm wide indicators across a 45 degree angle, since this allows the mount to be 3D printed with clear indicators using FDM printing with a 0.4 mm nozzle).

It is recommended to further decrease the step size of the indicators to allow more accurate repositioning. However, other ways of manufacturing should be reviewed to achieve the best and most accurate step size. For example injection molding or SLA/SLS printing.

Additionally, with data processing and automatic data alignment in mind, the custom camera mounts are designed in such a way that consistent camera angles between the cameras and the glass plate can be achieved. Having a common angle between the cameras that are positioned around the glass plate and the glass plate might benefit the alignment processes of the point clouds.

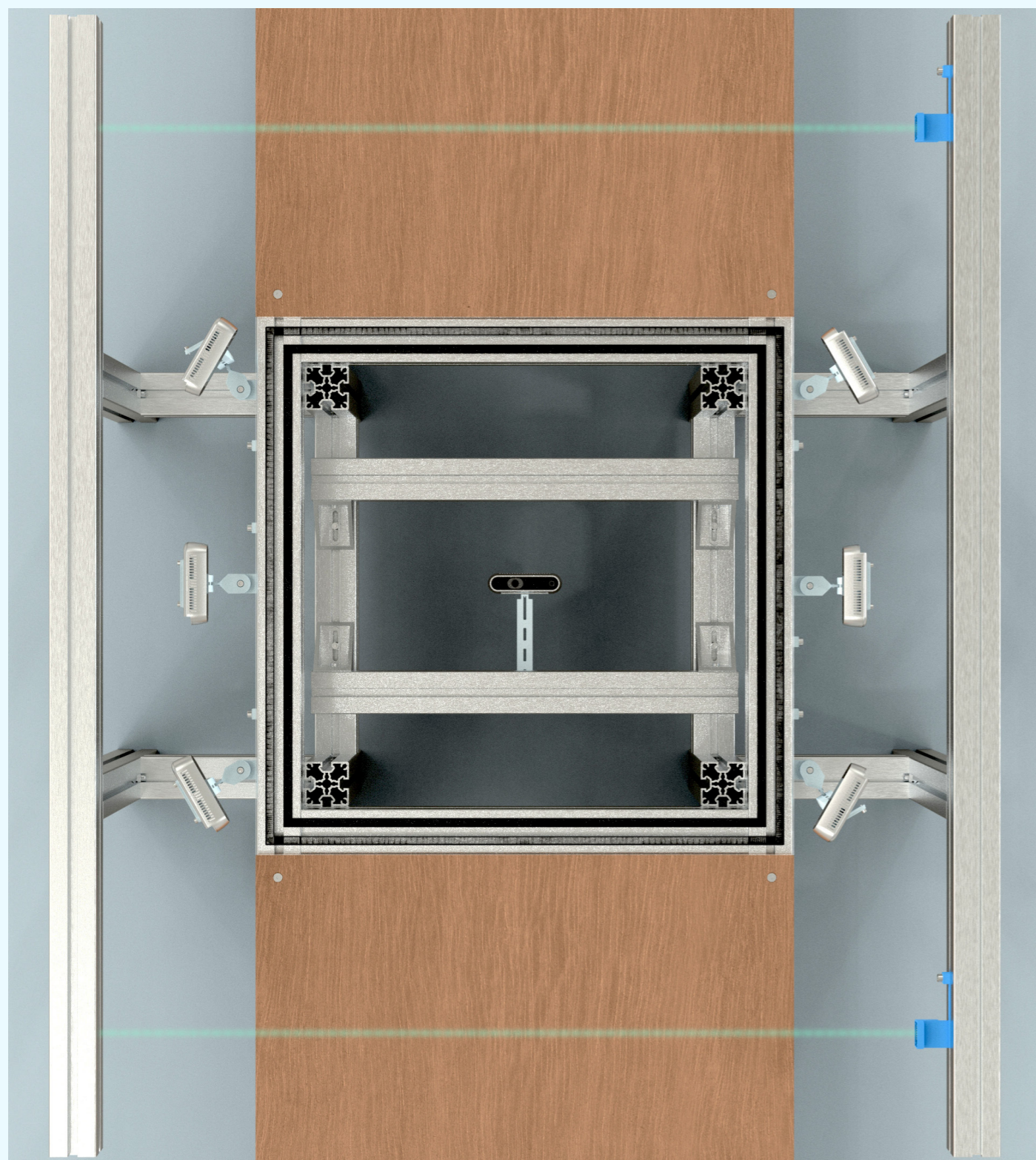


Figure 11.9 - A visualization of the trigger system when mounted onto the 4D foot scanner. The green lasers that are emitted from the trigger mounts act as trip wires and send information to the scanner.

## 11.5 Trigger system (Human Computer Interaction)

Dynamic foot scanning requires the ability to acquire camera data during a particular period of time in order to capture the complete gait cycle. Timing the start and end of a scan is essential in this process. The most straightforward approach to this problem is to predefine a fixed acquisition time of a dynamic scan and start the scanning process manually. This approach has three drawbacks:

- The predetermined acquisition time should be adjusted to the walking speed of the patient, i.e. a longer acquisition time is needed for patients who have trouble with walking (e.g. elderly or people with an adjusted gait);
- If the patient has a faster gait pace than the predetermined acquisition time, the patient will finish their gait before the system stops the acquisition. The result is acquired frames that are 'empty' (not containing any foot data), and can be considered as data that is unnecessarily occupying valuable memory- and data capacity of the scanner. Additional data cleaning is needed by the operator to remove unusable data;
- The operator has to time the initiation of the dynamic scan properly, taking the reaction time and gait pace of the patient into account. Incorrect timing of starting the scan could result in an incomplete scan. A redo of the scan and/or adjusting the acquisition time might be necessary.

Resolving the presented drawbacks will likely result in an improved user experience of the scanner. A solution is proposed and implemented, which introduces a human-computer interaction between operator and the scanner system with the following goals in mind:

- Improving the user experience by relieving the operator of timing concerns;
- To allow for automatic dynamic acquisition times, to comply with varying gait speeds;
- To minimize the amount of data occupancy due to 'empty' frames;
- The response time of the trigger system to detect motion should be as fast as possible in order to be

able to detect movement;

- The response time between the trigger system and the scanner should be minimized to avoid loss of acquisition data.

The presented trigger system proposal is for showcasing and proof of concept purposes, and is not optimized for performance, costs or manufacturing. Therefore, the trigger system consists of ready-made prototyping components.

### 11.5.1 Functionality

The trigger system has two tasks: notify the 4DFS system when to start data acquisition, and notify the 4DFS system when to stop data acquisition. The 4DFS system is only notified when patients move past a certain point on the foot scanner walkway. From this description, a one-way communication from the trigger system to the 4DFS system would be sufficient to achieve the goal of the trigger system. Critical with the implementation of this trigger is a fast communication speed between the two systems in order for the 4DFS system to start the data acquisition before the gait cycle of a patient begins.

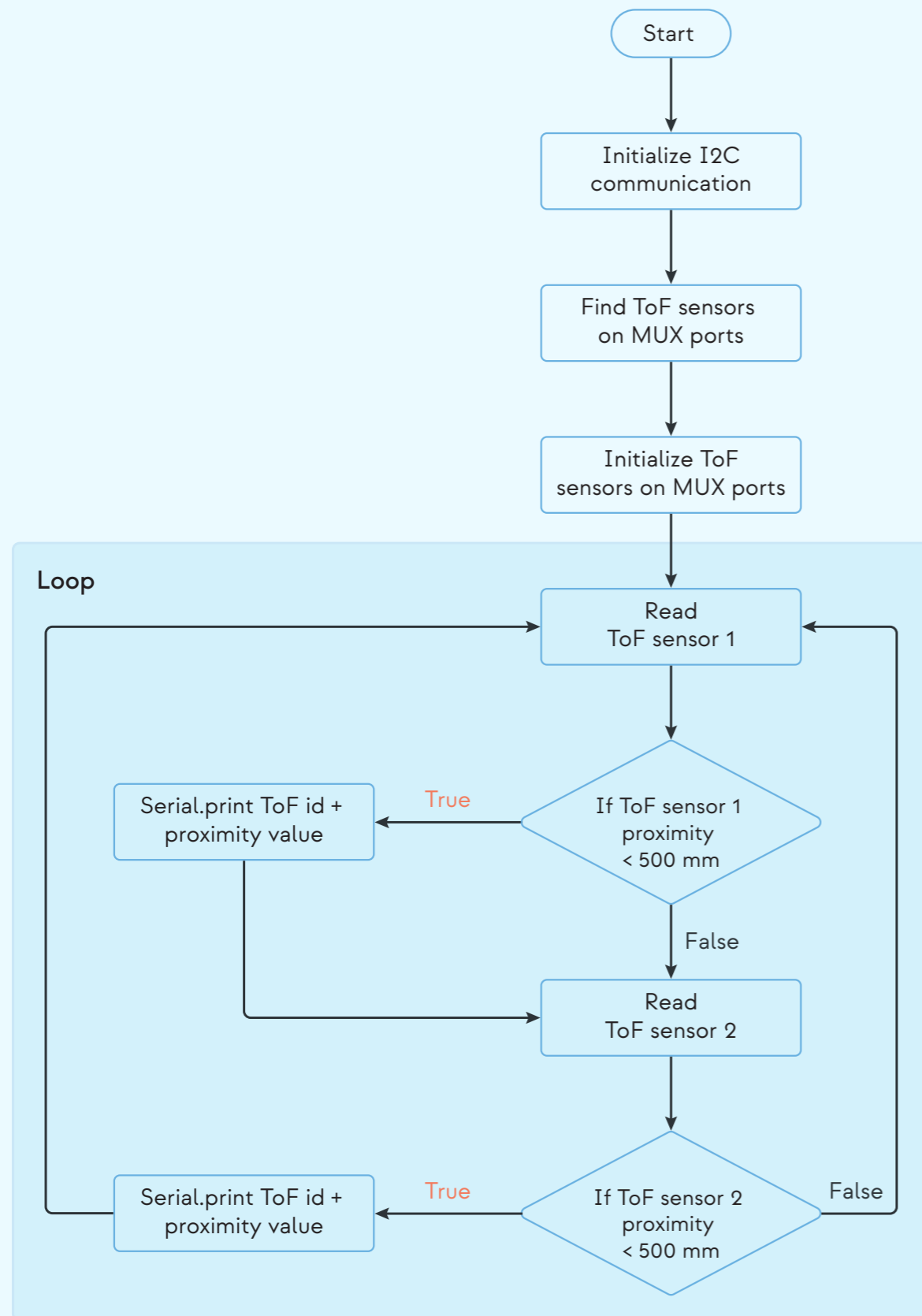


Figure 11.10 - Flowchart of the trigger system.

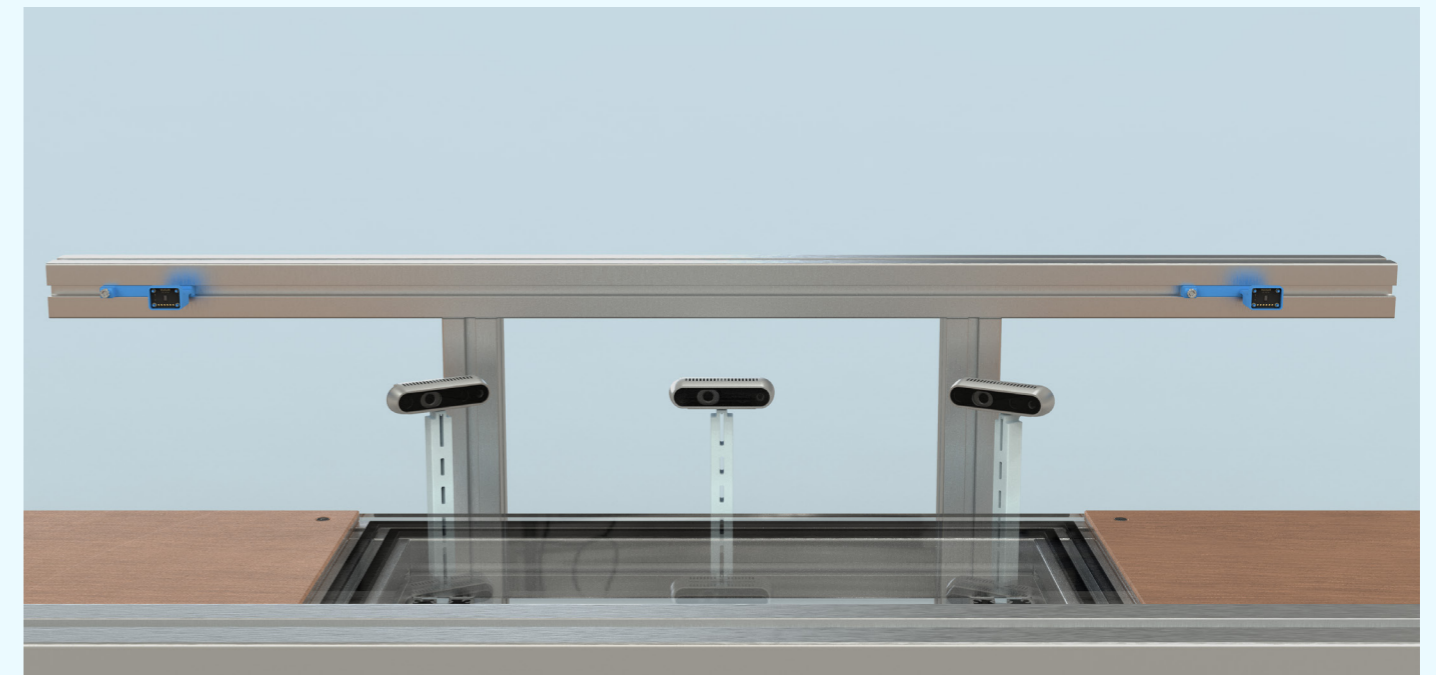


Figure 1.11 - Implementation of the trigger system (blue mounts) onto the existing 4D foot scanner frame.

The flowchart in figure 1.10 visualizes the flow of the trigger system. Currently, the trigger system starts when the scanner is turned on, since the trigger system is powered by USB. After initialization, the trigger system will be in a loop, constantly monitoring the sensor values.

The trigger system is designed to use Time of Flight (ToF) sensors as the triggers. The sensors are placed on the beams next to the scanning area and walkway of the scanner (figure 11.11). Since the sensors have a fixed position and measure a consistent constant distance, change in distance is easily detected when a patient walks past one of the triggers. This change is then communicated to the serial port by sending the sensor ids and values.

The schematic overview in figure 1.12 visualizes how the trigger system adds onto the existing 4D foot scanner system and lists all the components of the trigger system. The main system of the scanner handles serial data that is sent by the trigger system. Based on the content of the serial data, the scanner either starts or stops the data acquisition.

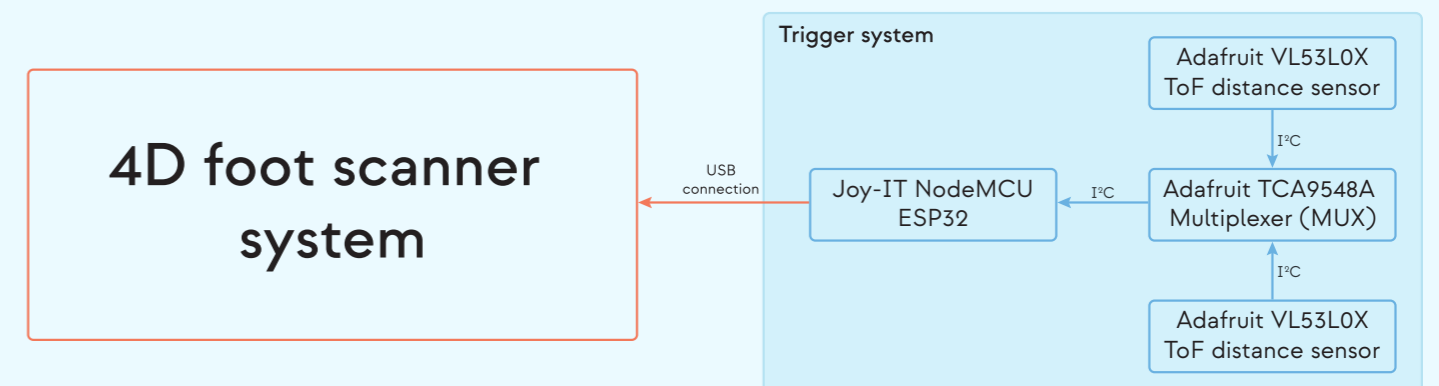


Figure 11.12 - A schematic component overview of the hardware components of the trigger system with connection types between the components.

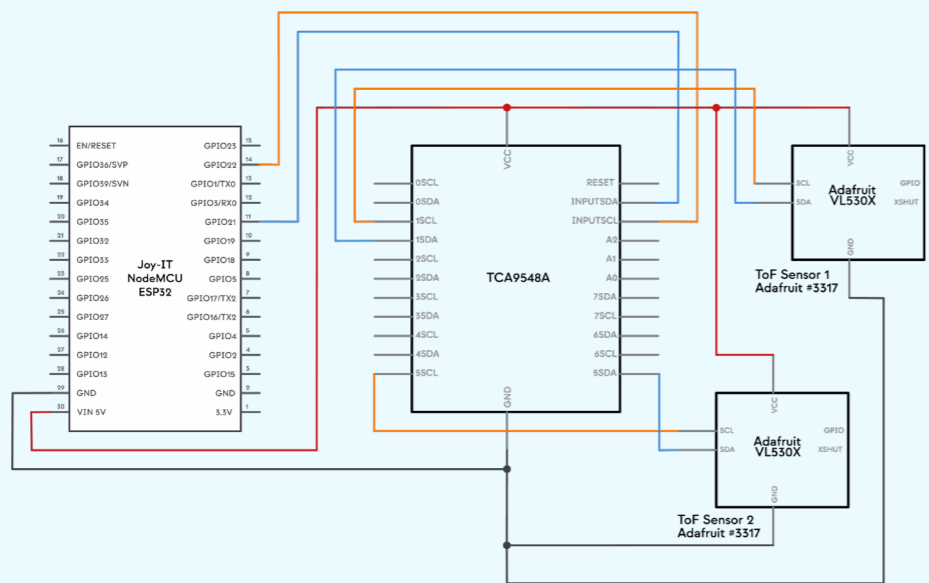


Figure 11.13 - Circuit design of the trigger system.

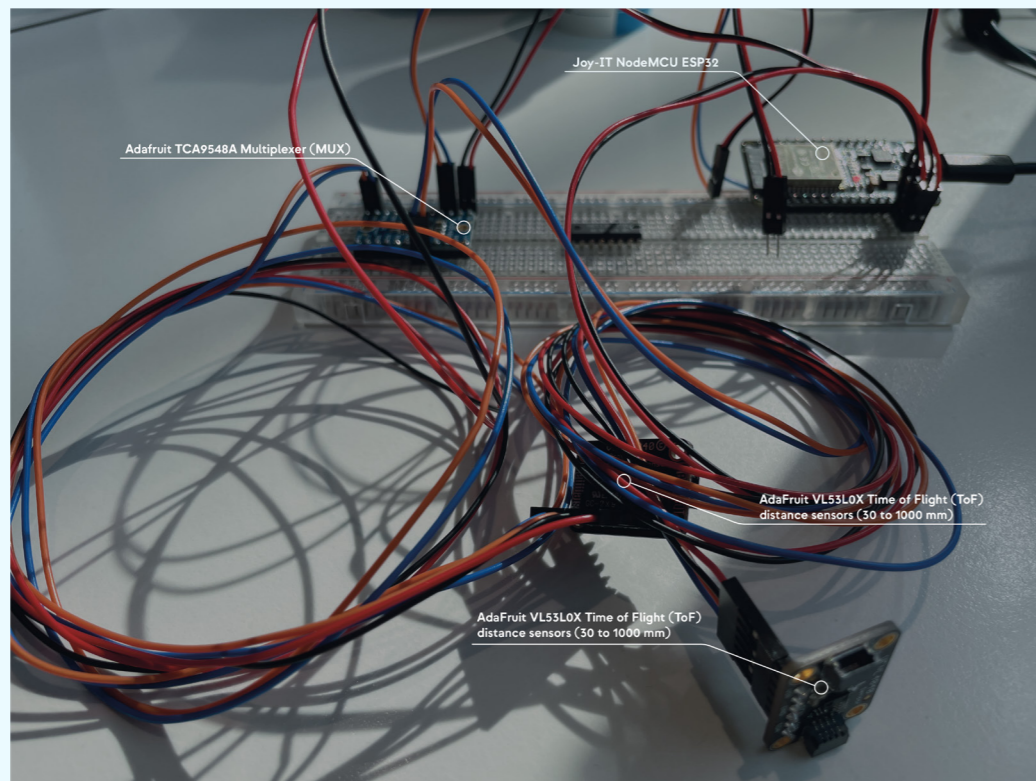


Figure 11.14 - Prototyping and testing of the circuit design. The components that make up the trigger system are labeled.

The trigger system is controlled by a Joy-IT NodeMCU ESP32 microcontroller unit (MCU). To this, two Adafruit VL53L0X ToF Distance sensors (30 to 1000 mm range) are connected through an Adafruit TCA9548a Multiplexer (MUX). All components are connected over I2C

connection. The trigger system is connected to the 4DFS system via the MCU through a serial connection (micro-USB). The circuit design of the trigger system is visualized in figure 11.13. Figure 11.14 shows the test setup of the trigger system on a breadboard.



Figure 11.15 - A render of how the ToF sensor is positioned in the mount on the aluminium frame.



Figure 11.16 - The real life implementation of the ToF sensor in the mount on the aluminium frame.

### 11.5.2 Positioning

As visualized in figure 11.15 and 11.16, the sensors are positioned in the vertical midpoint on one of the aluminium beams of the scanner frame and point to the beam on the other side of the scanner. The distance sensors are positioned 400 mm away from the middle of the glass plate (figure 11.17), leaving a remaining distance between the edge of the walkway and the sensor of 450

mm. This way, the patient can comfortably stand on the walkway without accidentally prematurely triggering the scanning system (figure 11.17).

Appendix E.5 contains in-depth information about the trigger system regarding the components selection, communication between the foot scanner system and the trigger system, the embodiment, a bill of materials and cost overview, and recommendations for optimization.

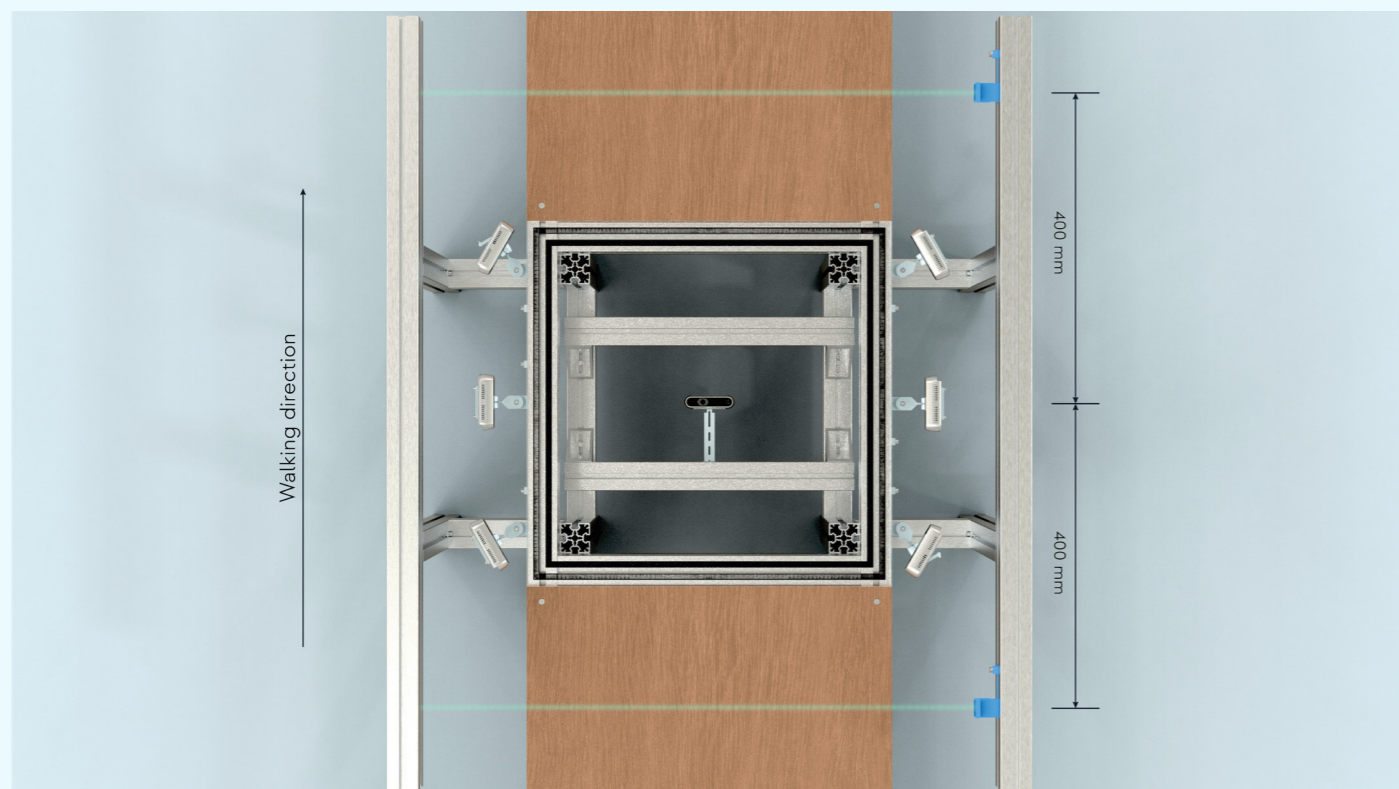


Figure 11.17 - Positioning of the sensors on the scanner. Both sensors are placed 400 mm from the glass plate. The green beam indicates the infrared light from the ToF sensors.

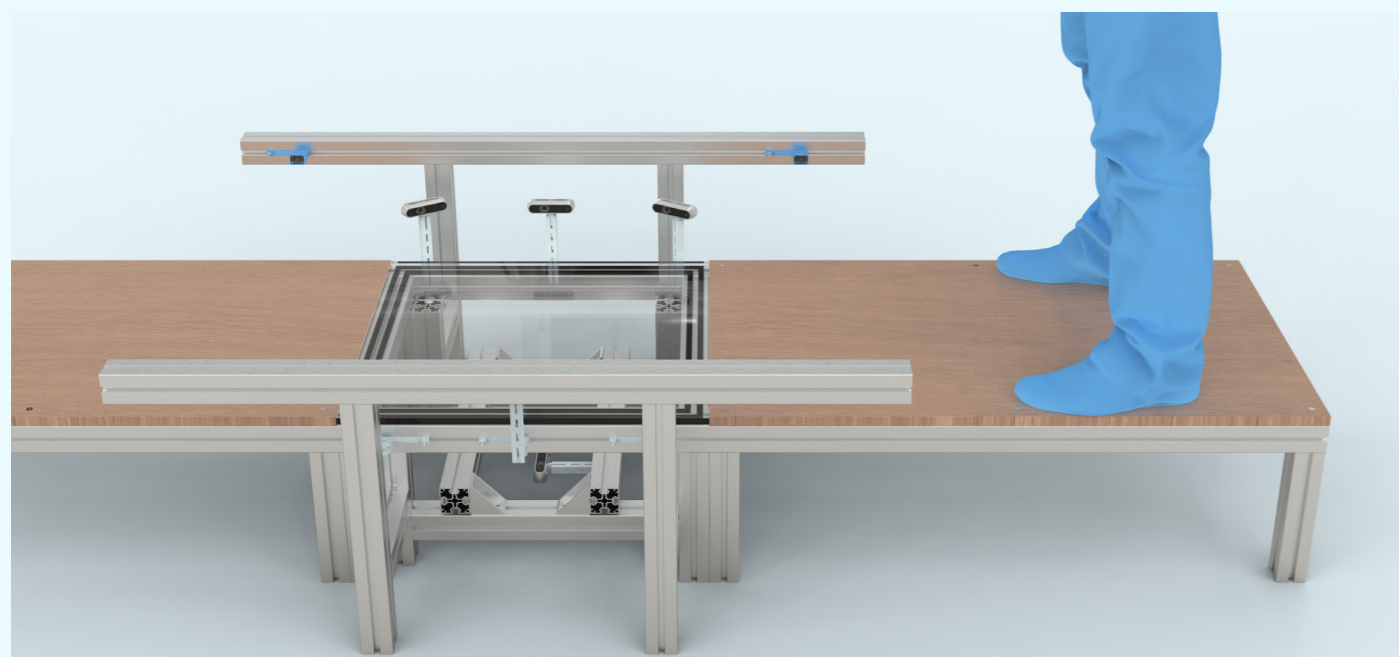


Figure 11.18 - A context render of a patient standing on the walkway of the scanner before triggering the first ToF sensor.

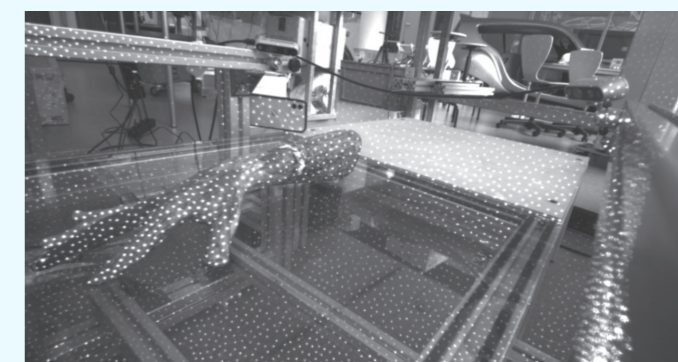
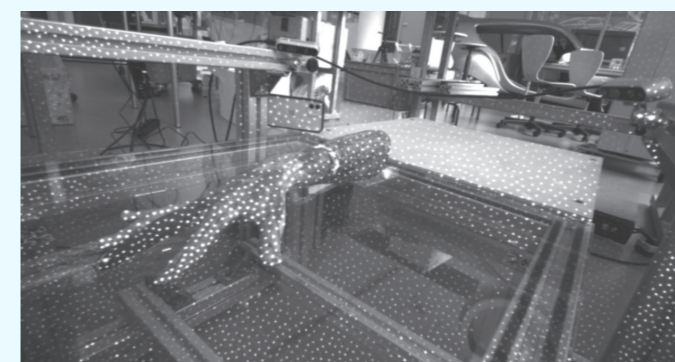


Figure 11.19 - Left and right depth sensor view, no added external light. The pseudo random pattern projected by the IR projector built into the RealSense cameras is quite distinguishable.

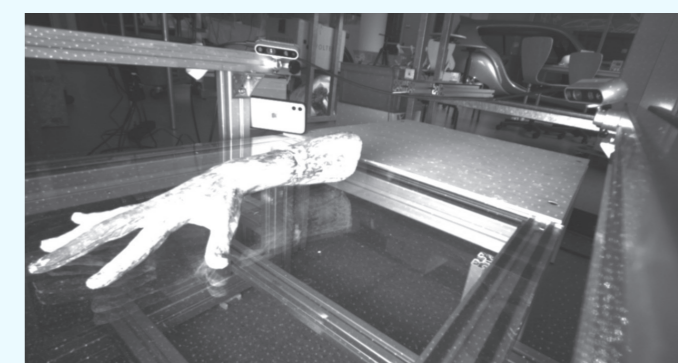
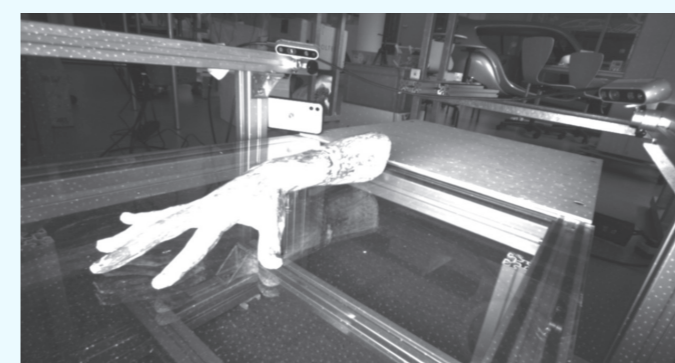


Figure 11.20 - Left and right depth sensor view, addition The external LED panel causes the initial IR pattern on the object to be less distinguishable. This results in gaps in the depth data.

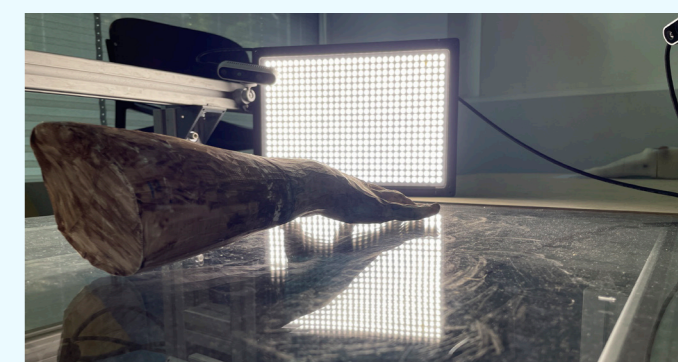


Figure 11.21 - Scene lighting comparison. (left) no additional lighting by the external light source. (right) 100 % brightness (5600 lux) additional lighting by the external light source.

## 11.6 External lighting

Options to include additional light sources to the embodiment of the scanner were considered to increase the quality of the 4D scans. To test the influence of additional lighting, an experiment was done with one D435i camera, a 3D printed hand model, and the acrylate

scanning plate. In this experiment, the brightness of the external light source was gradually increased and the effects on the depth scanning results were observed. Figures 11.19, 11.20 and 11.21 show the effect on adding external lighting. Appendix E.6 contains a detailed description of the scanning setup.

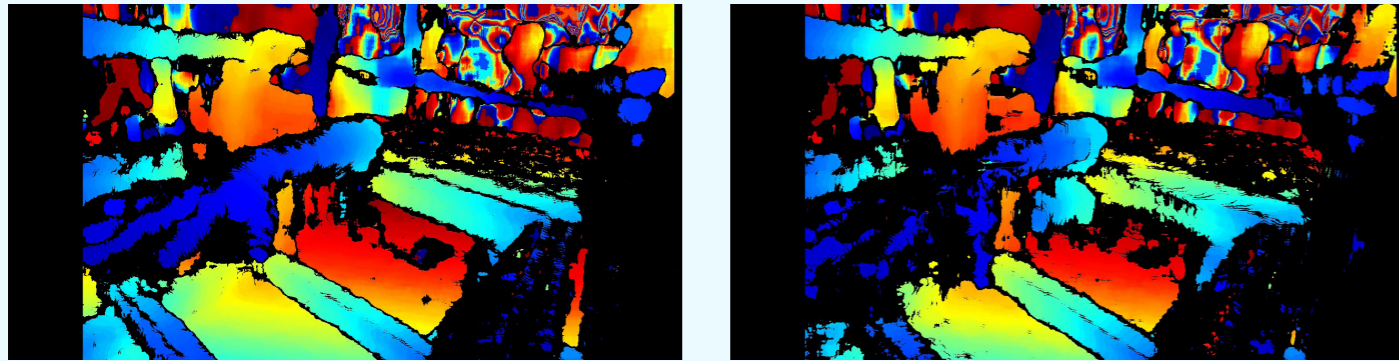


Figure 11.22 - Applying OpenCV's StereoBM to the aforementioned lighting conditions. (left) 0 lux external lighting, (right) 5600 lux external lighting. The depth data of the right image shows more gaps in depth data since the IR projection cannot be captured by the sensors.

The experiment gave four insights that were used in the design considerations of the final scanner:

1. **The camera needs a projected IR pattern to acquire depth data.**  
From the iterations with change in light intensity, it becomes clear that visibility of the IR speckle pattern is important in the final depth data quality of the D435i camera.
2. **To maintain complete depth data, the additional light source must not contain an IR component.**  
Since the LED panel contains an IR component, it lights up the whole hand with IR lighting with increased brightness, covering the hand with IR light. The cameras are not able to perceive the depth of this area, which results in loss of depth data.
3. **The IR component of the LED panel only affects short distance depth data acquisition.**  
The depth images made with the StereoBM implementation showed a change in depth perception on the hand model. However, the frame and surroundings of the scanner remained clearly visible, even with the added 5600 lux lighting.
4. **The acrylate plate does not reflect IR lighting.**  
The depth images made with the StereoBM implementation clearly show the bottom part of the scanner's frame.

Adding external lighting all around the volume of interest results in a controllable lighting environment and more

constant color images during the data acquisition process. However, external artificial lighting does not seem to directly improve the quality of the depth image. This is observed by using a stereo matching algorithm (OpenCV's stereoBM) on the two depth views for each lighting condition (figure 11.22). Nonetheless, it could be that the LED panel with its IR component obstructs the improvement in quality. Possibly, when a LED panel without IR component is used, the quality actually improves.

The experiment shows that the D435i camera needs the projected IR pattern in order to retrieve proper depth data. If this pattern is blocked or is faded because there is too much IR lighting in the environment, the depth sensors are not able to retrieve clear depth data, which results in gaps in the depth image.

The desirability to add external IR projectors to each camera is supported by Intel's whitepaper (Grunnet-Jepsen, Sweetser & Woodfill, 2020), stating that the depth perception of the cameras would benefit from an external pseudo random IR pattern projector next to each stereo camera in the system. With a higher IR pattern density, the depth sensors will probably be able to detect depth data more easily.

To gain knowledge about the IR reflective properties of the glass plate that is used in the final scanner and how this will affect the depth data, a similar experiment could be repeated.

Cost comparison table - Vidmar (2020), Concept 1, Concept 2 & Kwa (2021)				
Concept	Remarks	Product segment	Costs per segment (€) incl. VAT	Total concept costs (€) incl. VAT
Vidmar (2020)	Custom camera mounts not included.	Acquisition modules	€1,707.10	€3,738.63
		Desktop PC	€1,206.95	
		Embodiment components	€824.58	
Concept 1	Custom camera mounts and cloud computing not included.	Acquisition modules	€1,707.10	€3,787.82
		Desktop PC	€1,206.95	
		Embodiment components	€873.77	
Concept 2	Custom camera mounts not included.	Acquisition modules	€1,035.25	€3,151.92
		Desktop PC	€1,242.90	
		Embodiment components	€873.77	
Kwa (2021)	Custom camera mounts not included.	Acquisition modules	€1,692.39	€3,809.06
		Desktop PC	€1,242.90	
		Embodiment components	€873.77	

Table 11.3 - Cost comparison table of the mentioned 4D foot scanners from chapter 5, 9 and 10: Vidmar (2020), Concept 1, Concept 2, and the proposed scanner.

## 11.7 Pricing

The prototype that is presented in this chapter has a camera configuration of 9 cameras, of which 7 are D435i cameras, and 2 are D415 modules. An overview of all the components and costs is included in Appendix E.7.

Table 11.3 presents a cost comparison between the 4D foot scanner prototype of Vidmar (2020), the two concepts as proposed in chapter 10, and the final 4D foot scanner as presented in this chapter. As mentioned in chapter 10, the camera configuration of the scanner of Vidmar (2020), and concepts 1 and 2 are set to 5 connected cameras, since this follows requirement C.4.

The total component costs for the final 4D foot scanner prototype amount to €3.809,06, which is nine times lower than the requirement of not exceeding the commercial price of €35.000 [requirement PS.1. Note that additional costs which are normally included in commercial prices are not included in the cost comparison. Costs that are part of these additional costs are for example: profit margin, R&D costs, manufacturing costs, transportation costs, CE certification costs, overhead expenses, marketing, insurance and storage. However, a buffer of €31.190,94 per scanner still remains to include these costs.

With an increase of 4 cameras compared to the other three concepts, the price of the final foot scanner is only marginally higher. This is mainly because there is

no need for expensive acquisition modules, which each include an Intel Realsense camera, a Raspberry Pi 4 and 32 GB micro SD card, a 250 GB NVME M.2 SSD and an appropriate NVME M.2 SSD casing. Also, the cost analysis does not include the cables that are needed to connect the components in these modules to each other. The generic cables used to connect the camera modules to the scanner system (USB 3.1 cables) are included in the analysis.

## 12. Data acquisition

12.1	Data acquisition pipeline	P. 94
12.2	Acquisition performance analyses	P. 97
12.2.1	Frame analysis	P. 97
12.2.2	Memory analysis	P. 98
12.2.3	Dynamic acquisition	P. 100
12.3	Conclusions	P. 101
12.3.1	Frame analysis	P. 101
12.3.2	Memory analysis	P. 101

Chapter 7 describes two design challenges that are relevant to the data acquisition section of the 4D foot scanner: synchronized 4D data acquisition and the scanning pipeline. These challenges are overcome in the development of the final scanner to the point that 4D data acquisition with nine cameras is stable. The implementation takes the requirements regarding data acquisition in chapter 9 into account.

Chapter 12.1 presents a proposal for a new data acquisition pipeline. Chapter 12.2 analyses the proposed data acquisition pipeline in three different ways: frame acquisition, dynamic acquisition time, and memory consumption. An evaluation of the analyses is included in chapter 12.3. Appendix F elaborates on the data acquisition analyses in more detail.

### Conventional frame acquisition from RealSense camera

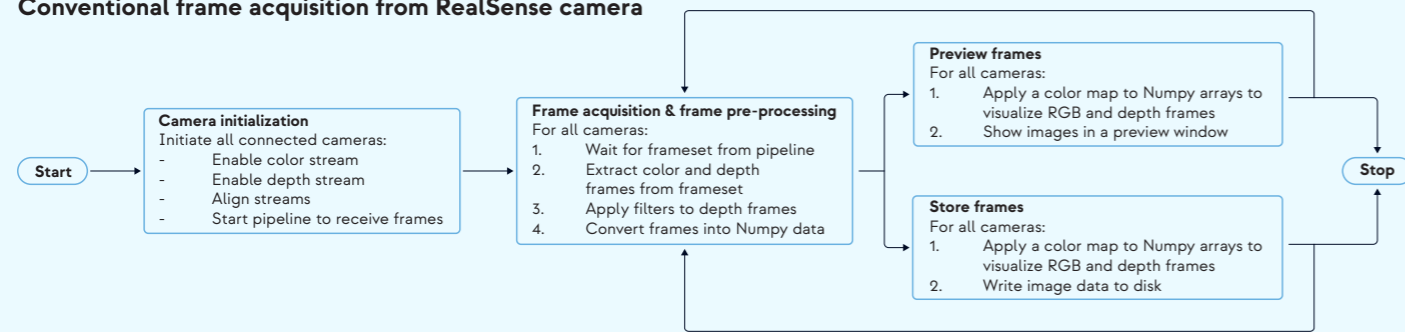


Figure 12.1 - A flowchart of the acquisition phase during conventional Intel RealSense use.

### Data acquisition pipeline for multiple RealSense cameras

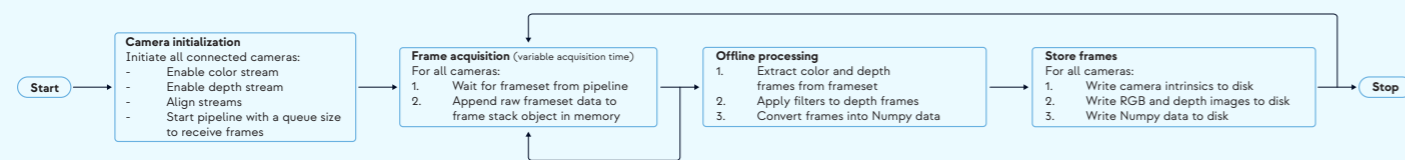


Figure 12.2 - A flowchart of the proposed data acquisition pipeline for the scanner.

## 12.1 Data acquisition pipeline

In contrast to 3D scanning, the ability to synchronize multiple cameras is an essential requirement in 4D scanning in order to properly align the RGB and depth data from all camera views. Keeping the project goal in mind to end up with a proof of concept for 4D foot scanning using commodity hardware, the decision was made to discard the implementation of Intel's RealSense hardware (HW) synchronization or their "Genlock" function (Grunnet-Jepsen et al., 2021). This would increase the hardware complexity of the system. Instead, a sequential data acquisition approach was implemented, which does not require any additional hardware. It also is the road of least resistance when exploring the possibilities of connecting as many Intel RealSense cameras to a computer as has been done in this project.

The acquisition pipeline is designed in such a way that it tries to minimize runtime in the context of sequential computing in multiple ways:

- Switching from online to offline processing;
- Making use of temporary memory storage;
- Making use of the internal memory storage of the RealSense cameras; the frames are queued in the internal memory of the cameras and dequeued when resources are available within the acquisition pipeline;

- Delay data acquisition after every twenty camera chain iterations to minimize the amount of frame drops (Intel, 2019).

Generally, acquiring frames from RealSense cameras is done as described in figure 12.1: the camera pipeline is watched for incoming framesets, the frameset is then pre-processed, and the frames are ready to be viewed. This approach can almost preview frames in real time for a single connected camera.

However, the scanner setup consists of 9 connected cameras which can result in connectivity problems due to the restricted bandwidth of the scanner, as pointed out in chapter 5.3. By pre-processing the frames directly after acquiring the frames for each camera, the acquisition slows down even more.

This newly proposed data acquisition pipeline reconsiders the conventional method of acquiring frame data from RealSense cameras. The goal is to be able to acquire data as fast as possible, in order to capture a whole gait cycle of a patient with the highest frame rate possible, bound by the hardware that is used. Therefore, for every camera, every frameset is temporarily stored in memory after it is acquired. Also, the intrinsic parameters of all cameras are stored in memory after acquisition, since this data is needed in post-processing to construct point clouds from the depth data.

### Desired sequential frame acquisition across cameras Consistent frame acquisition speeds

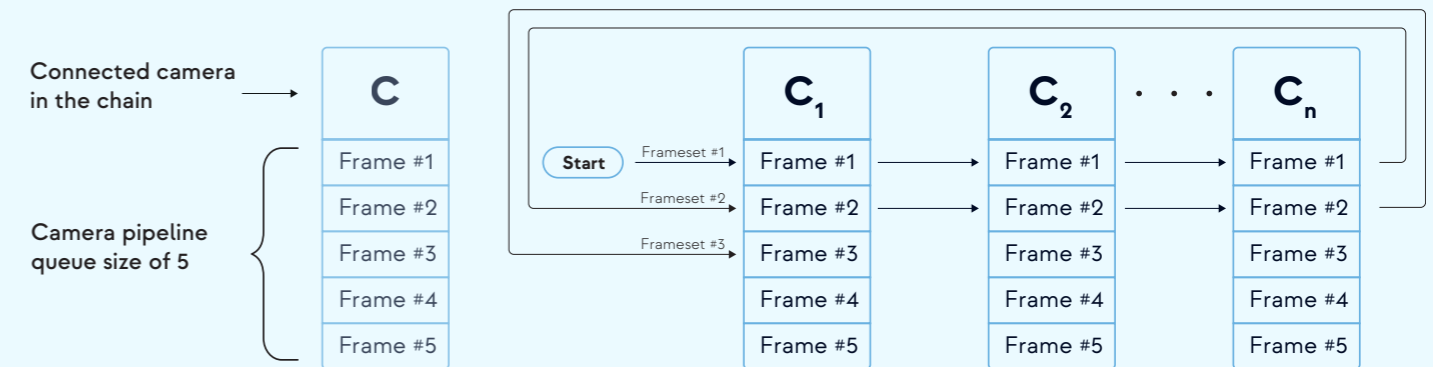


Figure 12.3 - A schematic overview of the desired flow when acquiring frames sequentially across cameras. For every loop, the frame numbers per camera are the same.

### Undesired sequential frame acquisition across cameras Due to inconsistent frame acquisition speeds

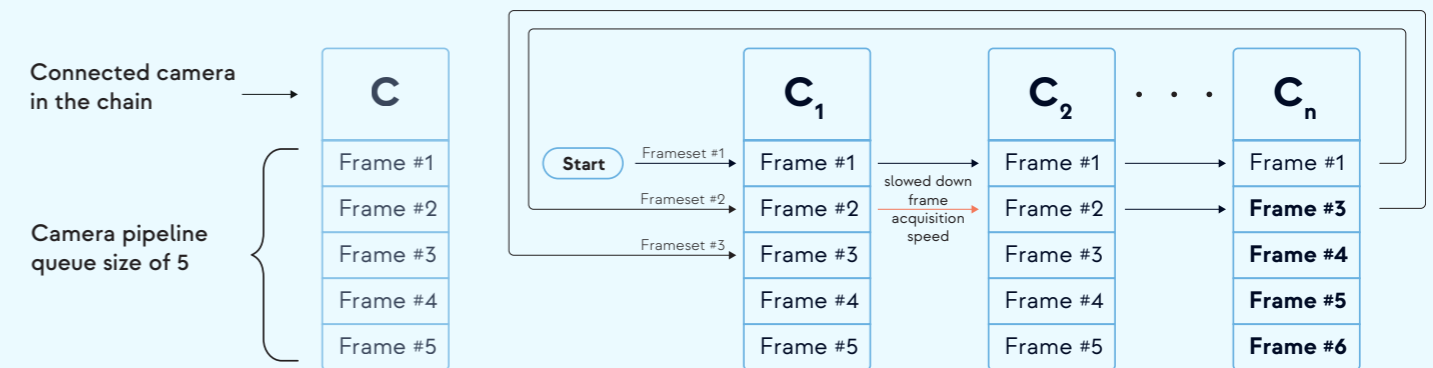


Figure 12.4 - A schematic overview of the undesired flow when acquiring frames sequentially across cameras. Due to inconsistent frame acquisition speeds, the frame number at the end of the camera chain prematurely moves to the next frame. When a new frame is available to be enqueued in the pipeline queue and the pipeline is full, the Intel RealSense camera automatically dequeues the first available frame at the front of the queue (first in, first out principle).

A schematic overview of the proposed and implemented data acquisition pipeline is presented in figure 12.2. The pipeline consists of four phases: initialization, acquisition, offline processing and storing data.

The implementation of the 4D data acquisition follows a sequential approach. Meaning that, for every frame loop, frames that are queued in the internal memory of the cameras are only dequeued when the frame of the previous camera in the chain is dequeued. Figure 12.3 visualizes the process of how sequential data acquisition ideally works. It is desired to acquire frames from each camera as fast as possible, before the last camera in the chain already has a new frame in the queue.

Figure 12.4 visualizes the process when the dequeuing of the camera frames is slowed down: the frame from the camera at the beginning of the chain does not match with the frame from the camera at the end of the chain. This results in a mismatch of frames when the frames are bundled by frameset number during the offline processing phase. This could result in a frameset where the foot position in one frame does not correspond with the foot position in another frame in the frameset. As shown in figure 12.4, frameset #2 should contain only frames with frame #2. However, due to the slowed down frame acquisition speed, frame #2 of the last camera in the chain has been prematurely dequeued and now frame #3 will be included in frameset #2.



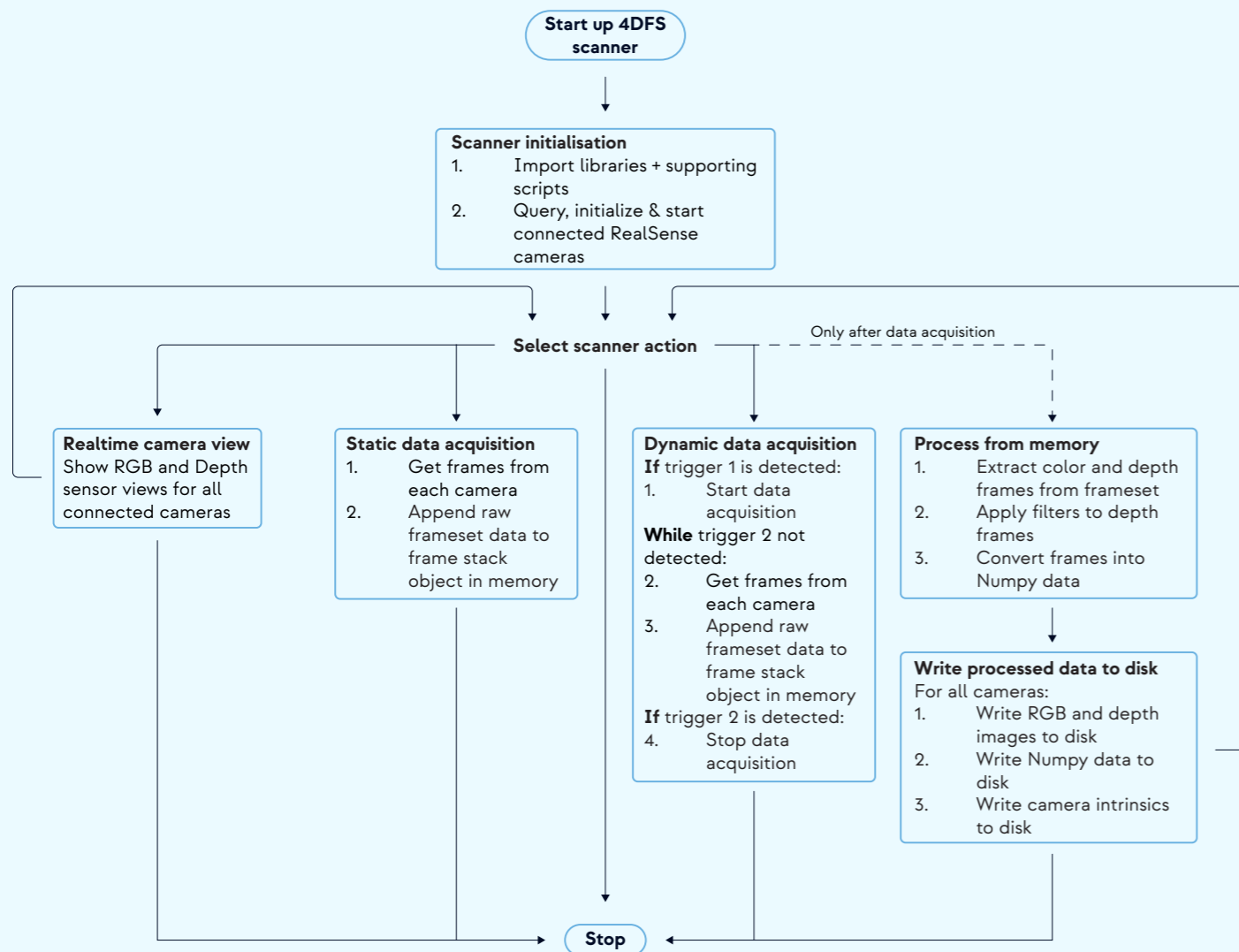


Figure 12.5 - The flowchart of the implemented data acquisition phase.

The minimum speed at which the frames should be dequeued per camera depends on the frame rate of the cameras in the chain, and on the amount of cameras. As described in requirements DA7 and DA8 in chapter 9, for a camera configuration of 6 cameras, the system must be able to acquire a frame within 5.5 ms. Chapter 12.2.1 presents the analysis on the frame speed and consistency of the scanner.

Figure 12.5 visualizes the flowchart of the total acquisition pipeline of the scanner, which also includes the implementation of the proposed data acquisition pipeline of figure 12.2.

During the initialization phase, the cameras connected to the system are queried and initiated with the configuration as mentioned in chapter 11.2. The initialization phase is necessary to prepare the cameras

for data acquisition. The scanning setup for nine cameras seems to stabilize when calling a hardware reset for each camera prior to starting the initialization process.

After acquisition, the offline processing phase reads the acquired framesets from memory. In this phase, the framesets are split up into RGB and depth frame data. RealSense filters, such as a spatial filter, temporal filter, and holes filling filter, are applied to the depth data to improve the quality of the depth data.

At the end of the acquisition pipeline, all relevant data for post-processing is stored. It includes raw RGB and prepared depth data, RGB and depth images, and the intrinsic camera parameters for all cameras in the system.

Performing this data acquisition process requires

Frame speed data per session										
	Session 1	Session 2	Session 3	Session 4	Session 5	Session 6	Session 7	Session 8	Session 9	Session 10
Number of cameras	6	6	6	6	6	6	6	6	6	9
Acquisition duration (s)	1	2	4	5	5	10	10	5	10	5
Amount of frames	120	240	480	600	600	1200	1194	600	1200	900
Average time per frame per camera (s)	0.00007035	0.00006509	0.00012053	0.00006033	0.00006024	0.00005860	0.00006404	0.00008259	0.00007476	0.00020355
Minimum duration (s)	0.00003886	0.00003791	0.00003695	0.00003672	0.00003576	0.00003552	0.00003433	0.00003672	0.00003505	0.00003600
Median duration (s)	0.00005364	0.00005913	0.00005412	0.00005388	0.00005722	0.00005364	0.00005651	0.00006008	0.00005722	0.00005805
Maximum duration (s)	0.00038600	0.00028515	0.01262903	0.00031877	0.00045180	0.00200605	0.00247717	0.00422597	0.00582242	0.06171536
Average loop time (s)	0.00042207	0.00039051	0.00072320	0.00036199	0.00036142	0.00035159	0.00038422	0.00049556	0.00044856	0.00183192
# of frame rate cap occurrences	0	0	2	0	0	0	0	0	1	4

Frame analysis over the entire dataset		
Total # of frames	7134	
# of occurrences > frame rate cap	7	
Percentage of frames too late	0.0981%	
Overall average time per frame per camera	0.0000860 (s)	0.086 (ms)
Overall minimum time per frame per camera	0.0000343 (s)	0.034 (ms)
Overall median time per frame per camera	0.0000536 (s)	0.054 (ms)
Overall maximum time per frame per camera	0.0617154 (s)	61.715 (ms)
Average time per frame per loop	0.0005771 (s)	0.577 (ms)

Table 12.1 - (top) An overview of the frame analysis over the frame speed of ten data acquisition runs. (bottom) A general overview of the overall frame analysis.

sufficient hardware capabilities of the scanner. A concern is the RAM capacity of the scanner, which should be able to hold all frame data of all connected cameras during one acquisition run. The memory analysis in chapter 12.2.2 elaborates on this concern.

## 12.2 Acquisition performance analyses

The acquisition analysis gives insight into the performance of the 4D foot scanner, regarding acquisition speed, dynamic acquisition time and memory usage. Additional scripts have been written in Python to evaluate the speed and memory usage, using native Python modules (sys and time).

### 12.2.1 Frame analysis

To match the acquisition requirements mentioned in chapter 9, the maximum tolerable acquisition speed of the whole system cannot exceed 33 ms. Since the system includes six cameras, the maximum delay between frame acquisition for each camera may not exceed 5.5 ms. Runtime evaluation of the acquisition phase showed promising results that match the set requirements. Table 12.1 presents the outcomes of the frame speed evaluation, which was done on ten individual data acquisition processes with varying acquisition lengths, acquiring a total of 7134 frames.

The last recorded session (session 10) was done using 9 connected cameras to observe the difference in behaviour compared to the camera configuration with 6 cameras.

To evaluate the performance, the acquisition time to fetch each frameset is recorded. In general, the acquisition performance of the scanner sits well below the threshold which is described in the list of requirements, as the average acquisition time per frame per camera is 0.086 ms. Also, the acquisition rate for the whole camera chain per frame number is 57 times faster than the limit of 33 ms, since it takes 0.577 ms on average to acquire one frame from all six cameras.

Session 10, as the only session with a camera configuration of 9 cameras, has noticeable inconsistencies compared to the other sessions. Keep in mind that the frame rate cap of this session is 3.67 ms, opposed to the 5.5 ms for the 6 camera configuration. Observing the frame speed data of session 10, the minimum and median frame speed are consistent with the other sessions. However, the average frame speed (0.20 ms) and maximum registered frame speed (61.7 ms) is much higher than that of the other sessions. The longer average frame speed is likely influenced by the maximum registered frame speed, which is between 10 and 200 times longer than that of the other sessions.

The data shows that, out of 7134 frames, only 9 frames took longer to acquire than the relative frame rate threshold per session. Also, session 10 contains more

Memory analysis overview per camera configuration									
# of cameras	Total # of unique acquisition runs	Average acquisition time (s)	Median acquisition time (s)	Maximum acquisition time (s)	# of frames per camera	Average # of frames per acquisition per camera	Average frame stack size (bytes)	Median frame stack size (bytes)	Maximum frame stack size (bytes)
1	13	1.000	1.000	1.000	906	70	4649	4584	5440
2	31	1.000	1.000	1.000	2030	65	8686	8408	10680
5	1	0.100	0.100	0.100	14	14	4960	4960	4960
6	23	1.348	1.000	6.979	1557	68	26750	28104	33240
7	60	1.474	0.100	7.378	1154	19	9146	6896	29632
8	2	0.100	0.100	0.100	103	52	27352	27352	27576
9	13	0.585	1.000	1.000	625	48	28685	30568	40144

Memory analysis overview over the entire dataset						
Total # of unique cameras	Total # of unique acquisition runs	Total # of acquired frames	Overall average acquisition time (s)	Overall average frame stack size (bytes)	Overall median frame stack size (bytes)	Overall maximum frame stack size (bytes)
8	143	28905.000	1.208	13534.378	9752	40144

Table 12.2 - (top) An overview of the memory analysis per camera configuration. (bottom) A general overview of the overall memory analysis.

frames that exceed the frame rate threshold, compared to the other sessions.

### 12.2.2 Memory analysis

The proposed data acquisition pipeline from chapter 12.1 prioritizes the data acquisition of raw frame data over processed frame data, to speed up the acquisition performance of the foot scanner. Doing this requires to temporarily store the acquired frame data of all cameras during an acquisition run in the internal memory (RAM) of the scanner.

To verify the possibility of executing this new approach with the presented system configuration from chapter 11, a preliminary memory analysis is done. In addition, the memory analysis gives an indication on the consistency of the scanner in terms of performance; whether or not it is able to output a consistent and predictable number of frames and memory usage. Worth noting is that the analysis only includes the memory consumption during frame acquisition. Overhead memory usage, due to the amount of connected cameras and executing the Python script, is not included in this analysis. Therefore, any conclusions from this analysis are only applicable to the memory usage during frame acquisition. Appendix F.1 further elaborates on the memory analysis.

The memory analysis tracks several parameters during an acquisition run:

- The size of a received frameset (in bytes);

- The size of the frame stack (in bytes) that contains all acquired framesets from all cameras;
- The acquisition time (in seconds);
- The number of frames per camera;
- The number of cameras connected to the system during the acquisition run;
- The frame rate for both the RGB and depth sensors of the cameras (in fps);
- The sensor resolution of both the RGB and depth sensors.

For all data acquisitions, the sensor resolution is set to 848 x 480 pixels, and the frame rate is set to 30 fps. The parameters that vary throughout the memory analysis and influence the required memory capacity of the scanner are: the acquisition time, and the camera configuration (number of connected cameras). The memory usage is analyzed by adjusting these variable parameters, with respect to the frame stack size.

The analysis is done with a number of camera configurations for different acquisition times, as shown in table 12.2. The dataset mostly consists of static data acquisition scans, due to time constraints. It's worth noting that the configuration with 7 cameras has the largest variation in acquisition time, which can be observed by studying the median and maximum acquisition times for all camera configurations.

7 Intel RealSense cameras: Frame stack size (bytes) vs. Acquisition time (s)

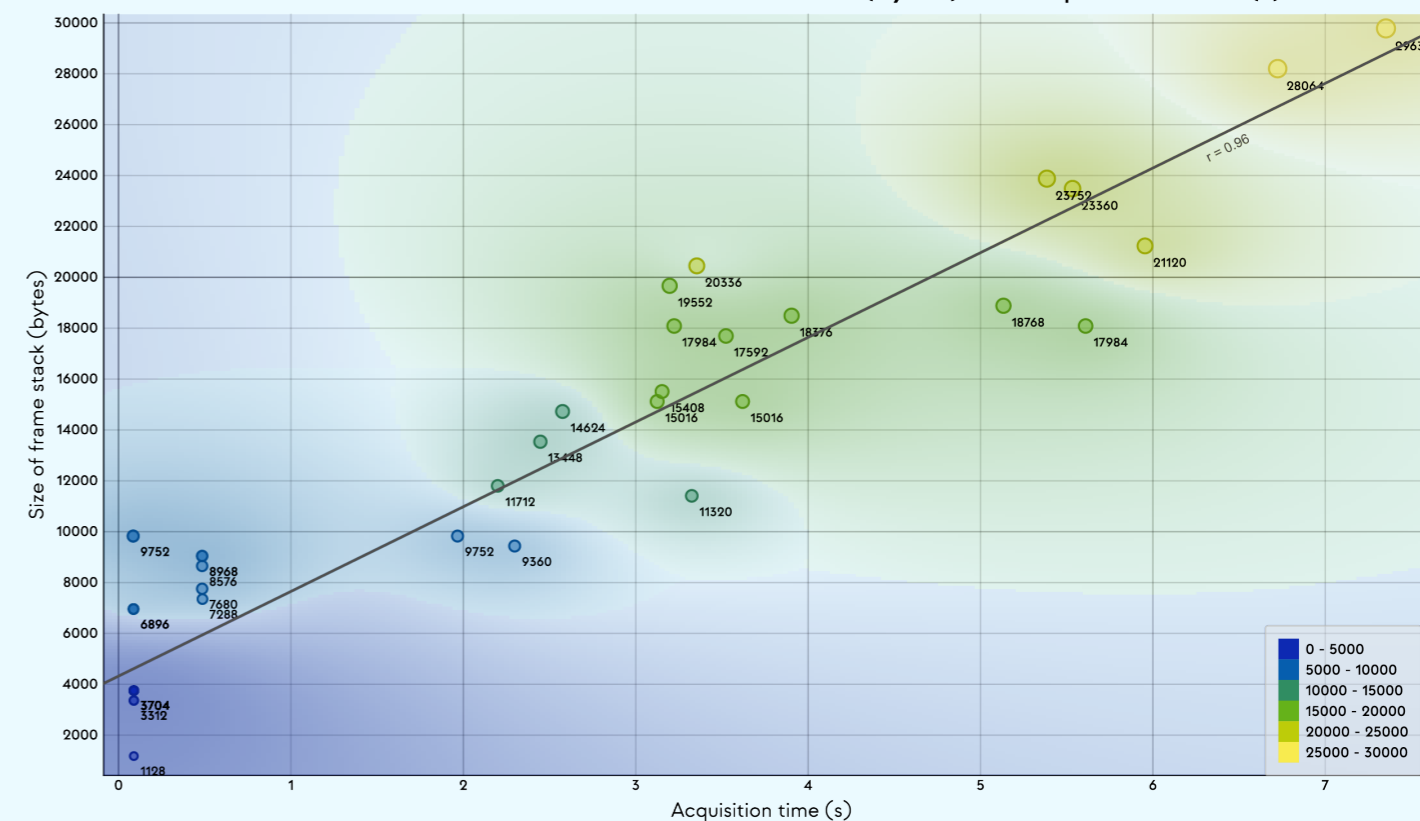


Figure 12.6 - A scatterplot of the frame stack size (in bytes) with respect to the acquisition time (in seconds) for only 7 cameras. The colour and labels of the data points represent the amount of connected cameras. The best-fitting line with a slope of  $r = 0.96$  is drawn.

During memory analysis, the size of the Python object (the frame stack) is evaluated at the end of each data acquisition run. Since at the end of the run, the frame stack contains all acquired framesets from all cameras. The object size of the framestack is the amount of memory that is used to temporarily store all frameset data of one acquisition run.

Observing the data from table 12.2, it shows that the frame stack size is maximized at 40144 bytes, which is 40.1 MB. This is for a camera configuration of 9 cameras, with an acquisition time of 1 second and 68 frames per camera.

When plotting the frame stack size against the acquisition time for a camera configuration of 7 (figure 12.6), a linear trend presents itself with a regression line with a Pearson correlation coefficient of  $r = 0.96$ . It shows that, for this camera configuration, it is possible to estimate the memory requirement of the acquisition process with a relatively high likelihood.

Because of the lack of variation in acquisition times of the

other camera configurations, it is not yet possible to spot any (linear) trends.

A surprising outcome of the data shows that the amount of cameras connected to the system do affect the amount of frames that is outputted during the data acquisition process. This is visible when plotting the number of frames against the acquisition time (figure 12.7). The data points at  $t = 1$  s for different camera configurations show a fluctuation in the number of outputted frames. Also, the acquired number of frames for the same camera configuration is fairly inconsistent: camera configuration 6 outputs anywhere between 40 and 90 frames for an acquisition time of 1 second.

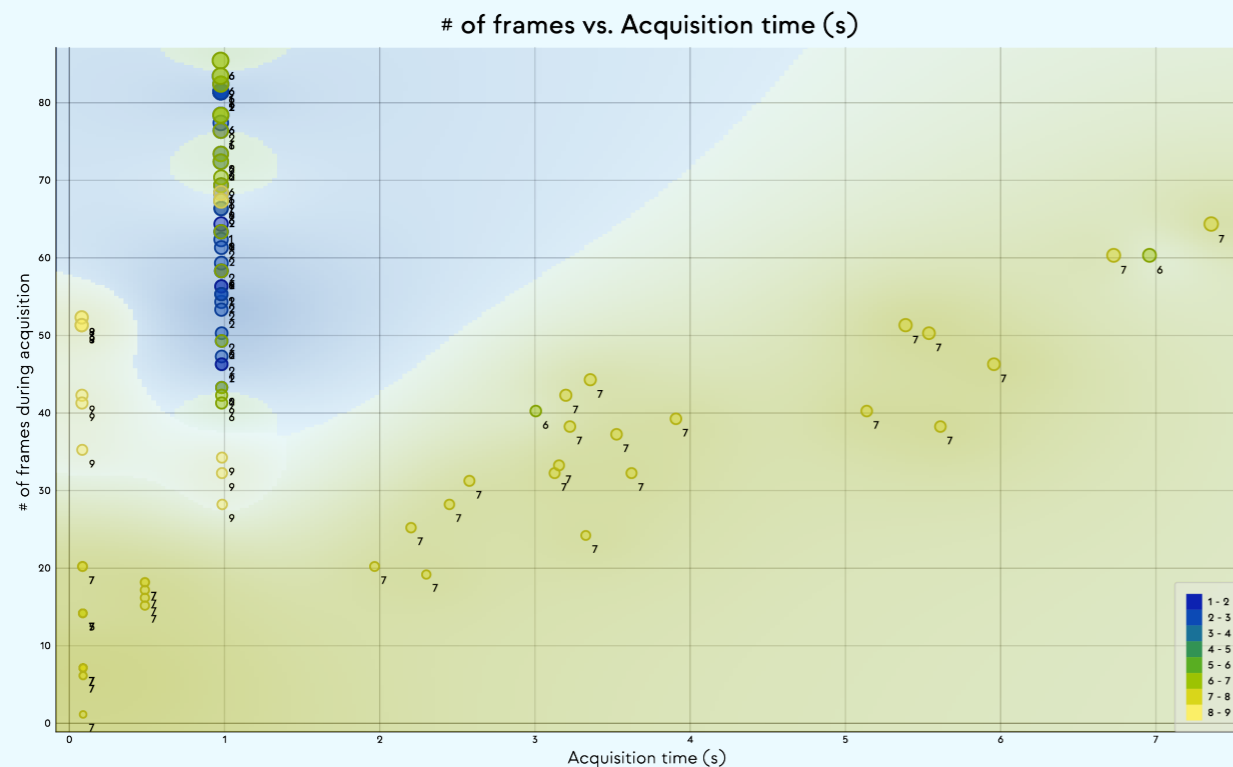


Figure 12.7 - A scatterplot of the number of frames with respect to the acquisition time (in seconds). The colour and labels of the data points represent the amount of connected cameras.

Memory analysis overview of dynamic scanning data per camera configuration										
# of cameras	Total # of unique acquisition runs	Average acquisition time (s)	Median acquisition time (s)	Maximum acquisition time (s)	# of frames per camera	Average # of frames per acquisition per camera	Average frame stack size (bytes)	Median frame stack size (bytes)	Maximum frame stack size (bytes)	Maximum frame stack size per second (bytes/s)
6	2	5.000	5.000	6.979	100	50	20088	20088	24072	3449
7	21	4.001	3.375	7.378	793	38	17723	17984	29632	4016

Memory analysis overview over the dynamic scanning dataset							
Total # of unique cameras	Total # of unique acquisition runs	Total # of acquired frames	Average # of frames per acquisition	Overall average acquisition time (s)	Overall median acquisition time (s)	Overall maximum acquisition time (s)	Overall average frame stack size (bytes)
2	23	6151	39	4.088	3.458	7.378	17928

Table 12.3 - (top) An overview of the memory analysis over the dynamic scanning dataset per camera configuration. (bottom) A general overview of the memory analysis over the entire dynamic scanning dataset.

### 12.2.3 Dynamic acquisition time

The average acquisition time for dynamic scans can be analyzed using the data of the memory analysis from chapter 12.2.2. It should be pointed out that the walking speed of these acquisitions is not regulated and only performed by a single person. Inconsistent walking speeds across different patients is expected in a podiatry context. A better representation of the average dynamic scan time would be possible if the dataset and the amount of unique participants is larger. The full dynamic

scan dataset is included in table F.1 of Appendix F.2.

A summarizing overview of the obtained data per camera and overall is presented in table 12.3. From the 23 acquisition runs, the average acquisition time is 4.08 seconds per dynamic scan, with an average of 39 frames per acquisition. Comparing the two camera configurations, it seems that the average frame stack size increases as the number of cameras in the configuration increases.

## 12.3 Conclusions

The preliminary quantitative analyses that were performed on the system and presented in chapter 12.2 are useful in determining the performance of the proposed data acquisition pipeline. However, more elaborate evaluations should be done on the performance to be able to verify the performance of the proposed data acquisition pipeline for a varying array of camera configurations and use cases.

### 12.3.1 Frame analysis

The frame analysis is constricted to only ten recorded sessions. The performance across the 6 camera configuration sessions is consistent, which is desirable. It gives an indication that the system can perform consistently and that general performance is predictable. However, to truly state this, an extensive analysis must be done over time on a wider range of camera configurations, each with a larger dataset.

Remarkable was that session 10 had more frame rate threshold occurrences than the other sessions. This could be due to the fact that the system has trouble with acquiring a larger amount of frames, which could choke the bandwidth of the system. A more elaborate analysis should be able to validate this hypothesis.

For data processing purposes, an implemented check to detect outliers that exceed the upper bound of acquisition time could help flag and communicate inadequate and unreliable scans to the operator of the scanner.

### 12.3.2 Memory Analysis

The memory analysis verifies that the presented system configuration from chapter 11 is capable of running the proposed data acquisition pipeline from chapter 12.1 The

insights from figure 12.6 indicate that it might be possible for a camera configuration of 7 cameras to predetermine the memory consumption of the scanner with high likelihood ( $r = 0.96$ ). However, it has yet to be determined if the linear trend shown in figure 9.6 applies to all camera configurations.

Furthermore, the analysis has given preliminary insights in the amount of frames that are acquired within the same acquisition time for different camera configurations. The fact that a configuration of 6 cameras is able to acquire more frames than a configuration of 2 cameras is surprising. Especially since the configuration of 9 cameras returns the least amount of frames. It would be expected that a larger number of connected cameras will per definition return less frames because more connected cameras can cause bandwidth issues. This is similar to the drop in the acquisition speed of the frames.

The maximum amount of memory that is temporarily stored is 40.4 MB for a 9 camera configuration with an acquisition time of 1 second. As previously mentioned, the general duration of a dynamic foot scan takes about 4.08 seconds. However, the maximum duration was 7.34 seconds.

If the assumption is made that the 9 camera configuration has the same linear trend ( $r = 0.96$ ) properties as the 7 camera configuration, an estimation of the required amount of memory can be made with equation 12.1.

Taking the maximum acquisition time as upper bound (7.34 seconds), the amount of bytes that are temporarily stored into memory would amount to 284.675 MB. With the 4GB RAM setup as presented in chapter 11], the proposed scanner configuration should have enough memory to handle the proposed data acquisition pipeline.

$$Estimated\ memory = (t_{acquisition} \cdot r) \cdot Memory\ consumption_{t=1} \quad (Eq. 12.1)$$

## 13. Data processing

13.1	Data processing pipeline	P. 104
13.1.1	From raw data to point cloud	P. 104
13.1.2	Preprocessing data	P. 104
13.1.3	Rough alignment	P. 105
13.1.4	Fine point cloud registration	P. 106
13.2	Result	P. 107
13.2.1	Rigid ICP	P. 107
13.2.2	Nonrigid ICP	P. 108
13.2.3	Preliminary accuracy validation	P. 109
13.3	Conclusions	P. 110

As mentioned in chapter 6, the primary focus of this thesis is on the development and validation of 4D data acquisition. However, to validate the quality of the data that is acquired during the acquisition process, the data has to be processed.

A short study has been done on the data processing pipeline related to the 4D foot scanner in chapter 13.1, which considers a selection of post-processing and data registration methods that are relevant in the construction of 3D models. Additionally, chapter 13.2 proposes an improved extrinsic camera calibration process over Vidmar's open-loop pairwise calibration method, as presented in chapter 5.4. To conclude, the accuracy of the scan is evaluated in section 13.3.

## 13.1 Data processing pipeline

The Intel® RealSense™ SDK 2.0 (Intel RealSense, 2021) promotes the use of the open-source 3D data processing library Open3D (Zhou, Park & Koltun, 2018). Therefore, this library is used in the data processing pipeline. This library contains ready-to-use implementations of widely used algorithms which are needed in performing 3D data processing and manipulation.

Figure 13.1 presents a schematic overview of a general pipeline that is used in the processing and manipulation of 3D data. This is also usable for the 4D foot scanner. The pipeline depends on the use of multiple Python libraries: NumPy (Harris, Millman, van der Walt et al., 2020), Open3D (Zhou, Park & Koltun, 2018), and OpenCV (Bradski, 2000).

### 13.1.1 From raw data to point cloud

Scanning data which is the output from the data acquisition needs to be transformed into point clouds. During data acquisition, the pipeline stores not only RGB and depth frames of each acquired camera frame, but also a numerical representation of the depth data (using Numpy) and the intrinsic parameters for each camera. Point clouds can be generated from the numerical data and the intrinsic parameters. The intrinsic parameters are needed to properly position the depth data into a 3D space. Without the proper intrinsic parameters, the depth data cannot be correctly represented by a point cloud.

Point cloud manipulation software, such as the open-source software Meshlab (Cignoni et al., 2008), is a popular tool when working with 3D data processing and manipulation, since it can perform all steps in the data processing pipeline.

### 13.1.2 Preprocessing data

Preprocessing the raw point cloud data is an important step, which discards any unwanted depth data from the point cloud. The goal is to remove distracting features in the point cloud that can hinder the fine registration process.

### Data processing pipeline

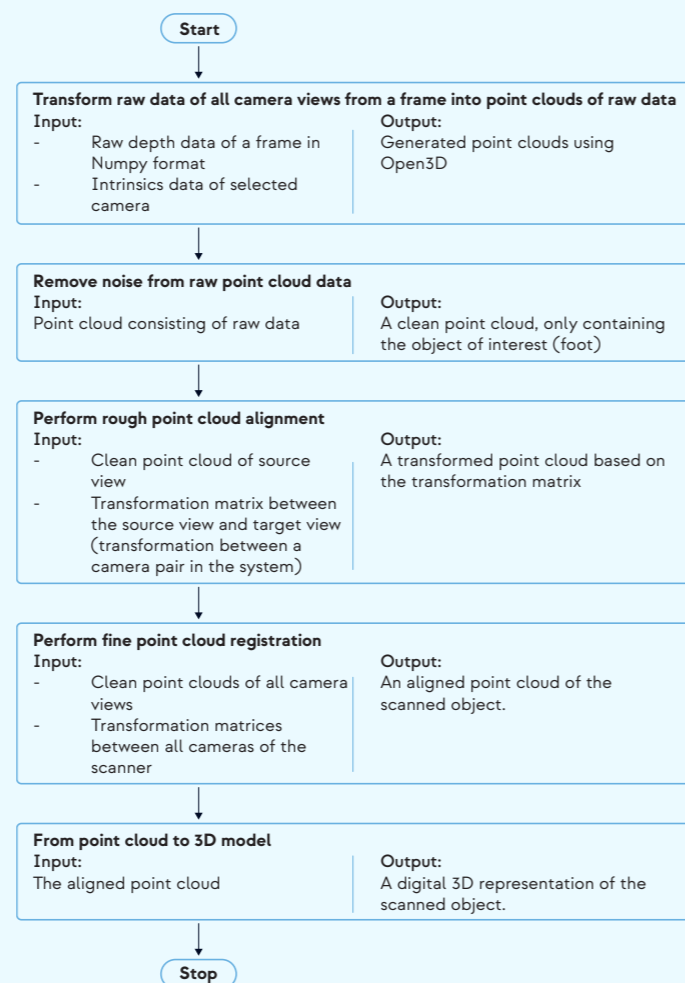


Figure 13.1 - A general representation of a data processing pipeline that is fitting to the use of 3D data.

The raw data can be cleaned in two ways:

- By automatically removing all points that are placed further than a certain distance threshold (e.g. by using Open3D). The disadvantage to this approach is that there is a lack of control. This approach is not recommended with inconsistent depth data.
- By using point cloud manipulation software, such as the open-source software Meshlab (Cignoni et al., 2008).

Figures 13.2 and 13.3 show the process of how raw point clouds are cleaned and the result after cleaning. This cleaning process should be done for every camera view. This will result in a set of clean point clouds which can be used for further data processing.

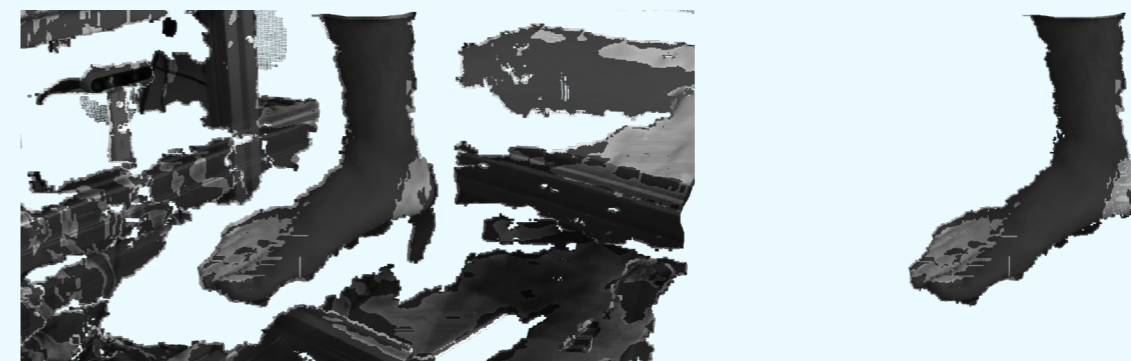


Figure 13.2 - Front view of the point cloud. (left) raw point cloud data. (right) the point cloud of the object of interest (foot) after preprocessing.



Figure 13.3 - Side view of the point cloud. (left) raw point cloud data. (right) the point cloud of the object of interest (foot) after preprocessing.

### 13.1.3 Rough alignment

Rough alignment is the process of applying initial transformation to a point cloud from one camera view relative to a point cloud from another camera view. The goal is to find a match in overlapping areas for each point cloud, like in figure 13.4. As discussed in chapter 5 and in equation 5.2, this is done by a transformation matrix  $T$ . The result is two point clouds that overlap which should make it easier for registration methods to find correspondence points.

The transformation matrix is normally acquired through camera calibration. Another approach is using a random sample consensus algorithm (RANSAC) (Fischler & Bolles, 1981), which is trying to roughly match point clouds with overlapping point cloud features. However, due to unforeseen reasons, RANSAC shows unpredictable behaviour when applied on the scanner point cloud data, as can be seen in figure 13.5. Again, point cloud manipulation software can also be used to manually reposition the point clouds and retrieve a transformation matrix  $T$ .

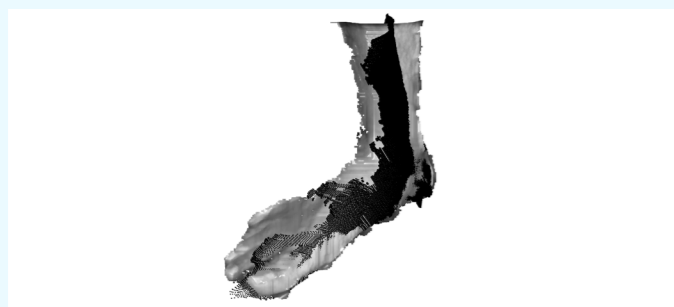


Figure 13.4 - Two point clouds (grey and black) that are roughly aligned.

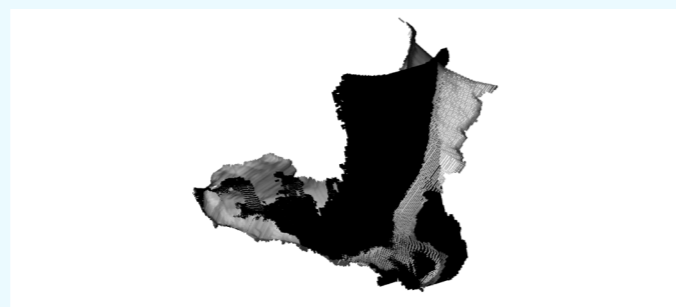


Figure 13.5 - Unpredictable RANSAC results for two separate RANSAC runs.



Figure 13.6 - 3D foot model which is used as reference model for nonrigid ICP registration.

### 13.1.4 Fine point cloud registration

The goal of fine point cloud registration is by matching the roughly aligned point clouds from all camera views into one point cloud that represents the scanned object. The most commonly applied point cloud registration method is Iterative Closest Point (ICP) (Chen & Medioni, 1991; Besl & McKay, 1992), which is also explored during this project. The goal of this algorithm is to find the largest correspondence of points between two point clouds, and is often used in the reconstruction of 2D and 3D surfaces. There are two types of ICP: rigid and nonrigid ICP. Also, many variants exist for both types of ICP. The results of the rigid and non rigid ICP registrations are discussed in chapter 13.2.

#### Rigid ICP

Rigid ICP is a type of ICP algorithm which tries to find a maximum number of correspondence points in two (overlapping) point clouds by respecting their geometry

and the relative distance of the data points in the point clouds. Rigid registration typically consists of translation and rotation to match the two point clouds.

Several types of rigid ICP methods were implemented using Open3D (Zhou, Park & Koltun, 2018):

- Global registration (Zhou, Park & Koltun, 2016), which does not require initial alignment;
- Fast global registration (Zhou, Park & Koltun, 2016), which is an improved global alignment method;
- Point-to-Point ICP (Besl & McKay, 1992);
- Point-to-Plane ICP (Rusinkiewicz & Levoy, 2001);
- Manual Point-to-Point ICP (Besl & McKay, 1992), with interactive initial alignment;
- Coloured point cloud registration (Park, Zhou & Koltun, 2017), which uses both color and geometry as variables for registration.



Figure 13.7 - Misalignment of two point clouds after initial alignment and Point-to-Plane ICP.

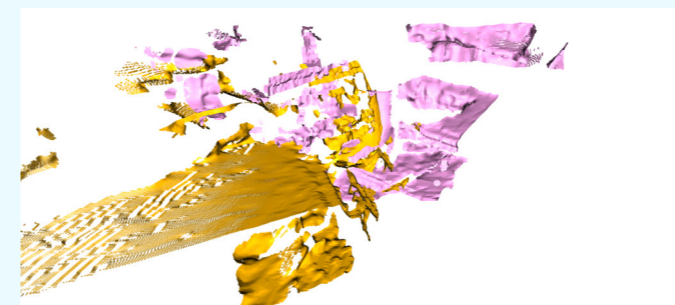
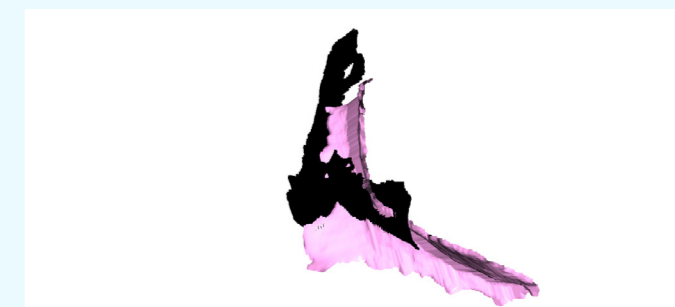


Figure 13.8 - (left) The source point cloud (yellow) is initially aligned with the target point cloud (pink), providing a large overlap of the two point clouds at the feet. (right) Misalignment of two point clouds after initial alignment and Point-to-Plane ICP. The source point cloud (yellow) is mapped upside down onto the target point cloud (pink).

## 13.2 Result

### 13.2.1 Rigid ICP

The implemented rigid ICP results were generally inconsistent and unpredictable. Tests were done with both raw and preprocessed point clouds, but ICP was not able to align overlapping point clouds properly with either of the types of data. The goal of ICP is to try and to maximize the correspondence of overlapping data points for both point clouds. Oddly enough, the ICP implementation seems to ignore the data points of the feet when using acquisition data from the prototyped scanner (figure 13.7).

From test runs, it appears that initial alignment of point clouds has a large influence on the outcome after the implementation of rigid ICP. However, when initial alignment is prepared (by retrieving matrix T from point cloud manipulation software), ICP discards the initial alignment completely, as shown in figure 13.8.

#### Nonrigid ICP

Nonrigid ICP is the method of finding the maximum correspondence between two point clouds through affine transformations, such as shear and scaling. For nonrigid ICP, a template of the desired general outcome is used, which is then deformed for a given stiffness factor according to the shape of the target point cloud. The outcome is a 3D model that respects the general proportions of the template, but is locally deformed to match the target point cloud.

For nonrigid ICP, the Optimal Step Nonrigid ICP method was implemented by F. Tajdari in Matlab. (Amberg, B., Romdhani, S., & Vetter, T., 2007). Static and dynamic scans were first preprocessed. A 3D foot model (figure 13.6) was used as a reference model, to constrain the overall shape of the foot.



Figure 13.9 (top, left) 3D model from static scan in midstance phase. (top, right) 3D model from dynamic scan in foot-flat phase. (bottom, left) 3D model from dynamic scan in midstance phase. (bottom, right) 3D model from dynamic scan in heel-off phase.

### 13.2.2 Nonrigid ICP

The nonrigid ICP implementation showed unexpectedly good results for registration. With the standard Optimal Step Nonrigid ICP method in Matlab, we were able to achieve realistic results that are usable in the design of custom foot orthotics and AFO's (W. ten Cate, personal communication, 16 August, 2021). According to W. ten Cate, the most important requirements for designing these orthotics are that the plantar surface and heel of the foot are clearly distinguishable.

Before applying nonrigid ICP, the scans were first roughly aligned. For this, transformation matrices for each of the cameras were first determined from manual rigid

registration in MeshLab. The transformation matrices are included in Appendix G.

Nonrigid ICP managed to construct 3D foot models from both the static foot scans, as well as the dynamic foot scans (figure 13.9). The dimensions of the 3D models were scaled down from the original dimensions of the physical foot: from 274 mm in a load bearing state (physical foot), to 0.4 mm (digital foot). This could be caused by a wrong depth step-size of the cameras, which can be resolved by changing the step-size value through the camera API. For this application, since the relative shape of the foot seems to be correct and the 3D model is a vector based model, the model can be scaled to the original foot size (274 mm) without disturbing the shape.

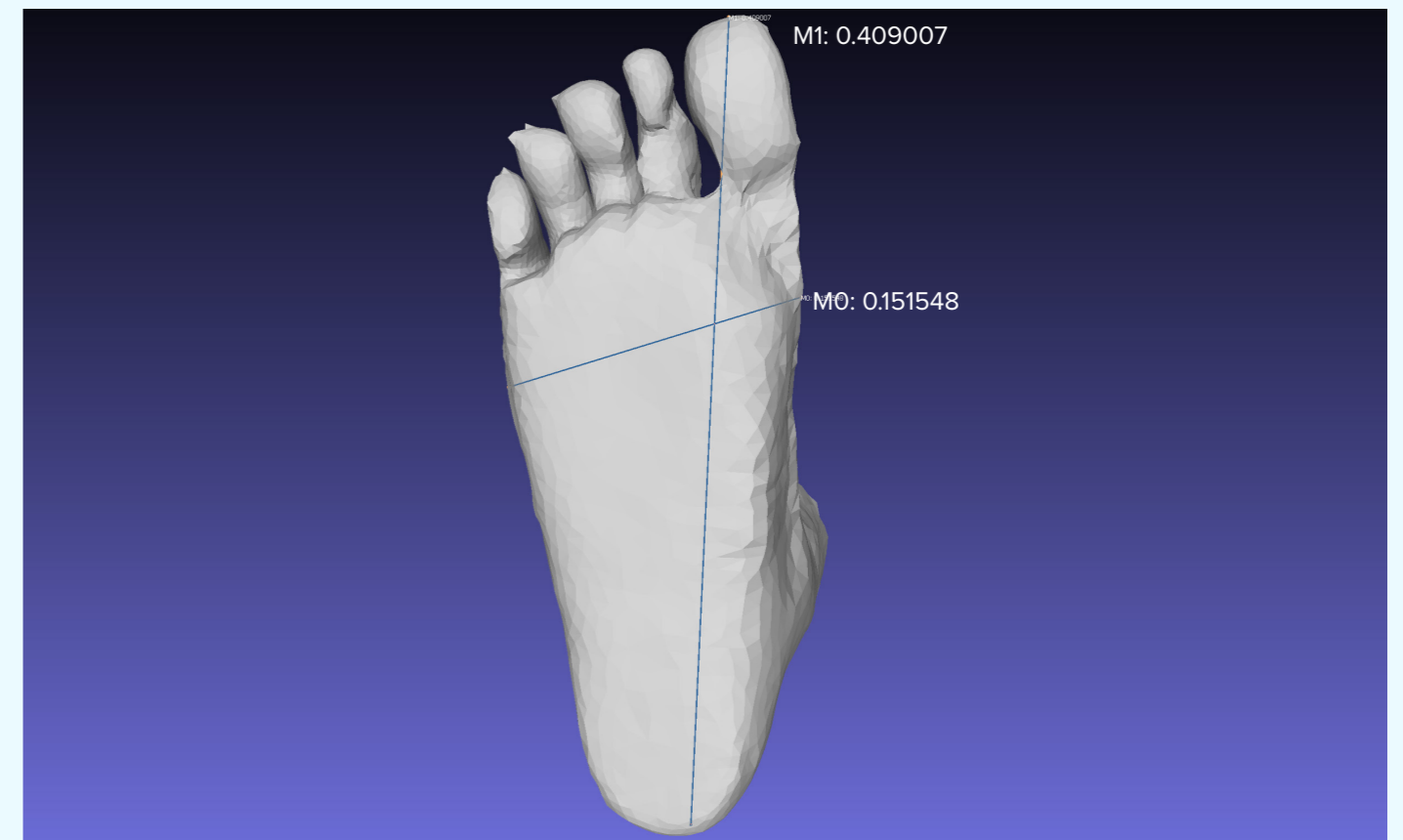


Figure 13.10 - The process of measuring the dimensions of the digital foot, which was done for all digital models. Measurements M0 and M1 represent the foot width and length in mm, respectively. As mentioned in chapter 13.2.2.

However, the 3D model must already be a processed mesh model and no point cloud when scaling, since it could otherwise result in less dense point clouds and therefore inaccurate results.

### 13.2.3 Preliminary accuracy validation

Validation of the accuracy of the 4D foot scanner is done by comparing the dimensions of the physical foot with the acquired 3D models. In accordance with ISO 7250:2017 standard, the foot length and foot width are the only relevant foot dimensions in generic footwear design, (so not personalized footwear design) [requirements MDR.1 and MDR.2]. Therefore, these dimensions were used in the validation process.

In order to comply with ISO 20685-1:2018 regulations, the static 3D scans of the foot should have an accuracy with a minimal error of 2 mm [requirement DA.1]. Since no standard mentions dynamic scans, the same minimal

error of 2 mm is taken as base [requirement DA.2].

For all scans, the foot dimensions (foot length and width) were measured with the help of MeshLab (figure 13.10). Based on the initial measurement of the digital foot length, a scaling ratio was determined, which is the original foot length over the measured foot length. This ratio is then applied to the measured digital foot width. The error of the scan (in mm) can be derived by taking the ratio of the original foot width over the measured scaled foot width, which should be less than 2 mm [requirement DA.1 & DA.2]. Note that the measuring of the foot length was done manually and could have caused discrepancies in measurement positions across the models.

Table 13.1 presents the error values for the relevant foot dimensions for each of the 4 digital 3D foot models, indicating the accuracy of both the static and dynamic

Scanner accuracy evaluation				
Original foot length (mm)	274			
Original foot width (mm)	104			
Length to width ratio	2.635			
Scanning state	Foot phase	Length to width ratio after scaling	Scan error (mm)	Absolute scan error (mm)
Static	Midstance	2.563	-2.793	2.793
Dynamic	Foot-flat	2.699	2.386	2.386
Dynamic	Midstance	2.576	-2.274	2.274
Dynamic	Heel-off	2.890	8.839	8.839

Table 13.1 - An overview of the scanner accuracy evaluation.

scans of the 4D foot scanner. The errors are obtained according to the aforementioned process. The “absolute scan error”-column indicates the error of the digital 3D model compared to the original foot. To be compliant with ISO standard 20685-1:2018, this value should be at least 2 mm, however lower is desired.

Table 13.1 shows that the static and dynamic scans foot is in a midstance phase (load bearing state) both have a negative scan error that is close to the 2 mm accuracy. The foot-flat and heel-off models (partially load bearing state) have a positive scan error, where the heel-off model has the highest error.

dimensions of the foot, the scan error is positive.

It should be noted that the accuracy validation gives a rough indication of the performance of the scanner, since the validation is done with only 4 3D foot models from acquired scan data. A more elaborate accuracy validation should be carried out with a larger set of 3D foot models that are acquired by scan data.

Furthermore, the 3D foot models in different phases of the gait cycle should be compared to a reference model that is positioned in the same phase. This is further detailed in the recommendations section (chapter 14).

### 13.3 Conclusions

The outcomes of the preliminary accuracy validation shows promising results regarding the performance of the scanner in commercial applications. For further development, a nonrigid ICP approach should be further explored, since this showed the most conclusive results.

The large error of the foot in the heel-off phase can be explained by the difference in foot dimensions during the midstance phase (load bearing) and the heel-off phase (partially load bearing from a different angle). Also, the width of a foot is more narrow in a non-weight bearing state (foot-flat phase is less weight bearing than the midstance phase) and as it elongates (as what happens in the heel-off phase). Because of the more narrow



## 14. Conclusion & recommendations

14.1	System optimization	P. 114
14.1.1	Hybrid camera setup	P. 114
14.1.2	Camera mounts manufacturing	P. 114
14.2	Optimized data acquisition and processing	P. 114
14.2.1	Asynchronous data acquisition	P. 114
14.2.2	Optimized data processing	P. 115
14.3	Automatic extrinsic camera calibration proposal	P. 115
14.4	Accuracy validation of the scanner	P. 116

Conclusions about the final outcome of this graduation project and recommendations for future development are discussed in this chapter.

The goal of this graduation project was to design an accurate and low-cost 4D foot scanner that can be used within the context of podiatry. To accomplish this goal, the following research questions were used as guidelines in the development process and have been answered throughout this thesis:

- Why should 4D foot scanning be introduced in the field of podiatry? - Chapter 4.4
- What is the added benefit of 4D foot scanning over 3D foot scanning? - Chapter 4.4
- How can Vidmar's foot scanner prototype (2020) be improved in terms of performance for static and dynamic foot scans? - Chapter 5 and 7

Throughout this thesis, these research questions have been answered. The result is the scanner, as presented in chapter 11, which is a step towards the development of a commercially available 4D foot scanner for podiatrists. With a total component cost of €3.809,06, the scanner includes: a camera configuration of 9 cameras, a system for the patient to interact with the scanner (trigger system), an improved scanning plate to accommodate the project context, and custom camera mounts to position the cameras. With this, the design challenges in chapter 7 are met.

From a price perspective and in comparison with existing commercial static 3D scanners, a preliminary conclusion can be made that the proposed 4D foot scanner takes a competitive position in the market. Since it is positioned at the lower bound of the range as defined in chapter 1 and does not exceed the threshold of €35.000. Considering the requirements that define the accuracy of a (static) 3D scanner, the project goal is not accomplished. However, with a minimal measured dynamic foot scan error of 2.274 mm, the scanner almost meets the ISO standards for 3D foot scanning (error of 2 mm).

## 14.1 System optimization

### 14.1.1 Hybrid camera setup

Chapter 11.2 presents a camera setup of 7 Intel RealSense D435i cameras. Since the system is able to manage the initialization and data acquisition of up to 9 cameras (more cameras are needed to test the upper limit of the camera configuration), 2 additional cameras can

be included in the configuration. Currently, the D435i cameras are positioned around and below the scanning plate. As the nonrigid 3D models in chapter 13.2 show, this setup is sufficient to acquire a 3D model of a foot. However, if detailed scans of the whole foot including the toes are desired, a hybrid camera approach should be considered of Intel RealSense D435 and D415 cameras. Since the D415 cameras have a smaller depth FOV, the pixel density of the depth image is larger than that of the D435(i) cameras, which is beneficial for identifying parts of the foot that are more intricate such as the toes. This might be desired within the context of podiatry or research into kinematics and geometry of feet during a gait cycle.

However, as indicated by W. ten Cate (personal communication, 16 August, 2021), within the context of modelling, designing and manufacturing of personalized foot orthotics (insoles and AFOs), detailed geometry of toes hinders this process and is unnecessary. From an orthotics perspective, the current camera configuration would be sufficient.

### 14.1.2 Camera mounts manufacturing

Due to the isotropic properties of FDM printing, parts of the mount are prone to breaking when applying pressure. Manufacturing the mounts using Stereolithography (SLA) or Selective Laser Sintering (SLS) results in a part with partially/completely anisotropic properties. Even though these manufacturing processes are more expensive than FDM printing, the camera mounts are of higher quality, will be more rigid and thus more resistant to applied force.

## 14.2 Optimized data acquisition and processing

### 14.2.1 Asynchronous data acquisition

The proposed data acquisition pipeline in chapter 12.1 presents a sequential data processing approach. Sequential processing was implemented to avoid hardware synchronization (which increases the hardware complexity of the scanner) and to decrease complexity during development.

An optimized data acquisition pipeline is recommended for future development of the scanner, by introducing

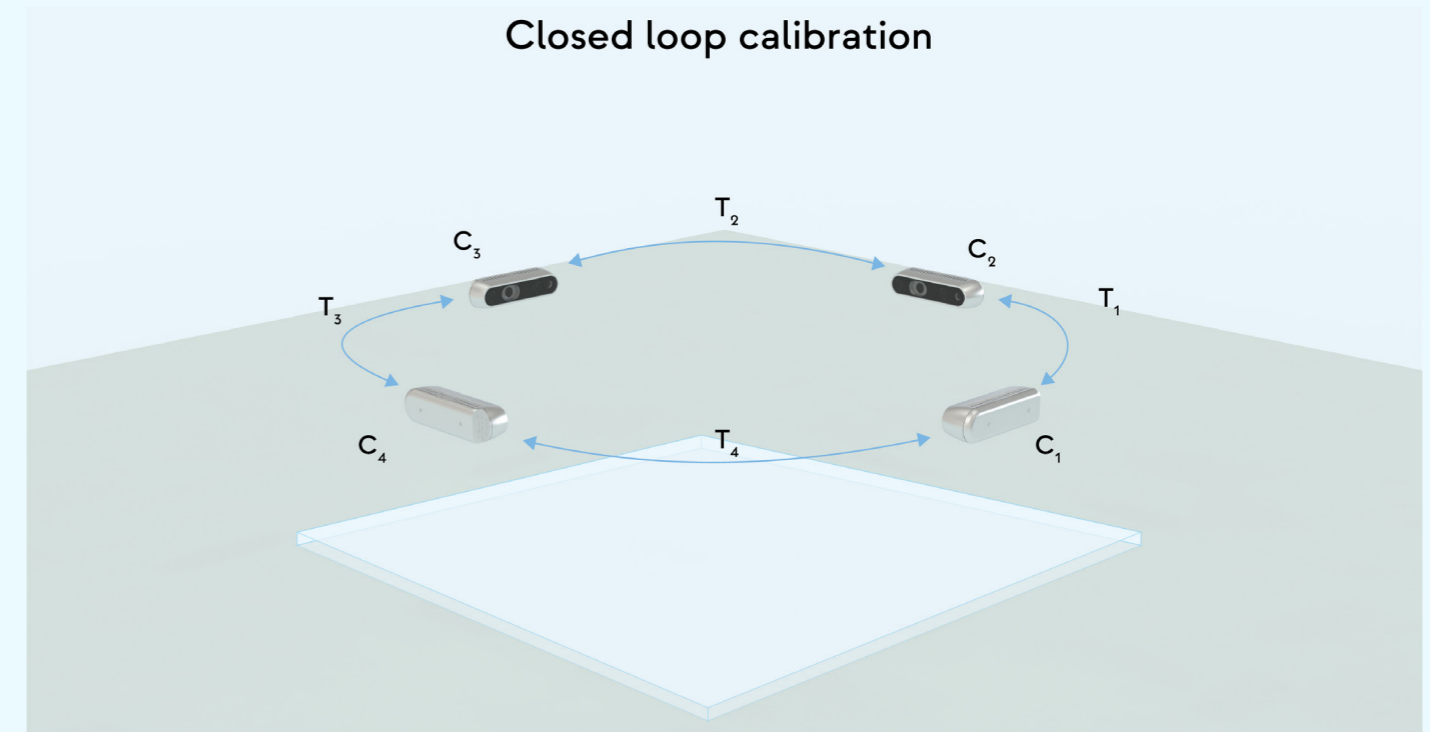


Figure 14.1 - The newly proposed closed loop extrinsic camera calibration method.

asynchronous acquisition, which will allow simultaneous data acquisition for all cameras.

The implementation of asynchronous acquisition can be achieved in Python by using multithreading. With multithreading in Python, every camera can run on a dedicated thread which is expected to increase the acquisition performance. However, due to Global Interpreter Lock (GIL) in Python (Python, 2020), true multithreading cannot be achieved as with C or C++ (sharing data between threads). However, using the Python multithreading module, it can likely be used in data acquisition, since data is written to memory and not shared by other threads. However, more exploration into this approach is necessary.

### 14.2.2 Optimized data processing

Current processing of the acquired data from memory to disk is time consuming and increases with large camera configurations. Current processing of this data as described in chapter 12.1 is done using the CPU. Future development could use the GPU for this processing, which is expected to significantly increase the speed of the data processing.

## 14.3 Automatic extrinsic camera calibration proposal

The open-loop pairwise calibration as presented in chapter 5 has two weaknesses:

- The calibration algorithm has an accumulating error with each camera that is added to the system, since each transformation matrix from one camera to the other is based on the transformation matrix of the previous pair.
- There is no error optimization, since the calibration is designed as an open loop system.

Together with F. Tajdari, a new camera calibration approach was drafted but not implemented. The new approach is a closed loop pairwise camera calibration, which relies on 2x2 ArUco boards with 4 mm sized markers that are embedded into the embodiment of the foot scanner (figure 14.1). With a closed loop approach, it is possible to iterate and converge the calibration error to a threshold accuracy that is acceptable for commercial 4D foot scanning, i.e. a minimum accuracy of 2 mm, according to ISO 20685-1:2018 standards.

The approach is detailed in Appendix H.1.

This automatic camera calibration approach improves upon Vidmar's approach (2020) in several ways with respect to the 4D foot scanner:

- By introducing automatic camera calibration, the user experience of the scanner operator/podiatrist is likely improved since extrinsic camera calibration can be done without supervision. By having an automatic camera calibration system, the podiatrist themselves will be able to run the extrinsic camera calibration tool, without the need to learn the specifics of camera calibration or the help of a third party that specializes in calibrating the scanner.
- Repositioning of a ChArUco board for every camera pair that needs to be calibrated will not be needed. This will become an increasingly larger task when cameras are added to the system. Eliminating this task is likely to improve the user experience and possibilities in user related calibration errors.
- Since patients are dynamically interacting with the foot scanner, offsets in camera position might be the result of this; for example when a patient bumps into a camera. To account for this possible disturbance, the podiatrist could regularly run the automatic calibration tool in order to restore the accuracy of the scanner. This will make for more constant measurements per analysis.

## 14.4 Accuracy validation of the scanner

Currently, the accuracy is validated by comparing the dimensions of the physical foot in a midstance phase (load bearing state) with digital models in a range of gait phases (foot-flat, midstance and heel-off). However, validation of the foot in phases other than the midstance should be done with a reference model that is positioned in a comparable gait phase.

To get dimensions of a reference model for different phases of the foot in the gait cycle, hand measurements could be taken. Another option is using a highly accurate 3D hand scanner, such as an Artec Eva (figure 4.5) to acquire the dimensions in different phases. The acquired 3D model from the 4D foot scanner can then be digitally evaluated using the digital model of the Artec Eva.

## IV. References

Active Arch. (2021). How it works. Retrieved from: <https://activearch.com/index.php/how-it-works/>

Adafruit. (2021). Adafruit VL53L0X Time of Flight Distance Sensor - ~30 to 1000mm. Retrieved from: <https://www.adafruit.com/product/3317>

Albayrak, A. (2021). Week two: eHealth Rules and Regulations [Powerpoint slides]. Retrieved from ID5741 eHealth, Delft University of Technology, The Netherlands.

AGC Glass Europe. (2021). Clearsight - AGC's anti-reflective glass. Retrieved from: <https://www.agc-yourglass.com/nl/nl/brands/clearsight>

Amberg, B., Romdhani, S., & Vetter, T. (2007, juni). Optimal Step Nonrigid ICP Algorithms for Surface Registration. 2007 IEEE Conference on Computer Vision and Pattern Recognition. 2007 IEEE Conference on Computer Vision and Pattern Recognition. <https://doi.org/10.1109/cvpr.2007.383165>

Arduino. (2021). Arduino Nano 33 BLE Sense. Retrieved from: <https://store.arduino.cc/arduino-nano-33-ble-sense>

Arduino. (2021). Arduino Uno Rev3. Retrieved from: <https://store.arduino.cc/arduino-uno-rev3>

ASTM F539-01(2017), Standard Practice for Fitting Athletic Footwear, ASTM International, West Conshohocken, PA, 2017, [www.astm.org](http://www.astm.org)

Barisch-Fritz, B., Schmeltzpfenning, T., Plank, C. & Grau, S. (2014). Foot deformation during walking: differences between static and dynamic 3D foot morphology in developing feet, *Ergonomics*, 57:6, 921-933, DOI: 10.1080/00140139.2014.899629

Basler. (2021). Pixel Format. Retrieved from: <https://docs.baslerweb.com/pixel-format#rgb-and-bgr-formats>

Besl, P. J., & McKay, N. D. A Method for Registration of 3D Shapes, *PAMI*, 1992.

Bradski, G. (2000). The OpenCV Library. *Dr. Dobb's Journal of Software Tools*, 120; 122-125.

Brown, T. (2009). Change by design: how design thinking transforms organizations and inspires innovation. New York: Harper Business.

Browning, R.C., Baker, E.A., Herron, J.A., Kram, R., (2006). Effects of obesity and sex on the energetic cost and preferred speed of walking. *Journal of Applied Physiology* 100, 390-398. doi:10.1152/jappphysiol.00767.2005.

Boppana, A., & Anderson, A. P. (2020). Dynamic foot morphology explained through 4D scanning and shape modeling. arXiv preprint [arXiv:2007.11077](https://arxiv.org/abs/2007.11077)

Boppana, A., Anderson, A.P., 2019. DynaMo: Dynamic Body Shape and Motion Capture with Intel RealSense Cameras. *The Journal of Open Source Software* 4. URL: <https://doi.org/10.21105/joss.01466>, doi:10.21105/joss.01466.

The Brannock Device Co, Inc. (2019). The Brannock Device Company. Retrieved from: <https://brannock.com/>

Chen, Y., & Medioni, G. (1992). Object modelling by registration of multiple range images. *Image and Vision Computing*, 10(3), 145–155. [https://doi.org/10.1016/0262-8856\(92\)90066-c](https://doi.org/10.1016/0262-8856(92)90066-c)

Cignoni, P., Callieri, M., Corsini, M., Dellepiane, M., Ganovelli, F., & Ranzuglia, G. (2008). MeshLab: an Open-Source Mesh Processing Tool. In *Eurographics Italian Chapter Conference*. The Eurographics Association. <https://doi.org/10.2312/LOCALCHAPTEREVENTS/ITALCHAP/ITALIANCHAPCONF2008/129-136>

Conrad. (2021). Joy-it Node MCU ESP32 Module. Retrieved from: <https://www.conrad.nl/p/joy-it-node-mcu-esp32-modul-printplaat-voor-ontwikkelaars-1656367>

DerSarkissian MD, C. (2020, March, 7). What are fallen arches? *WebMD*. <https://www.webmd.com/pain-management/what-are-fallen-arches>

Design Council. (2019). What is the framework for innovation? Design Council's evolved Double Diamond. Retrieved from: <https://www.designcouncil.org.uk/news-opinion/what-framework-innovation-design-councils-evolved-double-diamond>

DeskProto. (n.d.). How to CNC machine custom insoles. Retrieved from: <https://www.deskproto.com/gallery/orthopodo.php>

Choi, Q.-Y. Zhou, and V. Koltun, Robust Reconstruction of Indoor Scenes, *CVPR*, 2015.

Dimeglio, A., & Canavese, F. (2012). The French functional physical therapy method for the treatment of congenital clubfoot. *Journal of Pediatric Orthopaedics B*, 21(1), 28–39. <https://doi.org/10.1097/bpb.0b013e32834ee5f8>

Direct Orthotics. (n.d.). Ball of Foot pain. Retrieved from: <https://sites.google.com/orthoticselfie.com/direct-orthotics/ball-of-foot-pain>

Dobbs, M. B., & Gurnett, C. A. (2009). Update on Clubfoot: Etiology and Treatment. *Clinical Orthopaedics & Related Research*, 467(5), 1146–1153. <https://doi.org/10.1007/s11999-009-0734-9>

Eagle Pharmacy. (n.d.). Diabetic Shoes. Retrieved from: <https://www.eaglepharmacyandboutique.com/diabetic-shoes>

Eslami M, Begon M, Hinse S, Sadeghi H, Popov P, Allard P. Effect of foot orthoses on magnitude and timing of rearfoot and tibial motions, ground reaction force and knee moment during running. *J Sci Med Sport*. 2009 Nov;12(6):679-84. doi: 10.1016/j.jsams.2008.05.001. Epub 2008 Sep 3. PMID: 18768360.

European Commission. (2020). Medical Devices - Sector. Retrieved from [https://ec.europa.eu/health/md\\_sector/overview\\_en](https://ec.europa.eu/health/md_sector/overview_en)

European Commission. (2020). Qualification and Classification of stand alone software. Retrieved from <http://ec.europa.eu/DocsRoom/documents/17921/attachments/1/translations>

FDA. (2021). Product Classification. Retrieved from: <https://www.accessdata.fda.gov/scripts/cdrh/cfdocs/cfpccd/classification.cfm>

FDA. (2021). Product Classification. Retrieved from: <https://www.accessdata.fda.gov/scripts/cdrh/cfdocs/cfpccd/classification.cfm?id=5518>

Future Technology Systems. (n.d.). iQube & iQube Mini - 3D foot scanner. Retrieved from: <https://fts.gr/foot-scanner/>

Grunnet-Jepsen, A., Sweetser, J. N., Woodfill, J. (2020). Tuning depth cameras for best performance [Whitepaper]. Intel RealSense. <https://dev.intelrealsense.com/docs/tuning-depth-cameras-for-best-performance>

Grunnet-Jepsen, A., Takagi, A., Sweetser, J, Khuong, T. & Tong, D. (2021). External Synchronization of Intel® RealSense™ Depth cameras [Whitepaper]. Intel RealSense. <https://dev.intelrealsense.com/docs/external-synchronization-of-intel-realsense-depth-cameras>

Grunnet-Jepsen, A., Winer, P., Takagi, A., Sweetser, J., Zhao, K., Khuong, T., Nie, D. & Woodfill, J. (2021). Multi-Camera configurations - D400 Series Stereo Cameras [Whitepaper]. Intel RealSense. <https://dev.intelrealsense.com/docs/multiple-depth-cameras-configuration>

Hamamatsu. (2021). Si photodiodes. Retrieved from: <https://www.hamamatsu.com/eu/en/product/optical-sensors/photodiodes/si-photodiodes/index.html>

Harris, C.R., Millman, K.J., van der Walt, S.J. et al. Array programming with NumPy. *Nature* 585, 357–362 (2020). DOI: 10.1038/s41586-020-2649-2

Hawke, F., Burns, J., Radford, J. A., & du Toit, V. (2008). Custom-made foot orthoses for the treatment of foot pain. *Cochrane Database of Systematic Reviews*. <https://doi.org/10.1002/14651858.cd006801.pub2>

Healthline. (2017). Everything You Should Know About Metatarsalgia. Retrieved from: <https://www.healthline.com/health/metatarsalgia>

Hsu, W.-H., Lewis, C. L., Monaghan, G. M., Saltzman, E., Hamill, J., & Holt, K. G. (2014). Orthoses posted in both the forefoot and rearfoot reduce moments and angular impulses on lower extremity joints during walking. *Journal of Biomechanics*, 47(11), 2618–2625. <https://doi.org/10.1016/j.jbiomech.2014.05.021>

Huysmans, T., Goto, L., Molenbroek, J., & Goossens, R. (2020). DINED Mannequin. *Tijdschrift voor Human Factors*, 45(1).

Intel RealSense. (2018). Depth from Stereo. Retrieved from: <https://github.com/IntelRealSense/librealsense/blob/master/doc/depth-from-stereo.md>

Intel RealSense. (2021). Depth Camera D415. Retrieved from: <https://www.intelrealsense.com/depth-camera-d415/>

Intel RealSense. (2021). Depth Camera D435. Retrieved from: <https://www.intelrealsense.com/depth-camera-d435/>

Intel RealSense. (2021). Depth Camera D435i. Retrieved from: <https://www.intelrealsense.com/depth-camera-d435i/>

Intel RealSense. (2019). Frame Management. Retrieved from: <https://dev.intelrealsense.com/docs/frame-management>

Intel RealSense. (2020). Multi-Camera configurations - D400 Series Stereo Cameras. Retrieved from: <https://dev.intelrealsense.com/docs/multiple-depth-cameras-configuration>

Intel RealSense. (2021). Stereo Depth Camera D400. Retrieved from: <https://dev.intelrealsense.com/docs/stereo-depth-camera-d400>

International Organization for Standardization. (2017). Basic human body measurements for technological design — Part 1: Body measurement definitions and landmarks (ISO Standard No. 7250-1:2017). <https://www.iso.org/standard/65246.html>

International Organization for Standardization. (2016). Medical devices — Quality management systems — Requirements for regulatory purposes (ISO Standard No. 13485:2016). <https://www.iso.org/standard/59752.html>

International Organization for Standardization. (2018). 3-D scanning methodologies for internationally compatible anthropometric databases — Part 1: Evaluation protocol for body dimensions extracted from 3-D body scans (ISO Standard No. 20685-1:2018). <https://www.iso.org/standard/63260.html>

Joy-IT. (n.d.). NodeMCU ESP32. Retrieved from: <https://joy-it.net/en/products/SBC-NodeMCU-ESP32>

Kessler, E., Malladi, V. V. S., & Tarazaga, P. A. (2019). Vibration-based gait analysis via instrumented buildings. *International Journal of Distributed Sensor Networks*, 15(10), 155014771988160. <https://doi.org/10.1177/1550147719881608>

Kimura, M., Mochimaru, M., & Kanade, T. (2009). 3D measurement of feature cross-sections of foot while walking. *Machine Vision and Applications*, 22(2), 377–388. <https://doi.org/10.1007/s00138-009-0238-3>

Krauss I, Grau S, Mauch M, Maiwald C, Horstmann T: Sex-related differences in foot shape. *Ergonomics* 2008, 51:1693-1709.

Lecturio. (2021). Foot deformities. Retrieved from: <https://www.lecturio.com/concepts/foot-deformities/>

Luo, G., Stergiou, P., Worobets, J., Nigg, B., & Stefanyshyn, D. (2009). Improved footwear comfort reduces oxygen consumption during running. *Footwear Science*, 1(1), 25–29. <https://doi.org/10.1080/19424280902993001>

Maclean, C., Davis, I., & Hamill, J. (2008). Short- and Long-Term Influences of a Custom Foot Orthotic Intervention on Lower Extremity Dynamics. *Clinical Journal of Sport Medicine*, 18, 338-343.

Martin A. Fischler and Robert C. Bolles. 1981. Random sample consensus: a paradigm for model fitting with applications to image analysis and automated cartography. *Commun. ACM* 24, 6 (June 1981), 381–395. DOI:<https://doi.org/10.1145/358669.358692>

Materialise. (n.d.). Quality. Retrieved from: <https://www.materialise.com/>

en/about-materialise/quality

Materialise Motion. (n.d.). Measure. Retrieved from: <https://www.materialise.com/en/industries/motion/phits-suite/measure>

Materialise Phits Suite. (n.d.). 3D-print custom orthotics. Retrieved from: <https://www.materialise.com/en/industries/motion/phits-suite/3d-print-orthotics>

Max-Planck-Gesellschaft. (n.d.). 4D Foot Scanner. Retrieved from: <https://ps.is.tuebingen.mpg.de/pages/4d-foot-scanner>

Mayo Clinic. (2019). Metatarsalgia. Retrieved from: <https://www.mayoclinic.org/diseases-conditions/metatarsalgia/symptoms-causes/syc-20354790>

McKean MD, J. (n.d.). Diabetic Foot Ulcers. OrthoBullets. <https://www.orthobullets.com/foot-and-ankle/7046/diabetic-foot-ulcers>

Mentiplay, B. F., Banky, M., Clark, R. A., Kahn, M. B., & Williams, G. (2018). Lower limb angular velocity during walking at various speeds. *Gait & Posture*, 65, 190–196. <https://doi.org/10.1016/j.gaitpost.2018.06.162>

Mobilab. (n.d.). 3D Dynamic Scanning. Retrieved from: [http://www.applodynsca.mobilab.be/en/3d\\_dynamic\\_scanning/](http://www.applodynsca.mobilab.be/en/3d_dynamic_scanning/)

Moré J.J. (1978) The Levenberg-Marquardt algorithm: Implementation and theory. In: Watson G.A. (eds) *Numerical Analysis. Lecture Notes in Mathematics*, vol 630. Springer, Berlin, Heidelberg. <https://doi.org/10.1007/BFb0067700>

Murray, M. P., Drought, A. B., & Kory, R. C. (1964). Walking patterns of normal men. *JBJS*, 46(2), 335-360

Mueller, R. & Thoring, K. (2012). Design Thinking vs. Lean Startup: A comparison of two user-driven innovation strategies.

Nagymáté, G., & Kiss, R. M. (2019). Affordable gait analysis using augmented reality markers. *PLOS ONE*, 14(2), e0212319. <https://doi.org/10.1371/journal.pone.0212319>

Nictiz. (2019). Medische software: is CE-certificering nodig? Retrieved from: <https://www.nictiz.nl/nieuws/medische-software-is-ce-certificering-nodig/>

Nilsson, J., & Thorstensson, A. (1989). Ground reaction forces at different speeds of human walking and running. *Acta Physiologica Scandinavica*, 136(2), 217–227. <https://doi.org/10.1111/j.1748-1716.1989.tb08655.x>

NQA. (n.d.). Medical Device Standards. Retrieved from: <https://www.nqa.com/en-us/certification/sectors/medical-devices-services>

OpenCV. (2021). Calibration with ArUco and ChArUco. Retrieved from: [https://docs.opencv.org/4.5.2/da/d13/tutorial\\_aruco\\_calibration.html](https://docs.opencv.org/4.5.2/da/d13/tutorial_aruco_calibration.html)

Orange Insoles. (2020). How Great Insoles are Made: 4 Layers and Lots of Customer Observation. Retrieved from: <https://www.orangeinsoles.com/blogs/news/how-the-best-shoe-insoles-are-made>

OrthoInfo. (2019). Tarsal Coalition. Retrieved from: <https://orthoinfo.aaos.org/en/diseases--conditions/tarsal-coalition>

Ottawa Orthotic Lab inc. (n.d.). Services. Retrieved from: <https://www.ottawaorthoticlab.com/customorthotics>

Park, J., Zhou, Q.-Y., & Koltun, V. Colored Point Cloud Registration Revisited, ICCV, 2017.

Pololu. (2021). VL53L0X Time-of-Flight Distance Sensor Carrier with Voltage Regulator, 200cm Max. Retrieved from: <https://www.pololu.com/product/2490>

PolyLabs. (n.d.). Footwear: Insoles. Retrieved from: <https://polyurethanelaboratories.com/pu-polyurethane-products/footwear-insoles/>

Preferred Foot & Ankle Specialist. (2021). What Is Custom Orthotics Casting?. Retrieved from: <https://www.preferredfootankle.com/what-is-custom-orthotics-casting/>

Python. (2020). GlobalInterpreterLock. Retrieved from: <https://wiki.python.org/moin/GlobalInterpreterLock>

Rasenberg, N., Bierma-Zeinstra, S. M. A., Fuit, L., Rathleff, M. S., Dieker, A., van Veldhoven, P., Bindels, P. J. E., & van Middelkoop, M. (2020). Custom insoles versus sham and GP-led usual care in patients with plantar heel pain: results of the STAP-study - a randomised controlled trial. *British Journal of Sports Medicine*, 55(5), 272–278. <https://doi.org/10.1136/bjsports-2019-101409>

Rasenberg, N., Fuit, L., Poppe, E. et al. The STAP-study: The (cost) effectiveness of custom made orthotic insoles in the treatment for plantar fasciopathy in general practice and sports medicine: design of a randomized controlled trial. *BMC Musculoskeletal Disord* 17, 31 (2016). <https://doi.org/10.1186/s12891-016-0889-y>

Revopoint. (2019). Accuracy, Precision and Repeatability of 3D Depth Cameras. Retrieved from: <https://www.revopoint3d.com/accuracy-precision-and-repeatability-of-3d-depth-cameras/>

Ries, E. (2011). The lean startup: how today's entrepreneurs use continuous innovation to create radically successful businesses. New York: Crown Business.

Root, M. L. (1977). Normal and abnormal function of the foot. *Clinical biomechanics*, 2.

Rusinkiewicz, S., & Levoy, M. Efficient variants of the ICP algorithm. In 3-D Digital Imaging and Modeling, 2001.

Schiller J.R. (2012) Foot Pathology. In: Elzouki A.Y., Harfi H.A., Nazer H.M., Stapleton F.B., Oh W., Whitley R.J. (eds) *Textbook of Clinical Pediatrics*. Springer, Berlin, Heidelberg. [https://doi.org/10.1007/978-3-642-02202-9\\_410](https://doi.org/10.1007/978-3-642-02202-9_410)

Schmeltzpfenning, T., Plank, C., Krauss, I., Aswendt, P., & Grau, S. (2009). Dynamic foot scanning: A new approach for measurement of the human foot shape while walking. *Footwear Science*, 1(sup1), 28–30. <https://doi.org/10.1080/19424280902977111>

org/10.1080/19424280902977111

Strzalkowski N. D. J., Peters R. M., Inglis J. T. & Bent L.R. Cutaneous afferent innervation of the human foot sole: what can we learn from single-unit recordings? *J Neurophysiol*. 2018 Sep 1;120(3):1233-1246. doi: 10.1152/jn.00848.2017. Epub 2018 Jun 6. PMID: 29873612; PMCID: PMC6171067.

Telfer, S., Gibson, K. S., Hennessy, K., Steultjens, M. P., & Woodburn, J. (2012). Computer-Aided Design of Customized Foot Orthoses: Reproducibility and Effect of Method Used to Obtain Foot Shape. *Archives of Physical Medicine and Rehabilitation*, 93(5), 863–870. <https://doi.org/10.1016/j.apmr.2011.12.019>

Telfer, S., & Woodburn, J. (2010). The use of 3D surface scanning for the measurement and assessment of the human foot. *Journal of Foot and Ankle Research*, 3(1). <https://doi.org/10.1186/1757-1146-3-19>

The Linux Kernel. (n.d.). 2.8.2. V4L2\_PIX\_FMT\_Z16 ('Z16 '). Version 4.15.0. Retrieved from: <https://www.kernel.org/doc/html/v4.15/media/uapi/v4l/pixfmt-z16.html>

The Linux Documentation Project. (n.d.). Remote Serial Console HOWTO. Retrieved from: <https://tldp.org/HOWTO/Remote-Serial-Console-HOWTO/preparation-setspeed.html>

Thomas. (n.d.). All About Soda Lime Glass - Composition and Properties. Retrieved from: <https://www.thomasnet.com/articles/plant-facility-equipment/soda-lime-glass/>

Tsung, B. Y. S., Zhang, M., Fan, Y. B., & Boone, D. A. (2003). Quantitative comparison of plantar foot shapes under different weight-bearing conditions. *The Journal of Rehabilitation Research and Development*, 40(6), 517. <https://doi.org/10.1682/jrrd.2003.11.0517>

Vaverka, F., Elfmark, M., Svoboda, Z., & Janura, M. (2015). System of gait analysis based on ground reaction force assessment. *Acta Gymnica*, 45(4), 187–193. <https://doi.org/10.5507/ag.2015.022>

Vidmar, J. (2020). 4D foot scanner prototype development. [Master thesis, Technical University of Delft]. TU Delft Repository.

Voxelcare. (n.d.). 3D Laser Foot Scanner. Retrieved from: <https://www.voxelcare.com/#!/content/3d-laser-foot-scanner>

Voxelcare. (n.d.). 3D Foam Scanner. Retrieved from: <https://www.voxelcare.com/#!/content/3D-Laser-Foambox-Scanner>

Watts MD, E. & Sink MD, E. (n.d.). Tarsal Coalition. OrthoBullets. <https://www.orthobullets.com/pediatrics/4068/tarsal-coalition>

WebMD. (2020). Metatarsalgia. Retrieved from: <https://www.webmd.com/a-to-z-guides/metatarsalgia>

Whitney DPM, K. A. (2019, December). Overview of Foot and Ankle Disorders. MSD Manual Professional Version. <https://www.msmanuals.com/professional/musculoskeletal-and-connective-tissue-disorders/foot-and-ankle-disorders/overview-of-foot-and-ankle-disorders>

Wikipedia. (n.d.). Clubfoot. Retrieved from: <https://en.wikipedia.org/wiki/Clubfoot>

Wikipedia. (2021). USB 3.0. Retrieved from: [https://en.wikipedia.org/wiki/USB\\_3.0](https://en.wikipedia.org/wiki/USB_3.0)

Zhang, Z. (2014) Camera Parameters (Intrinsic, Extrinsic). In: Ikeuchi K. (eds) *Computer Vision*. Springer, Boston, MA. [https://doi.org/10.1007/978-0-387-31439-6\\_152](https://doi.org/10.1007/978-0-387-31439-6_152)

Zhang, X., Fang, G., Dai, C., Verlinden, J., Wu, J., Whiting, E., & Wang, C. C. L. (2017). Thermal-Comfort Design of Personalized Casts. *Proceedings of the 30th Annual ACM Symposium on User Interface Software and Technology. UIST '17: The 30th Annual ACM Symposium on User Interface Software and Technology*. <https://doi.org/10.1145/3126594.3126600>

Zhou, Q.-Y., Park, J., & Koltun, V. Fast Global Registration, ECCV, 2016.

Zhou, Q. Y., Park, J., & Koltun, V. (2018). Open3D: A modern library for 3D data processing. *arXiv preprint arXiv:1801.09847*

3dMD Inc. (n.d.). 3dMDfoot™ System Series. Retrieved from: <https://3dmd.com/products/#!/foot>

3D Scan Expert. (2017). Artec Eva 3D Scanner Review. Retrieved from: <https://3dscanexpert.com/artec-eva-3d-scanner-review/>

# Appendices

<b>Appendix A - Project structure</b>	<b>P. 124</b>
A.1 Double Diamond framework	P. 124
A.2 Lean Startup methodology	P. 125
<b>Appendix B - Vidmar's prototype (2020) identification</b>	<b>P. 126</b>
B.1 RealSense camera comparison	P. 126
B.2 Cost analysis	P. 126
<b>Appendix C - List of requirements</b>	<b>P. 128</b>
C.1 Medical Device regulations and standards	P. 128
<b>Appendix D - 4D foot scanning concepts</b>	<b>P. 130</b>
D.1 Cost analysis Concept 1	P. 130
D.2 Cost analysis Concept 2	P. 131
<b>Appendix E - Prototyping showcase</b>	<b>P. 132</b>
E.1 Bandwidth limitations	P. 132
E.2 Camera power consumption	P. 132
E.3 Scanning plate	P. 133
E.4 Custom camera mount	P. 135
E.5 Human Computer Interaction (trigger system)	P. 136
E.5.1 - Component selection	P. 136
E.5.2 - Communication	P. 137
E.5.3 - Embodiment	P. 138
E.5.4 - Bill of Materials & cost overview	P. 139
E.5.5 - Optimization recommendations	P. 140
E.6 External lighting	P. 140
E.7 Cost analysis	P. 143
<b>Appendix F - Data acquisition evaluation</b>	<b>P. 145</b>
F.1 Memory analysis	P. 145
F.2 Dynamic acquisition time	P. 147
<b>Appendix G - Data processing</b>	<b>P. 148</b>
<b>Appendix H - Camera calibration proposal</b>	<b>P. 148</b>

# Appendix A - Project structure

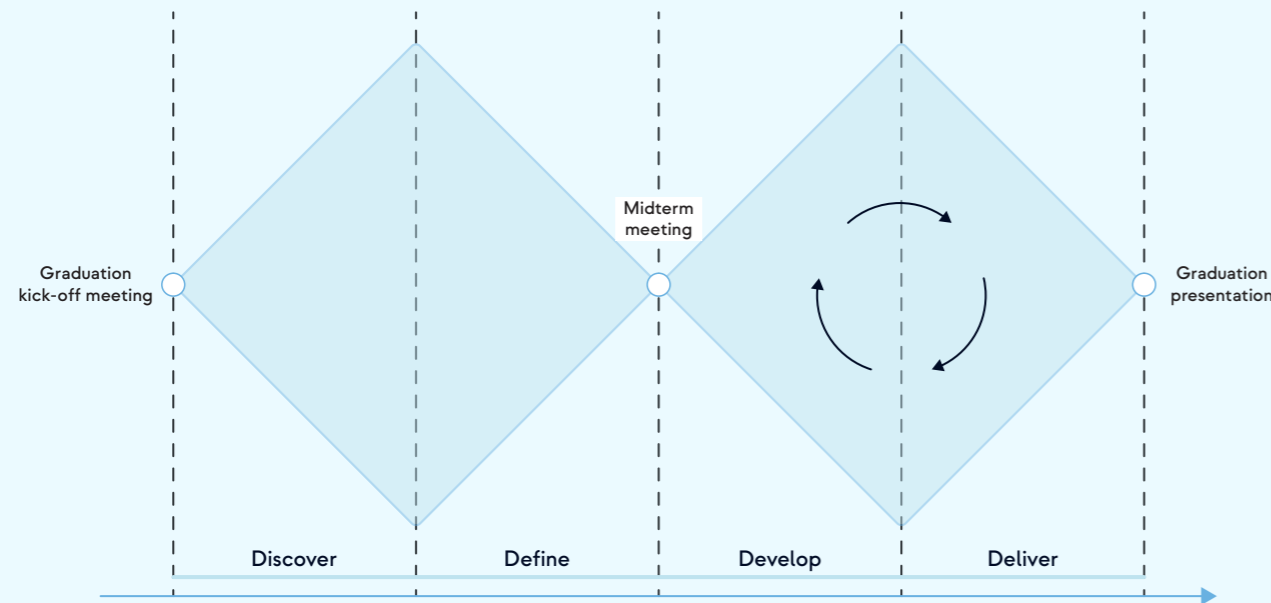


Figure A.1 - Double Diamond framework within this graduation project.

## A.1 Double Diamond framework

On a holistic level, the project adheres to the double diamond framework, which was developed by the British Design Council (2005). The framework consists of four phases to guide the process of a project: Discover, Define, Develop, and Deliver. In the development of a product, these phases help describe per phase in the project what to focus on. The framework consists of two diamonds:

- The first diamond consists of the Discover and Define phase: the first five to seven weeks of the project are dedicated to the Discover and Define phase; getting acquainted with (current) solutions and technologies, and acquiring fundamental knowledge is essential for the development phase. In this graduation project, the end of the Define phase is represented by the midterm presentation.
- The second diamond consists of the Development and Deliver phases. Here, the first diamond gives input (in terms of experience, knowledge and information) for further project development in the second diamond. This diamond has an iterative approach during the Development phase, especially in this graduation project where the goal is to optimize aspects of the product and improvements need to be made upon the previous state of the product. To support this iterative process, the Lean Startup methodology by Ries (2011) is adopted.

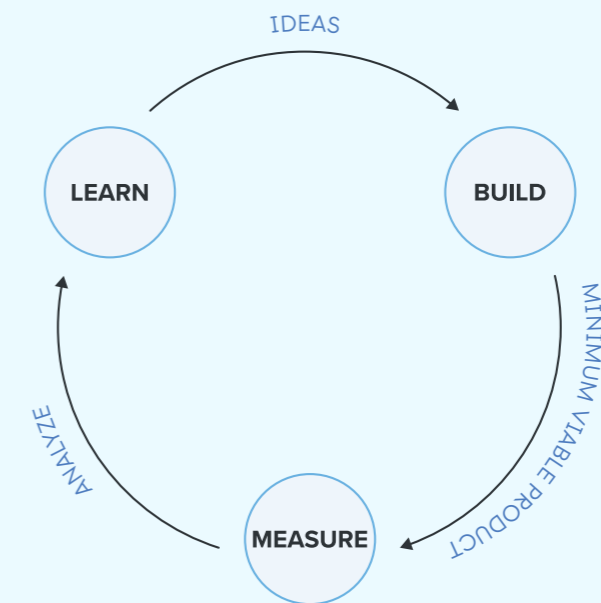


Figure A.2 - The Lean Startup methodology (Ries, 2011).

## A.2 Lean Startup methodology

Since the focus of the project is to build a physical working prototype, a considerable amount of time is scheduled for optimizing Vidmar's prototype, designing the physical aspect of the scanner and building and testing it. Also, the combination of focussing on the commercialization of the 4D foot scanner in podiatry and innovative (rapid) product development makes this project more suitable for the Lean Startup methodology than for Design Thinking (Mueller & Thoring, 2012). Especially during the Development phase, the Lean Startup methodology is maintained, since this method supports this highly iterative process/phase.

Sprints of two weeks are used to aim for completing intermediate milestones in the development process. Each sprint has a certain goal to achieve within the set timeline, and contains a full iteration as presented by the Lean Startup methodology in figure A.2.

# Appendix B - Vidmar's prototype identification

Comparison table - Intel RealSense D415, D435 & D435i			
Specifications	Intel RealSense D415	Intel RealSense D415 module (including Vision D4 processor board + 50-pin rigid interposer)	Intel RealSense D435(i)
Price	€ 148,66	€ 95,56	€ 168,55 / € 186.08
Image sensor technology	Rolling Shutter	Rolling Shutter	Global Shutter
Ideal range	0.5 to 3 m	0.5 to 3 m	0.3 to 3 m
Depth technology	Stereoscopic	Stereoscopic	Stereoscopic
Depth Field of View (FOV)	65° × 40°	65° × 40°	87° × 58°
Minimum Depth Distance (Min-Z) at Max Resolution	~45 cm	~45 cm	~ 28 cm
Depth Accuracy	< 2 % at 2 m	< 2 % at 2 m	< 2 % at 2 m
Depth Stream Output Frame Rate	Up to 90 fps	Up to 90 fps	Up to 90 fps
RGB Frame Resolution	1920 × 1080	1920 × 1080	1920 × 1080
RGB Frame Rate	30 fps	30 fps	30 fps
RGB Sensor FOV	69° × 42°	69° × 42°	69° × 42°
Camera Module	Intel RealSense Module D415	Intel RealSense Module D415	Intel RealSense Module D430 + RGB Camera

Table B.1 - Comparison of the Intel RealSense D415, D435 and D435i (Intel, 2021).

## B.1 RealSense camera comparison

Table B.1 lists the specifications of three Intel RealSense cameras: the D415, the D435 and the D435i camera. These specifications are leading in the recommendation on data capturing devices in the Intel RealSense D400-family.

## B.2 Cost analysis

Table B.2 presents the cost analysis of Vidmar's prototype (2020). The overview includes 5 cameras instead of the presented 4 cameras from Vidmar to give a more realistic cost representation of the scanner when enough cameras are connected to the system.

Amount of modules		5					
Product	Supplier	Remarks	Amount	Price (€) incl. VAT	Subtotal (€) incl. VAT	URL	
Acquisition modules	Raspberry Pi 4 Model B (4GB)	Mouser		5	€60.00	€300.00	<a href="https://nl.mouser.com/ProductDetail/SparkFun/DEV-15447?qs=d0WKA%252BL4KYKa%2FhHqY8NQ%3D%3D">https://nl.mouser.com/ProductDetail/SparkFun/DEV-15447?qs=d0WKA%252BL4KYKa%2FhHqY8NQ%3D%3D</a>
	Intel RealSense D435i	Mouser		5	€186.08	€930.40	<a href="https://nl.mouser.com/ProductDetail/Intel/82635D435DK5P?qs=PqoDHvF64%252B5RxJ3DyHfHg%3D%3D">https://nl.mouser.com/ProductDetail/Intel/82635D435DK5P?qs=PqoDHvF64%252B5RxJ3DyHfHg%3D%3D</a>
	Sandisk Extreme Micro SD 32 GB U3 (100 MB/s)	DatalO		5	€11.49	€57.45	<a href="https://www.dataio.nl/sandisk-extreme-micro-sd-32gb-met-adapter/">https://www.dataio.nl/sandisk-extreme-micro-sd-32gb-met-adapter/</a>
	Kingston A2000 250GB	Megekko		5	€39.90	€199.50	<a href="https://www.megekko.nl/product/0/266798/Kingston-SSD-A2000-250GB">https://www.megekko.nl/product/0/266798/Kingston-SSD-A2000-250GB</a>
	ICY BOX IB-1817M-C31 external M.2 enclosure USB C	Megekko		5	€43.95	€219.75	<a href="https://www.megekko.nl/product/3752/1037461/M-2-Behuizingen/ICY-BOX-IB-1817M-C31-externe-M-2-behuizing-USB-C-grjls">https://www.megekko.nl/product/3752/1037461/M-2-Behuizingen/ICY-BOX-IB-1817M-C31-externe-M-2-behuizing-USB-C-grjls</a>
	<b>Total module costs</b>					<b>€1,707.10</b>	
Desktop PC	Intel i7 920	N/A	Price is from 2013. Not for sale anymore.	1	€260.00	€260.00	<a href="https://tweakers.net/pricewatch/248378/zotac-geforce-gtx260-amp.html">https://tweakers.net/pricewatch/248378/zotac-geforce-gtx260-amp.html</a>
	Asus P6T7 WS SuperComputer	N/A	Price is from 2013. Not for sale anymore.	1	€400.00	€400.00	<a href="https://tweakers.net/pricewatch/248378/zotac-geforce-gtx260-amp.html">https://tweakers.net/pricewatch/248378/zotac-geforce-gtx260-amp.html</a>
	Samsung Evo 850 SSD (1TB)	N/A		1	€103.00	€103.00	<a href="https://tweakers.net/pricewatch/422397/samsung-850-evo-1tb.html">https://tweakers.net/pricewatch/422397/samsung-850-evo-1tb.html</a>
	Startech 4 Port USB 3.1 PCI-e Card - 10Gbps PCI Express Expansion Card / Adapter	Megekko		1	€79.95	€79.95	<a href="https://www.megekko.nl/product/2308/991522/USB-uitbreidingskaarten/StarTech-com-4-poorts-PCI-Express-PCI-e-Super-Speed-USB-3-0-kaartadapter-met-2-speciale-5-Gbps-kanal">https://www.megekko.nl/product/2308/991522/USB-uitbreidingskaarten/StarTech-com-4-poorts-PCI-Express-PCI-e-Super-Speed-USB-3-0-kaartadapter-met-2-speciale-5-Gbps-kanal</a>
	Zotac Geforce GTX 260 Amp Graphics Card	N/A	Price is from 2012. Not for sale anymore.	1	€314.00	€314.00	<a href="https://tweakers.net/pricewatch/248378/zotac-geforce-gtx260-amp.html">https://tweakers.net/pricewatch/248378/zotac-geforce-gtx260-amp.html</a>
	Sweex Power Supply 650 W	N/A	Price is from 2012. Not for sale anymore.	1	€50.00	€50.00	<a href="https://tweakers.net/pricewatch/168868/sweex-power-supply-650w.html">https://tweakers.net/pricewatch/168868/sweex-power-supply-650w.html</a>
	<b>Total PC costs</b>					<b>€1,206.95</b>	
Embodiment components	Aluminium profile - 1.11.050050.43L	Alucomp	Length: 400 mm	12	€15.34	€184.11	<a href="https://www.alucomp.nl/11105005043160-aluminium-profiel">https://www.alucomp.nl/11105005043160-aluminium-profiel</a>
	Aluminium profile - 1.11.050050.43L	Alucomp	Length: 500 mm	6	€18.72	€112.31	<a href="https://www.alucomp.nl/11105005043160-aluminium-profiel">https://www.alucomp.nl/11105005043160-aluminium-profiel</a>
	Aluminium profile - 1.11.050050.43L	Alucomp	Length: 600 mm	4	€22.09	€88.38	<a href="https://www.alucomp.nl/11105005043160-aluminium-profiel">https://www.alucomp.nl/11105005043160-aluminium-profiel</a>
	Aluminium profile - 1.11.050050.43L	Alucomp	Length: 1000 mm	4	€35.62	€142.49	<a href="https://www.alucomp.nl/11105005043160-aluminium-profiel">https://www.alucomp.nl/11105005043160-aluminium-profiel</a>
	Aluminium profile - 1.46.204.57571	Alucomp	Corner connector 57 x 57 mm)	24	€6.27	€150.43	<a href="https://www.alucomp.nl/14620438761-2">https://www.alucomp.nl/14620438761-2</a>
	Rose+Krieger Flange Brackets	DigiKey	Length: 40 mm	2	€6.13	€12.27	<a href="https://www.digikey.nl/product-detail/en/rose-krieger/4816702/1758-1019-ND/7200998">https://www.digikey.nl/product-detail/en/rose-krieger/4816702/1758-1019-ND/7200998</a>
	Rose+Krieger SLOT STONE F 30MM, M5	DigiKey		48	€1.59	€76.08	<a href="https://www.digikey.nl/product-detail/en/rose-krieger/4006711/1758-1040-ND/7201019">https://www.digikey.nl/product-detail/en/rose-krieger/4006711/1758-1040-ND/7201019</a>
	Socket head M5 x 20 mm galvanized	Gamma	12 pieces per pack <b>Density:</b> 1.2e3 kg/m <sup>3</sup> (Granta Edupack, 2021) <b>Dimensions:</b> 600 x 600 x 15 mm (l x w x h) <b>Volume:</b> 0.0054 m <sup>3</sup> <b>Weight:</b> 6.48 kg <b>Price:</b> \$ 0.99/kg = € 0.84/kg (July, 2021)	1	€2.69	€2.69	<a href="https://www.gamma.nl/assortiment/gamma-inbusbout-m5-x-20-mm-cilinderkop-verzinkt-12-stuks/p/B458107">https://www.gamma.nl/assortiment/gamma-inbusbout-m5-x-20-mm-cilinderkop-verzinkt-12-stuks/p/B458107</a>
	15 mm extruded acrylic plate	Foshan Shunde Lunjiao Xishun Plastic Factory		1	€5.44	€5.44	<a href="https://www.alibaba.com/product-detail/Acrylic-1mm-12mm-Sheet-Clear-Sheets_62217506442.html">https://www.alibaba.com/product-detail/Acrylic-1mm-12mm-Sheet-Clear-Sheets_62217506442.html</a>
	Plywood hardwood - 1220 x 610 x 15 mm (l x w x h)	Gamma	1000 x 600 x 15 (l x w x h) - 2 par	3	€16.79	€50.37	<a href="https://www.gamma.nl/assortiment/multiplex-hardhout-122x61-cm-15-mm/pi/B454826">https://www.gamma.nl/assortiment/multiplex-hardhout-122x61-cm-15-mm/pi/B454826</a>
<b>Total embodiment costs</b>					<b>€824.58</b>		
<b>Total prototype cost</b>					<b>€3,738.63</b>		

Table B.2 - Cost analysis of Vidmar's prototype, containing all components of the prototype.



# Appendix C - List of requirements

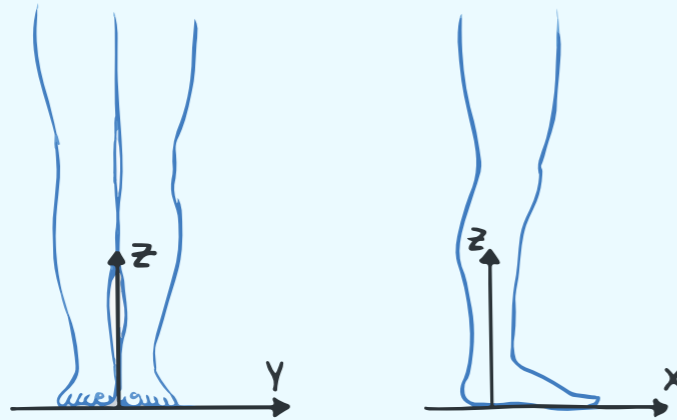


Figure C.1 - x, y, z coordinate system as defined by ISO 20685-1:2018.

## C.1 Medical Device regulations and standards

The development of a commercial 4D foot scanner comes with a list of regulations and standards that the scanner has to adhere to in order to be used in a commercial and healthcare environment (NQA, n.d.). The most prominent ISO standards that the scanner needs to conform to, relevant to 3D body acquisition, measurement aspects and commercialization, are: **ISO 7250-1:2017/7250-2:2017**, **ISO 20685-1:2018**, and **ISO 13485:2016**.

### ISO 7250-1:2017/7250-2:2017 standard

This standard describes the basic human body measurements for technological design (ISO 7250-1:2017) and statistical summaries of body measurements from individual ISO populations (ISO 7250-2:2017). Within this standard, only two foot related measurements are included: the foot length and foot breadth, both in a static and weight bearing state, where the subject stands with weight equally distributed on both feet. The maximum allowable difference between values obtained by the method described in ISO 7250-1 and other methods is 2 mm.

### ISO 20685-1:2018 standard

This standard describes the 3-D scanning methodologies for internationally compatible anthropometric databases. In particular, part 1 describes the evaluation protocol

for body dimensions extracted from 3-D body scans. In order for a 3D body scanner to be used for 3D human body data acquisition, it needs to comply with the ISO 20685-1:2018 standard. Even though 4D scanning is not specifically mentioned, it does describe the use of point clouds, which are used to assess body measurements. The accuracy requirements of the extracted measurements refer to ISO 7250-1:2017, which is 2 mm.

Furthermore, the standard describes a methodology for a validation study to establish accuracy of body dimensions extracted from scanners, including a *defined x, y, z coordinate system* (figure C.1). The x-axis is defined by the sagittal axis (fore-to-aft direction), the y-axis is defined by the transverse axis (side-to-side direction), and the z-axis is defined by the longitudinal axis (top-to-bottom direction).

### ISO 13485:2016 standard

The ISO 13485:2016 standard describes a quality management system and is a standard specifically for medical devices, based on the ISO 9001 standard. The standard is more relevant to the organisation distributing/commercializing the 4D foot scanner, rather than to the foot scanner. It is not mandatory for an organisation to comply with this standard, but the law requires the existence of a quality management system. This ISO standard shows clients that an organisation complies to the legal requirements and enhances the reliability of the medical device. Complying to this standard requires extensive documentation and instructions, which are

more relevant towards the actual commercialization of the product.

### Medical Device Regulations (MDR)

Next to these ISO standards, the European Commission has set regulations to which medical devices have to adhere to. Following the infographic of Nictiz (2019) in combination with the decision tree of the MEDDEV 2.1/6 (2016), a 4D foot scanner can be classified as a medical device that is used to make decisions for diagnostic and therapeutic purposes. This makes the 4D foot scanner a medical device, falling under MDR. The scanner has no association with the In Vitro Diagnostic Regulation (IVDR), since this regulation only applies to software and devices that are involved in in-vitro diagnostics.

The 4D foot scanner can be classified as a Class I 'low risk' device, since it is a non-invasive device that only touches the skin of a patient. Comparable scanners are also classified as Class I products, even a nuclear whole body scanner, used in radiology (FDA, 2021).

### Regulation (EU) 2017/745

This regulation imposes rules concerning the placement of a medical device on the market, making available on the market or including medical devices into services for human use and accessories for such devices in the Union. This regulation repeals Directive 93/42/EEC, which concerns medical devices (Albayrak, 2021).

# Appendix D - 4D foot scanning concepts

Amount of modules		5					
Product	Supplier	Remarks	Amount	Price (€) incl. VAT	Subtotal (€) incl. VAT	URL	
Raspberry Pi 4 Model B (4GB)	Mouser		5	€60.00	€300.00	<a href="https://nl.mouser.com/ProductDetail/SparkFun/DEV-15447?qs=d0WKAP%252BL4KYKa%2FhHqY8NQ%3D%3D">https://nl.mouser.com/ProductDetail/SparkFun/DEV-15447?qs=d0WKAP%252BL4KYKa%2FhHqY8NQ%3D%3D</a>	
Intel RealSense D435i	Mouser		5	€186.08	€930.40	<a href="https://nl.mouser.com/ProductDetail/Intel/82635D435IDK5P?qs=PqoDHHvF64%252B5RxJ3DyHfHg%3D%3D">https://nl.mouser.com/ProductDetail/Intel/82635D435IDK5P?qs=PqoDHHvF64%252B5RxJ3DyHfHg%3D%3D</a>	
Sandisk Extreme Micro SD 32 GB U3 (100 MB/s)	DatalO		5	€11.49	€57.45	<a href="https://www.dataio.nl/sandisk-extreme-micro-sd-32gb-met-adapter/">https://www.dataio.nl/sandisk-extreme-micro-sd-32gb-met-adapter/</a>	
Kingston A2000 250GB	Megekko		5	€39.90	€199.50	<a href="https://www.megekko.nl/product/0/266798/Kingston-SSD-A2000-250GB">https://www.megekko.nl/product/0/266798/Kingston-SSD-A2000-250GB</a>	
ICY BOX IB-1817M-C31 external M.2 enclosure USB C	Megekko		5	€43.95	€219.75	<a href="https://www.megekko.nl/product/3752/1037461/M-2-Behuizingen/ICY-BOX-IB-1817M-C31-externe-M-2-behuizing-USB-C-grjls">https://www.megekko.nl/product/3752/1037461/M-2-Behuizingen/ICY-BOX-IB-1817M-C31-externe-M-2-behuizing-USB-C-grjls</a>	
<b>Total module costs</b>					<b>€1,707.10</b>		
Product	Supplier	Remarks	Amount	Price (€) incl. VAT	Subtotal (€) incl. VAT	URL	
Intel i7 920	N/A	Price is from 2013. Not for sale anymore.	1	€260.00	€260.00	<a href="https://tweakers.net/pricewatch/248378/zotac-geforce-gtx260-amp.html">https://tweakers.net/pricewatch/248378/zotac-geforce-gtx260-amp.html</a>	
Asus P6T7 WS SuperComputer	N/A	Price is from 2013. Not for sale anymore.	1	€400.00	€400.00	<a href="https://tweakers.net/pricewatch/248378/zotac-geforce-gtx260-amp.html">https://tweakers.net/pricewatch/248378/zotac-geforce-gtx260-amp.html</a>	
Samsung Evo 850 SSD (1TB)	N/A		1	€103.00	€103.00	<a href="https://tweakers.net/pricewatch/422397/samsung-850-evo-1tb.html">https://tweakers.net/pricewatch/422397/samsung-850-evo-1tb.html</a>	
Startech 4 Port USB 3.1 PCI-e Card - 10Gbps PCI Express Expansion Card / Adapter	Megekko		1	€79.95	€79.95	<a href="https://www.megekko.nl/product/2308/991522/USB-uitbreidingskaarten/StarTech-com-4-poorts-PCI-Express-PCI-e-Super-Speed-USB-3-0-kaartadapter-met-2-speciale-5-Gbps-kanal">https://www.megekko.nl/product/2308/991522/USB-uitbreidingskaarten/StarTech-com-4-poorts-PCI-Express-PCI-e-Super-Speed-USB-3-0-kaartadapter-met-2-speciale-5-Gbps-kanal</a>	
Zotac Geforce GTX 260 Amp Graphics Card	N/A	Price is from 2012. Not for sale anymore.	1	€314.00	€314.00	<a href="https://tweakers.net/pricewatch/248378/zotac-geforce-gtx260-amp.html">https://tweakers.net/pricewatch/248378/zotac-geforce-gtx260-amp.html</a>	
Sweex Power Supply 650 W	N/A	Price is from 2012. Not for sale anymore.	1	€50.00	€50.00	<a href="https://tweakers.net/pricewatch/168868/sweex-power-supply-650w.html">https://tweakers.net/pricewatch/168868/sweex-power-supply-650w.html</a>	
<b>Total PC costs</b>					<b>€1,206.95</b>		
Product	Supplier	Remarks	Amount	Price (€) incl. VAT	Subtotal (€) incl. VAT	URL	
Aluminium profile - 1.11.050050.43L	Alucomp	Length: 400 mm	12	€15.34	€184.11	<a href="https://www.alucomp.nl/11105005043160-aluminium-profiel">https://www.alucomp.nl/11105005043160-aluminium-profiel</a>	
Aluminium profile - 1.11.050050.43L	Alucomp	Length: 500 mm	6	€18.72	€112.31	<a href="https://www.alucomp.nl/11105005043160-aluminium-profiel">https://www.alucomp.nl/11105005043160-aluminium-profiel</a>	
Aluminium profile - 1.11.050050.43L	Alucomp	Length: 600 mm	4	€22.09	€88.38	<a href="https://www.alucomp.nl/11105005043160-aluminium-profiel">https://www.alucomp.nl/11105005043160-aluminium-profiel</a>	
Aluminium profile - 1.11.050050.43L	Alucomp	Length: 1000 mm	4	€35.62	€142.49	<a href="https://www.alucomp.nl/11105005043160-aluminium-profiel">https://www.alucomp.nl/11105005043160-aluminium-profiel</a>	
Aluminium profile - 1.46.204.57571	Alucomp	Corner connector 57 x 57 mm)	24	€6.27	€150.43	<a href="https://www.alucomp.nl/14620438761-2">https://www.alucomp.nl/14620438761-2</a>	
Rose+Krieger Flange Brackets	DigiKey	Length: 40 mm	2	€6.13	€12.27	<a href="https://www.digikey.nl/product-detail/en/rose-krieger/4816702/1758-1019-ND/7200998">https://www.digikey.nl/product-detail/en/rose-krieger/4816702/1758-1019-ND/7200998</a>	
Rose+Krieger SLOT STONE F 30 MM, M5	DigiKey		48	€1.59	€76.08	<a href="https://www.digikey.nl/product-detail/en/rose-krieger/4006711/1758-1040-ND/7201019">https://www.digikey.nl/product-detail/en/rose-krieger/4006711/1758-1040-ND/7201019</a>	
Socket head M5 x 20 mm galvanized	Gamma	12 pieces per pack	1	€2.69	€2.69	<a href="https://www.gamma.nl/assortiment/gamma-inbusbout-m5-x-20-mm-cilinderkop-verzinkt-12-stuks/p/B458107">https://www.gamma.nl/assortiment/gamma-inbusbout-m5-x-20-mm-cilinderkop-verzinkt-12-stuks/p/B458107</a>	
12 mm tempered soda lime glass, 600 x 600 MM	Alkema Technical Glass Solutions	AGC 12 mm Planibel Clearvision glass - low iron concentration, with 92 % light transmission.	1	€105.00	€105.00	<a href="https://www.agc-yourglass.com/nl-BE/merken/planibel-extra-clear">https://www.agc-yourglass.com/nl-BE/merken/planibel-extra-clear</a>	
<b>Total embodiment costs</b>					<b>€873.77</b>		
<b>Total prototype cost</b>					<b>€3,787.82</b>		

Table D.1 - Cost analysis of concept 1, containing all components of the prototype.

## D.1 - Cost analysis Concept 1

Table D.1 presents the cost analysis of concept 1, which includes all components of the system.

Amount of modules		5					
Product	Supplier	Remarks	Amount	Price (€) incl. VAT	Subtotal (€) incl. VAT	URL	
Intel RealSense D435	Mouser		5	€186.08	€930.40	<a href="https://nl.mouser.com/ProductDetail/Intel/82635D435IDK5P?qs=PqoDHHvF64%252B5RxJ3DyHfHg%3D%3D">https://nl.mouser.com/ProductDetail/Intel/82635D435IDK5P?qs=PqoDHHvF64%252B5RxJ3DyHfHg%3D%3D</a>	
Sabrent 60W 7-Port USB 3.0 Hub + 3 Smart Charging Ports (60W 12V/5A external power adapter)	Amazon		1	€39.90	€39.90	<a href="https://www.amazon.com/gp/product/B0797NWDGB/">https://www.amazon.com/gp/product/B0797NWDGB/</a>	
Goobay USB-C 3.0 2.0m cables	Kabeltje.com		5	€12.99	€64.95	<a href="https://www.megekko.nl/product/3752/1037461/M-2-Behuizingen/ICY-BOX-IB-1817M-C31-externe-M-2-behuizing-USB-C-grjls">https://www.megekko.nl/product/3752/1037461/M-2-Behuizingen/ICY-BOX-IB-1817M-C31-externe-M-2-behuizing-USB-C-grjls</a>	
<b>Total module costs</b>					<b>€1,035.25</b>		
Product	Supplier	Remarks	Amount	Price (€) incl. VAT	Subtotal (€) incl. VAT	URL	
Intel i7 920	N/A	Price is from 2013. Not for sale anymore.	1	€260.00	€260.00	<a href="https://tweakers.net/pricewatch/248378/zotac-geforce-gtx260-amp.html">https://tweakers.net/pricewatch/248378/zotac-geforce-gtx260-amp.html</a>	
Asus P6T7 WS SuperComputer	N/A	Price is from 2013. Not for sale anymore.	1	€400.00	€400.00	<a href="https://tweakers.net/pricewatch/248378/zotac-geforce-gtx260-amp.html">https://tweakers.net/pricewatch/248378/zotac-geforce-gtx260-amp.html</a>	
Samsung Evo 850 SSD (1TB)	N/A		1	€103.00	€103.00	<a href="https://tweakers.net/pricewatch/422397/samsung-850-evo-1tb.html">https://tweakers.net/pricewatch/422397/samsung-850-evo-1tb.html</a>	
StarTech 2 Port PCI Express SuperSpeed USB 3.0 Card Adapter with UASP Support	Megekko		1	€35.95	€35.95	<a href="https://www.megekko.nl/product/2308/991106/USB-uitbreidingskaarten/StarTech-com-2-poorts-PCI-Express-PCI-e-Super-Speed-USB-3-0-kaartadapter-met-UASP-SATA-voeding">https://www.megekko.nl/product/2308/991106/USB-uitbreidingskaarten/StarTech-com-2-poorts-PCI-Express-PCI-e-Super-Speed-USB-3-0-kaartadapter-met-UASP-SATA-voeding</a>	
Startech 4 Port USB 3.1 PCI-e Card - 10Gbps PCI Express Expansion Card / Adapter	Megekko		1	€79.95	€79.95	<a href="https://www.megekko.nl/product/2308/991522/USB-uitbreidingskaarten/StarTech-com-4-poorts-PCI-Express-PCI-e-Super-Speed-USB-3-0-kaartadapter-met-2-speciale-5-Gbps-kanal">https://www.megekko.nl/product/2308/991522/USB-uitbreidingskaarten/StarTech-com-4-poorts-PCI-Express-PCI-e-Super-Speed-USB-3-0-kaartadapter-met-2-speciale-5-Gbps-kanal</a>	
Zotac Geforce GTX 260 Amp Graphics Card	N/A	Price is from 2012. Not for sale anymore.	1	€314.00	€314.00	<a href="https://tweakers.net/pricewatch/248378/zotac-geforce-gtx260-amp.html">https://tweakers.net/pricewatch/248378/zotac-geforce-gtx260-amp.html</a>	
Sweex Power Supply 650 W	N/A	Price is from 2012. Not for sale anymore.	1	€50.00	€50.00	<a href="https://tweakers.net/pricewatch/168868/sweex-power-supply-650w.html">https://tweakers.net/pricewatch/168868/sweex-power-supply-650w.html</a>	
<b>Total PC costs</b>					<b>€1,242.90</b>		
Product	Supplier	Remarks	Amount	Price (€) incl. VAT	Subtotal (€) incl. VAT	URL	
Aluminium profile - 1.11.050050.43L	Alucomp	Length: 400 mm	12	€15.34	€184.11	<a href="https://www.alucomp.nl/11105005043160-aluminium-profiel">https://www.alucomp.nl/11105005043160-aluminium-profiel</a>	
Aluminium profile - 1.11.050050.43L	Alucomp	Length: 500 mm	6	€18.72	€112.31	<a href="https://www.alucomp.nl/11105005043160-aluminium-profiel">https://www.alucomp.nl/11105005043160-aluminium-profiel</a>	
Aluminium profile - 1.11.050050.43L	Alucomp	Length: 600 mm	4	€22.09	€88.38	<a href="https://www.alucomp.nl/11105005043160-aluminium-profiel">https://www.alucomp.nl/11105005043160-aluminium-profiel</a>	
Aluminium profile - 1.11.050050.43L	Alucomp	Length: 1000 mm	4	€35.62	€142.49	<a href="https://www.alucomp.nl/11105005043160-aluminium-profiel">https://www.alucomp.nl/11105005043160-aluminium-profiel</a>	
Aluminium profile - 1.46.204.57571	Alucomp	Corner connector 57 x 57 mm)	24	€6.27	€150.43	<a href="https://www.alucomp.nl/14620438761-2">https://www.alucomp.nl/14620438761-2</a>	
Rose+Krieger Flange Brackets	DigiKey	Length: 40 mm	2	€6.13	€12.27	<a href="https://www.digikey.nl/product-detail/en/rose-krieger/4816702/1758-1019-ND/7200998">https://www.digikey.nl/product-detail/en/rose-krieger/4816702/1758-1019-ND/7200998</a>	
Rose+Krieger SLOT STONE F 30 MM, M5	DigiKey		48	€1.59	€76.08	<a href="https://www.digikey.nl/product-detail/en/rose-krieger/4006711/1758-1040-ND/7201019">https://www.digikey.nl/product-detail/en/rose-krieger/4006711/1758-1040-ND/7201019</a>	
Socket head M5 x 20 mm galvanized	Gamma	12 pieces per pack	1	€2.69	€2.69	<a href="https://www.gamma.nl/assortiment/gamma-inbusbout-m5-x-20-mm-cilinderkop-verzinkt-12-stuks/p/B458107">https://www.gamma.nl/assortiment/gamma-inbusbout-m5-x-20-mm-cilinderkop-verzinkt-12-stuks/p/B458107</a>	
12 mm tempered soda lime glass, 600 x 600 MM	Alkema Technical Glass Solutions	AGC 12 mm Planibel Clearvision glass - low iron concentration, with 92 % light transmission.	1	€105.00	€105.00	<a href="https://www.agc-yourglass.com/nl-BE/merken/planibel-extra-clear">https://www.agc-yourglass.com/nl-BE/merken/planibel-extra-clear</a>	
<b>Total embodiment costs</b>					<b>€873.77</b>		

Table D.2 - Cost analysis of concept 2, containing all components of the prototype.

## D.2 - Cost analysis Concept 2

Table D.2 presents the cost analysis of concept 2, which includes all components of the system.

# Appendix E - Prototyping showcase

Individual USB connection (PC with multiple USB)							
Mode	Bandwidth, Mbps	1 unit	2 units	3 units	4 units	5 units	6 units
Depth: 848x480, 90fps + Left Color: 848x480, 90fps	1172	1172	2345	3517	4689	5861	7034
Depth: 1280x720, 30fps + Left Color: RGB 1280x720, 30fps	885	885	1769	2654	3539	4424	5308
Depth: 1280x720, 30fps + Left Mono: RGB 1280x720, 30fps	664	664	1327	1991	2654	3318	3981
Depth-only: 848x480, 90fps	586	586	1172	1758	2345	2931	3517
Depth-only: 1280x720, 30fps	442	442	885	1327	1769	2212	2654
Depth: 840x480, 30fps + Left Color: Mono 848x480, 30fps	293	293	586	879	1172	1465	1758
Depth: 640x360, 30fps + Left Color: RGB 640x360, 30fps	221	221	442	664	885	1106	1327
Depth-only: 640x360, 30fps	111	111	221	332	442	553	664

Table E.1 - Bandwidth of PC with multiple USB connections. Hardware Sync is disabled (Intel Realsense, 2020).

## E.1 - Bandwidth limitations

The whitepaper of Intel on multi-camera-configurations (Grunnet-Jepsen et al., 2021) presents an analysis of the bandwidth when cameras are connected directly into a PC via USB. The data in Table E.1 shows possible configurations using USB 3.1 “SuperSpeed” connectivity, where green is successfully verified streaming, yellow indicates slightly reduced frame rate (i.e. frame drops occur), red indicates frame rate cut in half or none, and grey is not tested.

Testing with a setup of six cameras concludes a maximum camera configuration for all six cameras is limited to a resolution of 848 x 480 pixels and 30 fps, which amounts to a bandwidth of 1758 Mbps. Adding an additional seventh camera to the system with the same configuration resulted in all USB devices being disconnected and the need for a system reboot.

From the data presented in Table D.1, a connection of six cameras configured with a 848 x 480 resolution and 90 fps for both depth and color sensors, would theoretically maximize to a bandwidth of 7034 Mbps. Since the cameras are connected to USB 3.1, with a maximum allowable speed of 5 Gbps (in practice aim for a maximum of 3.2 Gbit/s) (Wikipedia, 2021), this configuration would not be possible if all cameras are connected to the same USB 3.1 port and USB port controller.

However, the StarTech USB 3.1 Gen 1 PCI expansion card

contains two independent USB channels, each with their own USB port controller. By distributing the cameras among the two independent channels, the total data throughput of the cameras is also distributed. In theory, this would allow for either better camera configuration with the same amount of cameras, or adding more cameras to the scanning system.

## E.2 - Camera power consumption

First testing with four cameras on a laptop (Dell XPS 15 9560, 2017, highest specifications) was done with a Goobay USB C hub with a max transfer speed of 5000 Mbps (5 Gbps), which provided a stable connection.

Connecting more than four cameras to the laptop or the custom-built floor computer caused the USB hub to disconnect. A possible explanation is that a single USB 3.1 port is able to provide a maximum voltage of 5.0 V and a current of 0.9 A. However, the Vision Processor D4 power consumption (which powers the camera modules) has a maximum nominal voltage of 3.3 V and a peak current of 0.2 A. Since a USB hub branches into multiple USB ports in parallel the voltage remains constant across all ports, but the total current is divided among the connected ports. If more than four cameras are connected, the USB 3.1 cannot accommodate the power consumption of these cameras, since the peak current is 1.0 A.

Introducing an external power supply to power the

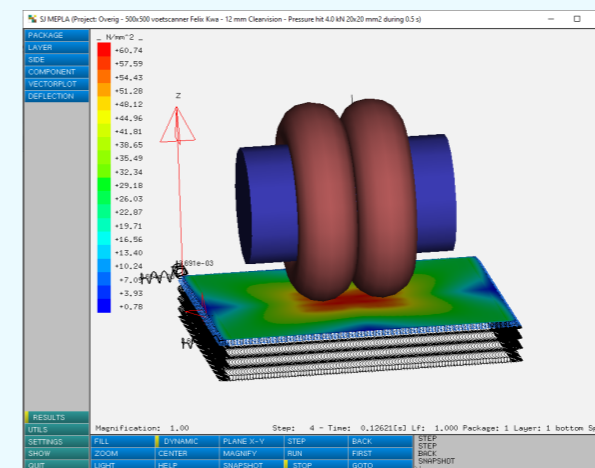
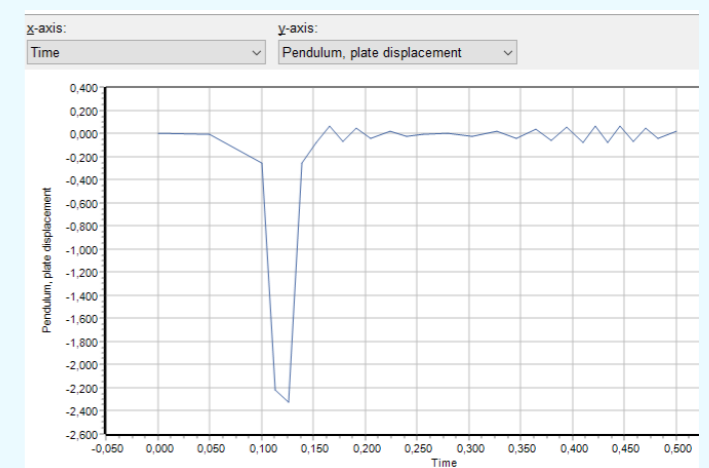


Figure E.1 - (left) a pendulum body with a mass of 200 kg. (right) the displacement (mm) of the glass.



connected devices of the USB 3.1 hub seems to give more stable connectivity and shows compatibility of up to seven scans. Intel’s whitepaper on multi-camera configurations (2020) also mentions the use of a powered USB hub, since each connected camera could in theory require up to 2 W per camera.

## E.3 - Scanning plate

M. Spijker (personal communication, 15 April, 2021), technical consultant glass at AGC, was able to assist in executing a force analysis of the glass plate to determine the specifications of the glass plate for two situations. The outcome of these force analyses is that a tempered glass plate of 12 mm (soda-lime glass) should be sufficient, since this type of glass can normally handle a load of approximately 90 N/mm<sup>2</sup>. The 90 N/mm<sup>2</sup> is including a so-called material safety factor, since tempered soda-lime glass can generally handle a load of 120 N/mm<sup>2</sup>.

The initial specifications for these simulations were based on the studies as previously mentioned in chapter 7.4:

- Glass plate dimensions: 50 x 50 cm
- Maximum load: 300 to 400 kg (including safety factor)
- Load duration: relatively short (0.5 s)
- Type of load: point load (at heel strike during the gait)

- Area of load: approximately 300 to 400 mm<sup>2</sup>

The first simulation is a dynamic calculation with a pendulum body of 200 kg (figure E.1, left). As can be observed in the figure, the maximum load that occurs is 60.74 N/mm<sup>2</sup>, which is well below the 90 N/mm<sup>2</sup> threshold. Also, the maximum displacement in the glass is about 2.3 mm in a time period of 0.1 seconds (figure E.1, right). This displacement is likely occurring when the patient is loading the glass with full weight between the heel strike and the foot-flat phase of the gait, since this stance has the highest distributed load. After this stance, the load does not increase, but the area does, which would result in a lower distributed load because the load area increases.

The second simulation that was done has a point load of 4000 N on an area of 20 x 20 mm (figure E.2) using AGC’s 12 mm Clearsight glass, which is AGC’s anti-reflective glass, used generally in windows and showcases (AGC Glass Europe, 2021). As shown in the figure E.2, the maximum load of the point load amounts to 66.80 N/mm<sup>2</sup>.

NB: The simulation was done with a load area size of 400 mm<sup>2</sup> (20 x 20 mm). However, according to the study of Strzalkowski et al. (2018), this should be 3000 to 4000 mm<sup>2</sup>, which is a factor ten larger. From this simulation, the assumption that the area load remains constant across the plate, and the heel area as indicated by Strzalkowski et al. (2018), the glass plate would be able to support

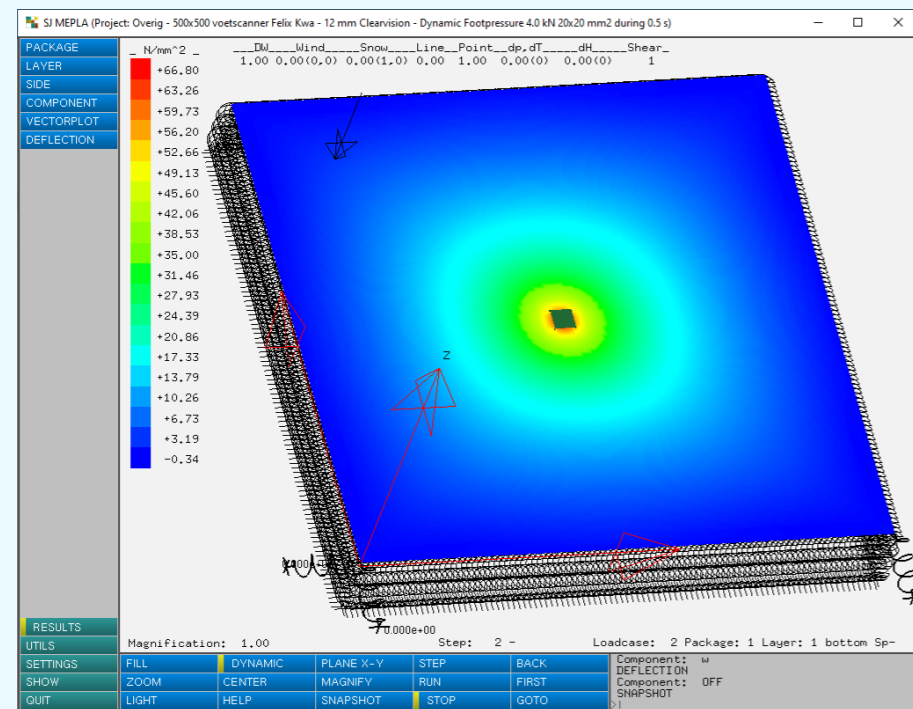


Figure E.2 - The force analysis done by M. Spijker, with a point load of 4000 N on an area of 20 x 20 mm.

2000 kg instead of 200 kg. From this, the conclusion can be made that 12 mm soda-lime glass will be more than sufficient to hold the load during a 4D foot scan.

**Choice of glass**

The simulation of M. Spijker considered soda-lime glass. Soda-lime glass is the most common form of produced glass. It generally consists of 70 - 75 % silicon dioxide (silica), 13 - 17 % sodium oxide (soda), and 5 - 10 % calcium oxide (lime) (Granta Edupack, 2021). This type of glass is known for its workability, which makes it highly suitable for manufacturing. Because soda-lime glass is widely used in many applications (e.g. windows, dinnerware, light bulbs, consumer glassware), the cost of soda-lime glass is relatively low compared to, for example, borosilicate glass.

Borosilicate glass is generally used in applications with chemicals because of its heat properties. It is also an appropriate material to be used in telescopic lenses, because of its low coefficient of thermal expansion, minimizing deformation of the glass which could distort the image. However, borosilicate glass is 3 to 4.5 times more expensive than soda-lime glass (not tempered) (Granta Edupack, 2021), and thermal expansion is not directly relevant in the case of 4D foot scanning.

Alternatives to glass are polycarbonate (PC) and polymethyl methacrylate (PMMA), which are materials that are generally 100 to 250 times stronger than glass, twice as light, and easier to machine (Granta Edupack, 2021). However, these materials are susceptible to scratches. Since the scanning plate is used to capture data of the foot, the plate should be as transparent as possible without artefacts disturbing the scanning quality. The expectation is that choosing softer materials such as PC or PMMA will scratch quickly and are not durable for the use of the scanner.

**Pricing**

Order size is important in reducing the pricing of glass. Manufacturers such as AGC Glass Europe are generally not able to produce the glass plate for the prototype, since their minimal order quantity (MOQ) is 500 pieces. Next to the MOQ, glass pricing depends on many other factors, such as:

- Type of glass (e.g. soda-lime glass or borosilicate glass)
- Thickness of the glass
- Dimensions of the glass
- Additional glass treatment (e.g. AR coating (anti reflective), glass tempering)

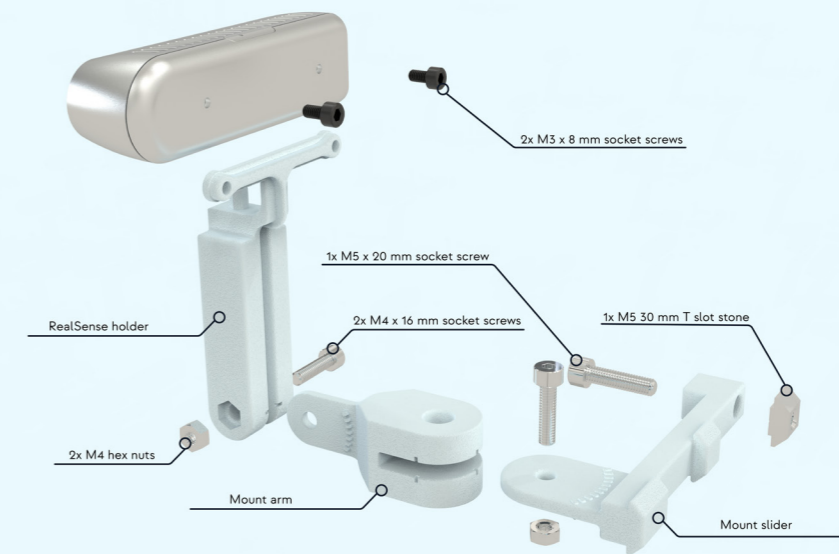


Figure E.3 - A render of the assembly of the camera mount with the components specified.

- Amount of layers of glass
- Type of adhesive to bond multiple layers of glass
- Post-production of glass
- Tolerances
- Specialized glass treatment

**Normative references**

The glass conforms to *ISO EN 572-1*, *EN 572-2* and *EN 572-9* standards. Also, CE-marking declarations are available. By conforming to CE-marking declarations, the glass plate can be easily used in the commercial development of the 4D foot scanner.

The glass is provided by ATGS (Alkema Technical Glass Solutions), who was able to acquire ClearVision low-iron glass from AGC's Planibel Extra Clear glass collection, which has a light transmission rate of 92 %. The glass plate has a nominal thickness of 12 ± 0.3 mm and a width and height of 600 ± 2 mm and 600 ± 3 mm, respectively.

There is a discrepancy between the dimensions of the glass plate in the simulations and in real life, with a difference of 100 mm for both the width and height of the plate. However, initial simulations with dimensions of 500 x 500 mm showed extremely durable results within the context of use.

**Treatment**

To make the glass harder and therefore more scratch resistant, the glass is tempered. The upside of using tempered glass is that it is safer in use. If the glass breaks, it breaks up into small blunt pieces, instead of large sharp glass shards. If the glass would ever happen to break in the middle of a data acquisition process where a person is standing on top of the glass, the glass would not be able to cut this person.

**E.4 - Custom camera mount**

The custom camera mount is designed to replace the existing ball mount that was initially used. This newly designed camera can be made using 3D printing and commodity fasteners.

As shown in figure E.3, the camera mount consists of three parts: a camera holder to position an Intel RealSense D4XX camera, an arm that extends the camera away from the frame, and a slider to attach the whole mount to the aluminium extrusion frame.

The three parts are connected to each other using M4 x 16 mm socket screws and M4 hex nuts that are integrated into the embodiment of the parts. The slider is fastened to the frame by a M5 30 mm T-slot stone and an M5 x 20 mm socket screw. The RealSense cameras are connected to the camera holder with 2x 8 mm M3 socket screws.

Comparison table - microcontrollers			
Specifications	Arduino Uno Rev3 (Arduino, 2021)	Arduino Nano 33 BLE Sense (Arduino, 2021)	Joy-IT NodeMCU ESP32 (Joy-IT, 2021)
Price (€) (Kiwi Electronics, July 2021)	€23.95	€27.00	€9.91
Processor	ATmega328	nRF52840	Tensilica LX6 Dual-Core
Operating Voltage	5 V	3.3 V (operable via 5 V microUSB)	3.3 V (operable via 5 V microUSB)
Clock speed	16 MHz	64 MHz	240 MHz
Flash Memory	32 kB	1 MB	4 MB
SRAM	2 kB	256 kB	512 kB

Table E.2 - A comparison table of the Arduino Uno Rev3, Arduino Nano & Joy-IT NodeMCU ESP32.

## E.5 - Human Computer Interaction (trigger system)

This appendix elaborates on the trigger system, including components selection, communication between the foot scanner system and the trigger system, the embodiment, and a preliminary bill of materials and cost overview. The recommendations section elaborates on possible development steps to be made when developing a commercial-ready 4D foot scanner.

### E.5.1 Component selection

#### Joy-IT NodeMCU ESP32

The ESP32 MCU is chosen over an Arduino Uno because of memory restrictions on the Arduino Uno. In the trigger system that is laid out in figure 11.10, the initialization and constant data fetching of the distance sensors occupy more than 80 % of the Arduino's dynamic memory capacity. Occupying this much of the dynamic memory capacity therefore results in no readable measurement values of the ToF sensors. This makes the serial implementation of the trigger system unusable.

Also, the tolerable clock speed (cycles per second of the CPU) of the ESP32 MCU (240 MHz) is 15 times faster than that of the Arduino Uno (16 MHz). Which means that the ESP32 would be able to react faster when motion is detected on the Time of Flight sensors.

Comparison table E.2 compares three microcontrollers: the Arduino Uno Rev3, the Joy-IT NodeMCU ESP32, and the Arduino Nano (which is more comparable to the ESP32 MCU). Making a selection based on clock speed and available flash memory, the ESP32 is preferred. Coincidentally, the price is almost 2.5 times lower than that of both the Arduino boards.

The ESP32 module that is used contains an ESP32-WROOM module. With this module, pins D21 and D22 contain SDA (serial data) and SCL (serial clock) functionality, respectively. These pins are used to establish an I2C connection with other devices and are directly connected to the TCA9548A MUX, as shown in figure E.3.

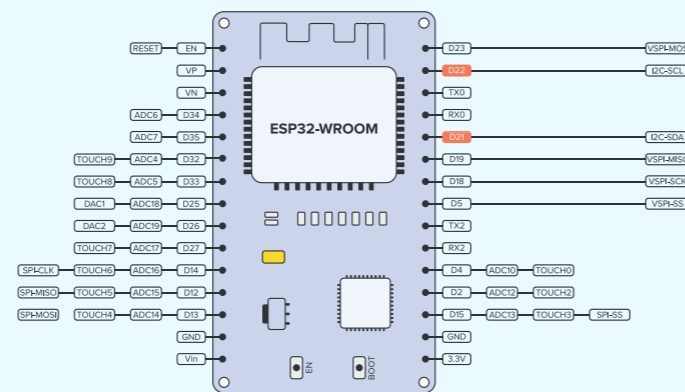


Figure E.3 - Pin layout of the ESP32-WROOM MCU, with the I2C ports (SDA and SCL) highlighted.

#### AdaFruit VL53L0X Time of Flight (ToF) distance sensors (30 to 1000 mm)

For prototyping purposes, the trigger system uses the readymade AdaFruit VL53L0X ToF distance sensors to detect motion on the walkway of the foot scanner setup. The VL53L0X ToF sensor utilizes infrared to detect distance. The Adafruit VL53L0X board, in combination with the open-source Adafruit VL53L0X library, is optimized to a response time of < 50 ms, thus allowing a frequency of 20 Hz.

#### Adafruit TCA9548A Multiplexer (MUX)

A downside of the Adafruit VL54L0X ToF sensor boards is that they all share the same I2C address. Thus, when connecting multiple sensors onto the same system over the same I2C bus, it is not possible to individually address them. The sensors have a feature to temporarily change the I2C address on initialization. However, with multiple sensors connected, this could be a potential bottleneck, such as resulting in inconsistent sensor order, which would cause incorrect behaviour of the trigger system.

Introducing a multiplexer (MUX) discards this bottleneck, since all sensors keep their original address and are physically connected to ports on the MUX. Therefore, the same order of sensors can always be assumed. The multiplexer is connected via I2C connection to the ESP32 and to both the ToF sensors. On runtime, the addressable ports of the MUX are switched, depending on the desired ToF sensor to read out.

### E.5.2 Communication

The communication between the trigger system and the 4DFS system is one-way, meaning that the trigger implementation works by sending data to the 4DFS system, without the need to receive data back.

Since the 4DFS system is written in Python but the trigger system is written in C++, the systems cannot natively communicate with each other. However, the serial connection between the ESP32 and the 4DFS system through the micro USB 2.0 connection can be used for communication. The benefit of using a serial connection is that it allows the 4DFS system to monitor the serial port to which the trigger system is connected. By sending data from the ESP32 through the serial connection, the 4DFS system is able to read in this data and act accordingly.

Maximizing the communication speed between the trigger system and the main operating system of the foot scanner is a priority. To maximize the allowable serial data transfer speed, the ESP32 is configured with a baud rate of 115200 Bd. Since the Arduino framework is used, 1 baud = 1 bit, resulting in a data rate of 115200 bits per second over the serial connection.

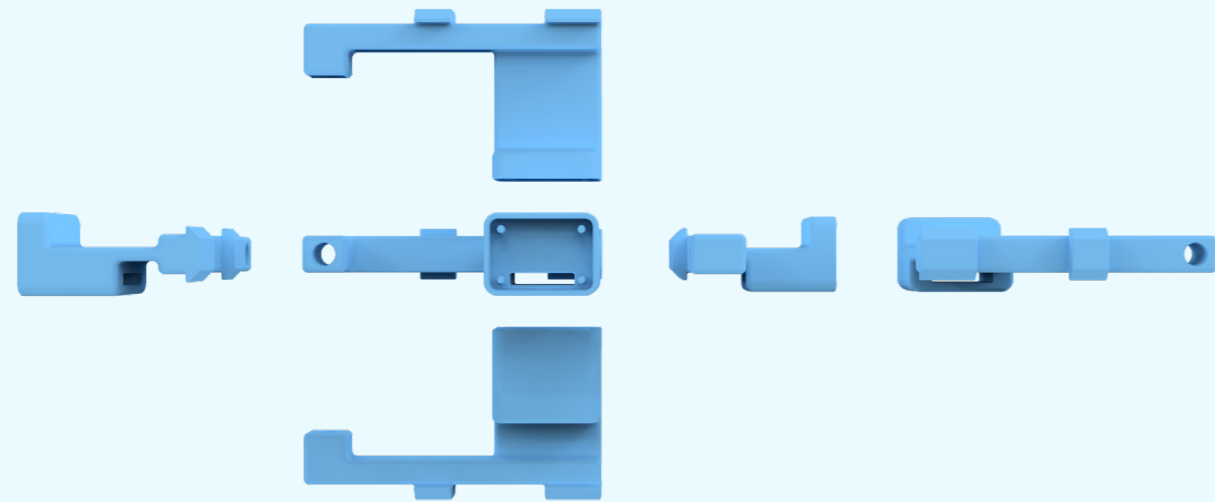


Figure E.4 - Orthogonal projection of the sensor housing.

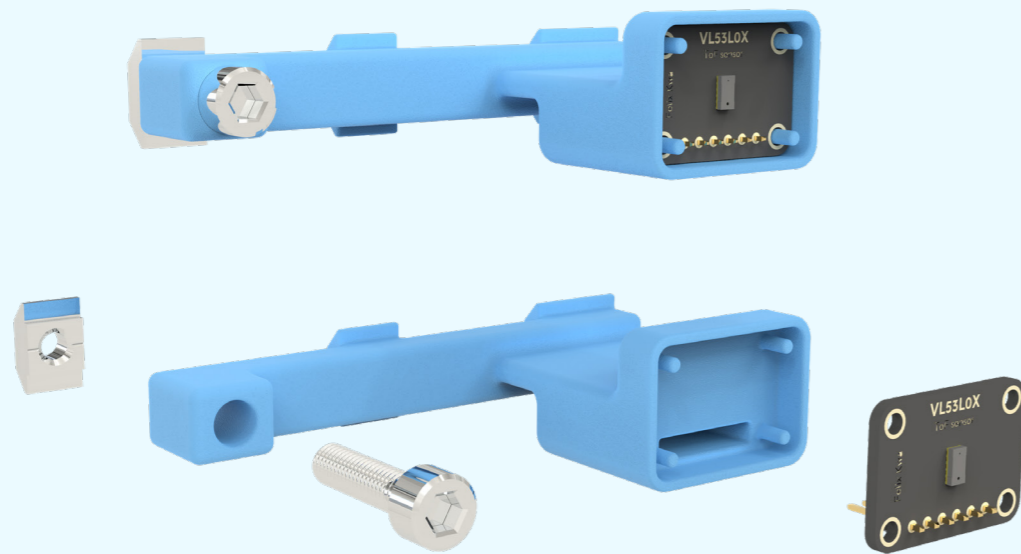


Figure E.5 - (top) The fully assembled sensor with all components. (bottom) An exploded view of the housing and all its components, excluding the 6 pin female connector.

### E.5.3 Embodiment

Figure E.4 showcases the sensor housing that is designed to hold the ToF sensors and to be attached to the T-slot aluminium profiles that hold the cameras. The ToF sensor is clamped with friction, without mechanical fixtures. The four pins in the housing help to align the ToF sensor during placement. The housing has room for the 6-pin female connector, which is used to connect the ToF board to the MUX.

Figure E.5 shows the assembled sensor including housing, sensor board, T-slot nut and M5 socket. The 6-pin female connector is excluded from this view.

The sensor mounts are designed in such a way that Adafruit's VL53L0X sensor board can be placed into the mount without additional mechanical fixtures. The mounts are designed to be 3D printed in one piece with support material, using Fused Deposition Modelling (FDM printing). The total print time is 3 hours and 13 minutes, with 10 % infill.

### BILL OF MATERIALS

Component	Comments	Supplier	Amount
VL53L0X Time of Flight sensor - 30 to 1000 mm range		Kiwi Electronics	2
Joy-IT Node MCU ESP32 module		Conrad	1
TCA9548A I2C Multiplexer		Kiwi Electronics	1
Custom housing	Custom made 3D printed housing which is mounted onto the aluminium profiles.	N/A	1
Socket head M5 x 20 mm galvanized	12 pieces per pack	Gamma	1
Rose+Krieger SLOT STONE F 30 MM, M5		DigiKey	1

Table E.3 - An overview of the Bill of Materials of the trigger system.

	Component	Comments	Supplier	Amount	Price (€) excl. VAT	Subtotal (€) excl. VAT	URL
HCI Trigger system	VL53L0X Time of Flight sensor - 30 to 1000 mm range		Kiwi Electronics	2	€14.83	€29.67	<a href="https://www.kiwi-electronics.nl/adafruit-vl53l0x-time-of-flight-distance-sensor-30-to-1000mm">https://www.kiwi-electronics.nl/adafruit-vl53l0x-time-of-flight-distance-sensor-30-to-1000mm</a>
	Joy-IT Node MCU ESP32 module		Conrad	1	€8.19	€8.19	<a href="https://www.conrad.nl/p/joy-it-node-mcu-esp32-modul-printplaat-voor-ontwikkelaars-1656367">https://www.conrad.nl/p/joy-it-node-mcu-esp32-modul-printplaat-voor-ontwikkelaars-1656367</a>
	TCA9548A I2C Multiplexer		Kiwi Electronics	1	€6.82	€6.82	<a href="https://www.kiwi-electronics.nl/tca9548a-i2c-multiplexer">https://www.kiwi-electronics.nl/tca9548a-i2c-multiplexer</a>
	Socket head M5 x 20 mm galvanized	12 pieces per pack	Gamma	1	€2.22	€2.22	<a href="https://www.gamma.nl/assortiment/gamma-inbusbout-m5-x-20-mm-cilinderkop-verzinkt-12-stuks/p/B458107">https://www.gamma.nl/assortiment/gamma-inbusbout-m5-x-20-mm-cilinderkop-verzinkt-12-stuks/p/B458107</a>
	Rose+Krieger SLOT STONE F 30 MM, M5		DigiKey	1	€1.31	€1.31	<a href="https://www.digikey.nl/product-detail/en/rose-krieger/4006711/1758-1040-ND/7201019">https://www.digikey.nl/product-detail/en/rose-krieger/4006711/1758-1040-ND/7201019</a>
<b>Total system costs</b>						<b>€48.21</b>	

Table E.4 - A cost overview of the trigger system.

### E.5.4 Bill of Materials & cost overview

The total component costs of the prototyped trigger system amounts to €44.68, excl. VAT (21 %). The Bill of Materials (BOM) and cost overview are presented in table E.3 and E.4, respectively. Since the proposal of this trigger system is for prototyping purposes, the custom 3D printed housing of the sensors is excluded from the costs. For development of the scanner as a commercial product, there are multiple manufacturing options for the sensor housings, depending on the series size; 3D printing, silicone molding, and injection molding.

The holder is a static object that is mounted onto the aluminium frame and is not mechanically challenged, since it only holds a weight of approximately 5 grams (Adafruit, 2021), including fixtures. Therefore, printing the mounts with Fused Deposition Modelling (FDM printing) will be sufficient and there is no need for more expensive 3D printing methods (such as stereolithography (SLA printing) or selective laser sintering (SLS printing)). Also, since there is no acting force from a particular direction, the anisotropic properties of FDM printing do not have to

be taken into account during manufacturing.

The downside of FDM printing (also with SLA printing, but not with SLS printing) is that the mount needs support structure, which results in post-processing after printing (cleaning up the support structure, sanding down the support structure marks). An option to overcome this costly process is to split the mount and optimize the design to be printed without support. The two halves can then be glued together with epoxy glue for a firm hold.

Generally, for small series sizes of 1 up to 100, 3D printing is a reasonable production method. For larger series sizes, silicone molding and injection molding is recommended. Silicone molding is highly suitable for small/medium sized batches (50 up to 1000). Injection molding tends to be more cost and time effective for larger series sizes (1000 and up).



Figure E.6 - The lighting experiment setup.

### E.5.5 Optimization recommendations

#### Embedded systems implementation

The implemented Time of Flight sensors are able to operate at a frequency of 20 Hz. A 20 Hz trigger is not ideal, since it could occur that a patient walks past the trigger without actually triggering the system. A faster trigger solution is desired when developing and optimizing the 4D foot scanner towards a commercial-ready solution. Or when implementing the trigger system as an embedded system of the whole 4D foot scanner.

An option is to replace the Adafruit VL53L0X board with an Pololu VL53L0X board, which is able to reach communication speeds of up to 400 kHz in I<sup>2</sup>C fast mode (Pololu, 2021).

Another option would be to use photodiodes instead of Time of Flight sensors, which are able to achieve response times at microseconds level (Hamamatsu, 2021).

#### Start camera streams directly via HW Sync

Currently, the trigger system sends out data to the serial port and the 4DFS system listens to this port. If there is activity, the 4DFS system responds accordingly. Because this connection is not optimized, the response time between triggering a sensor and the 4DFS system taking action is likely longer than 50 ms. With an embedded systems implementation, the trigger could be directly connected to the RealSense cameras via hardware synchronization (HW Sync). In combination with the aforementioned sensitive photodiode from Hamamatsu, this could be the fastest way of starting the data acquisition of the 4DFS system.

#### Custom PCB

The selected microcontroller is able to provide the functionalities that are needed to run this prototype, but also many more that will never be used (e.g. WiFi module, BLE module). Designing a custom PCB with the functionalities that are needed, such as an optimized chipset to handle fast rise times of photodiodes, not only provides better suited functionalities. In large order quantities, it will likely become cheaper than the € 9.91 per ESP32.

## E.6 - External lighting

#### Introduction

An experiment was done to explore the added value of adding external lighting to the volume of interest of the scanner and how brightness of external lighting influences the quality of the depth data. Also, the experiment is done to get a deeper understanding of the functionality of the depth sensors on the D435i camera. The results of this experiment setup are fundamental in establishing design considerations for the embodiment of the scanner and lighting requirements.

#### Method

The experiment was done with the depth sensors of a D435i camera, a 3D printed hand model that is painted in a skin-like tone and a Bresser SH-600 LED panel. To reflect the environment lighting, RGB photos were taken with an iPhone 12. The setup of this experiment is visualized in figure E.6.

The experiment consists of 22 iterations, where each iteration has different external lighting brightness

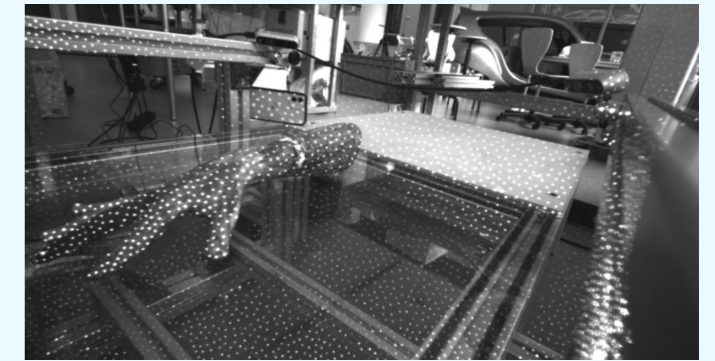
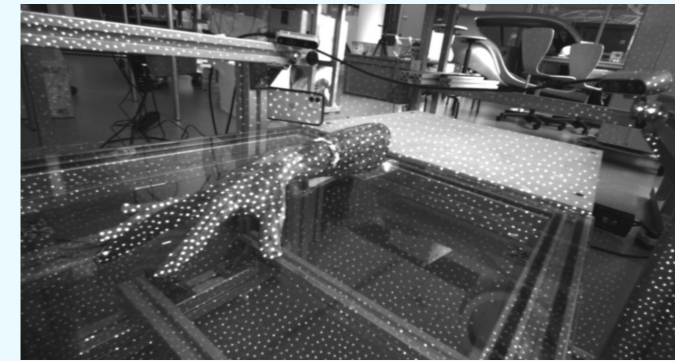


Figure E.7 - Iteration 0: Left and right depth sensor view, no added external light. The pseudo random pattern projected by the IR projector built into the RealSense cameras is quite distinguishable.

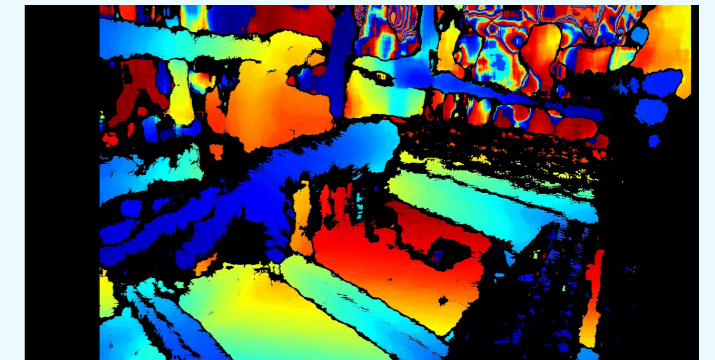


Figure E.8 - Iteration 0: (left) RGB image from iPhone. (right) depth image after StereoBM implementation. Model is recognizable without large random gaps in the depth data of the model.

measured in lux. The Bresser SH-600 LED panel has a maximum brightness of 5600 lux, and is adjustable between 10 and 100 % with a step size of 250 lux per step (21 steps in total).

For the first iteration, the LED panel is turned off. The second iteration has a brightness of 560 lux (10 % of max brightness). After the second iteration, every iteration has a brightness increment of 250 lux.

For every iteration in the experiment, an RGB photo is taken using the iPhone 12 to observe the change in lighting of the scene. Next to this, the left and right depth views of the D435i camera are captured and stored for data processing. The depth data of the camera is evaluated by implementation of OpenCV's stereo matching algorithm **stereoBM**, which takes both depth images (left and right view) as input.

#### Results

Figures E.7 through E.12 present the acquired data as prescribed in the method section for iterations 0, 10 and 22, which represent a brightness of 0 lux, 2810 lux (~ 50%) and 5600 lux (100 %), respectively.

At an additional external brightness of 0 lux, the pseudo random IR speckle pattern that is projected by the internal projector on the D435i camera is clearly visible in the 0th iteration and nicely spread out across the whole hand model. The depth image generated by the StereoBM implementation clearly shows most parts of the hand model. Also, the frame is clearly visible.

At a brightness of 2810 lux, the pseudo random IR speckle pattern becomes less visible on certain parts of the hand model. The depth data from the StereoBM evaluation shows gaps at the positions where the white spots are in the depth sensor views. The frame is still clearly visible.

At a brightness of 5600 lux, the pseudo random IR speckle pattern is not visible anymore at the front of the hand. A vague representation of the speckle pattern is visible at the back of the hand model. The depth image from the StereoBM evaluation shows large gaps in depth data at the front of the hand model. The frame is still clearly visible.

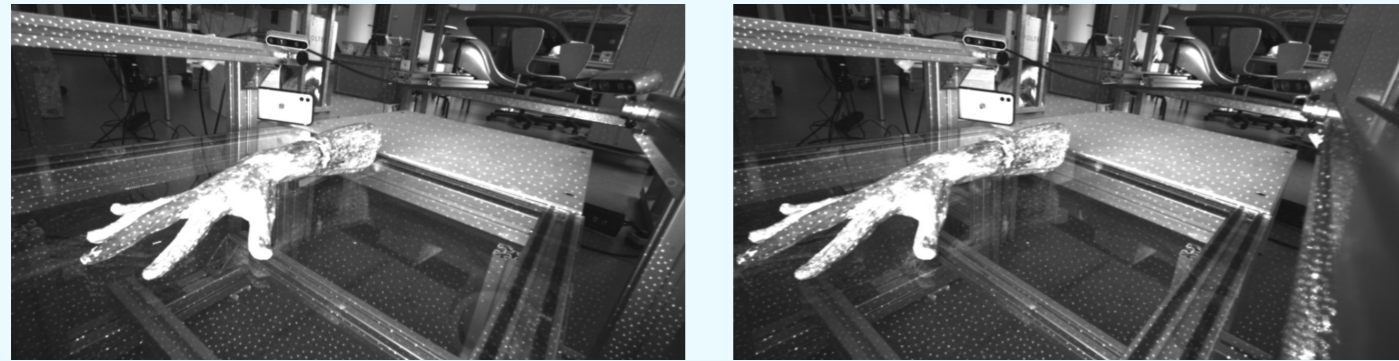


Figure E.9 - Iteration 10: Left and right depth sensor view, 50 % added external light (2810 lux). The external lighting causes white spots on the hand.

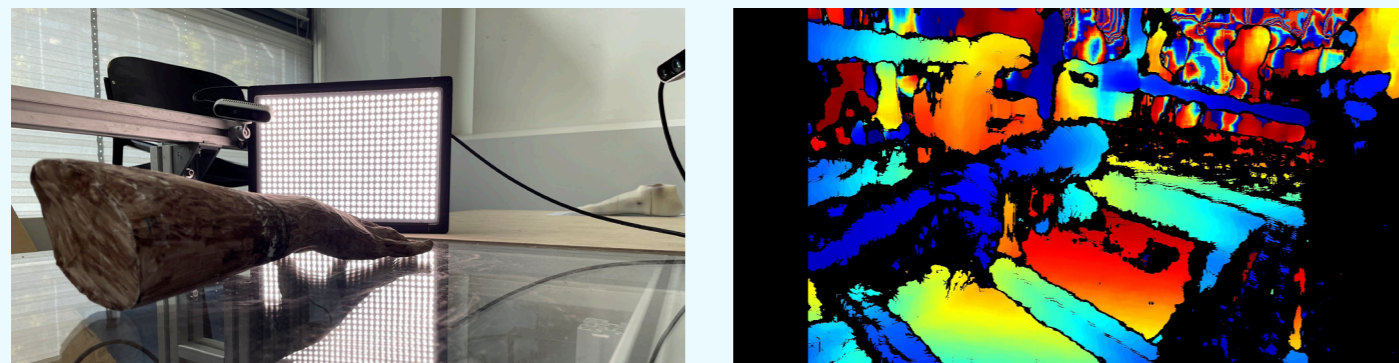


Figure E.10 - Iteration 10: (left) RGB image from iPhone. (right) depth image after StereoBM implementation. Model is recognizable but has small gaps in the depth data of the model that matches the location of the white spots from the depth sensor views.

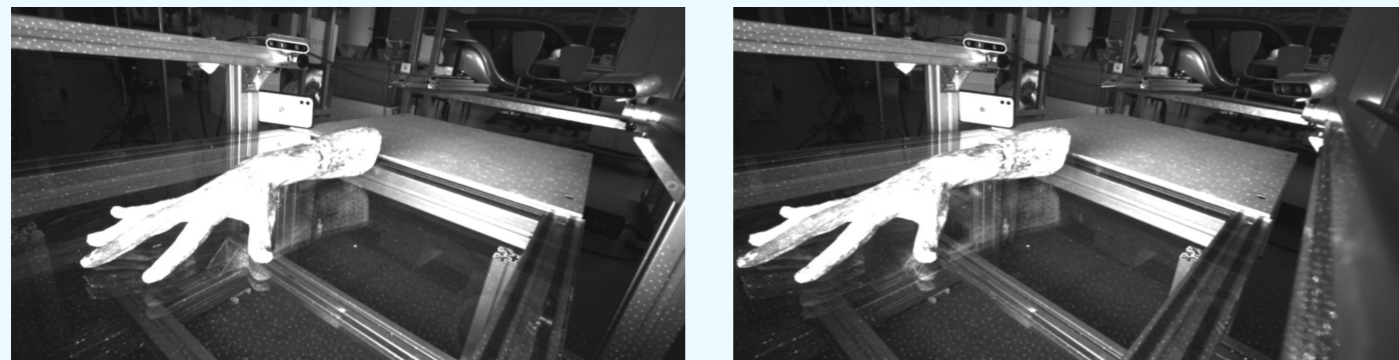


Figure E.11 - Iteration 22: Left and right depth sensor view, 100 % added external light (5600 lux). The projected IR pattern is almost completely faded and the hand model is overexposed by the external light source.

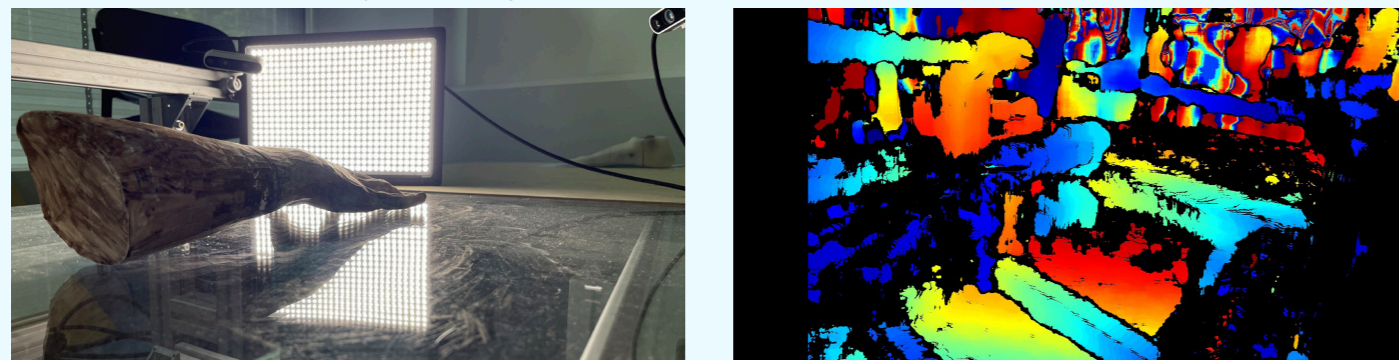


Figure E.12 - Iteration 11: (left) RGB image from iPhone. (right) depth image after StereoBM implementation. Model is hardly recognizable and contains large gaps in the depth data.

**Discussion**

The experiment gave four insights that were used in the design considerations of the final scanner:

1. **The camera needs a projected IR pattern to acquire depth data.**  
From the iterations, it becomes clear that visibility of the IR speckle pattern is important in the final depth data acquisition of the D435i camera.
2. **To maintain complete depth data, the additional light source must not contain an IR component.**  
Since the LED panel contains an IR component, it lights up the whole hand with IR lighting with increased brightness, covering the hand with IR light. The cameras are not able to perceive the depth of this area, which results in loss of depth data.
3. **The IR component of the LED panel only affects short distance depth data acquisition.**  
The depth images made with the StereoBM implementation showed a change in depth perception on the hand model. However, the frame and surroundings of the scanner remained clearly visible, even with the added 5600 lux lighting.
4. **The acrylate plate does not reflect IR lighting.**  
The depth images made with the StereoBM implementation clearly show the bottom part of the scanner's frame.

From the experiment we can conclude that the camera needs the projected IR pattern in order to retrieve proper depth data. If this pattern is blocked or is faded because there is too much IR lighting in the environment, the depth sensors are not able to retrieve clear depth data, which results in gaps in the depth image.

The IR component that is emitted by the LED panels causes the initial IR projection of the RealSense cameras to fade. The result is that the depth sensors of the RealSense cameras are not able to distinguish the IR projected pseudo random pattern on the scannable object, which results in gaps in the depth data, as shown in figure E.12.

The desirability to add external IR projectors to each camera is supported by Intel RealSense (2020), stating that the depth perception of the cameras is highly improved with an additional external pseudo random IR pattern projector. Insight 1 can support this statement.

With this experiment, the hand model was positioned on top of a transparent acrylic plate. To gain knowledge about the IR reflective properties of the glass plate that is used in the final scanner, a similar experiment could be repeated.

**E.7 - Cost analysis**

Table E.5 presents the cost analysis of the developed prototype that is presented in chapter 10. The overview includes the biggest tested camera configuration, which includes 7 Intel RealSense D435i cameras, and 2 Intel RealSense D415 modules, including 50-pin rigid interposer and Vision Processor D4 board. As with concepts 1 and 2, the prices of the Desktop PC components are indicated by their last retail price.



Amount of modules		9					
Product	Supplier	Remarks	Amount	Price (€) incl. VAT	Subtotal (€) incl. VAT	URL	
Intel RealSense D435	Mouser		7	€186.08	€1,302.56	<a href="https://nl.mouser.com/ProductDetail/Intel/82635D435DK5P?qs=PqoDHHvF64%252B5R%3DyHfg%3D%3D">https://nl.mouser.com/ProductDetail/Intel/82635D435DK5P?qs=PqoDHHvF64%252B5R%3DyHfg%3D%3D</a>	
Intel RealSense D415 module	Mouser		2	€58.44	€116.88	<a href="https://nl.mouser.com/ProductDetail/Intel/82635DSASRCPRQ?qs=w%2FvICP2dgr%2FNFDC8oSpw%3D%3D">https://nl.mouser.com/ProductDetail/Intel/82635DSASRCPRQ?qs=w%2FvICP2dgr%2FNFDC8oSpw%3D%3D</a>	
Intel RealSense 50-pin rigid interposer	Mouser		2	€8.47	€16.94	<a href="https://nl.mouser.com/ProductDetail/607-82635DSITR50P">https://nl.mouser.com/ProductDetail/607-82635DSITR50P</a>	
Intel RealSense Vision D4 processor board	Mouser		2	€29.65	€59.30	<a href="https://nl.mouser.com/ProductDetail/Intel/82635DSASRCPRQ?qs=w%2FvICP2dgr%2FNFDC8oSpw%3D%3D">https://nl.mouser.com/ProductDetail/Intel/82635DSASRCPRQ?qs=w%2FvICP2dgr%2FNFDC8oSpw%3D%3D</a>	
Sabrent 60W 7-Port USB 3.0 Hub + 3 Smart Charging Ports (60W 12V/5A external power adapter)	Amazon		2	€39.90	€79.80	<a href="https://www.amazon.com/gp/product/B0797NWDDB/">https://www.amazon.com/gp/product/B0797NWDDB/</a>	
Goobay USB-C 3.0 2.0m cables	Kabeltje.com		9	€12.99	€116.91	<a href="https://www.megekko.nl/product/3752/1037461/M-2-Behuizingen/CY-BOX-IB-1817M-C31-externe-M-2-behuizing-USB-C-grjls">https://www.megekko.nl/product/3752/1037461/M-2-Behuizingen/CY-BOX-IB-1817M-C31-externe-M-2-behuizing-USB-C-grjls</a>	
<b>Total module costs</b>					<b>€1,692.39</b>		
Product	Supplier	Remarks	Amount	Price (€) incl. VAT	Subtotal (€) incl. VAT	URL	
Intel i7 920	N/A	Price is from 2013. Not for sale anymore.	1	€260.00	€260.00	<a href="https://tweakers.net/pricewatch/248378/zotac-geforce-gtx260-amp.html">https://tweakers.net/pricewatch/248378/zotac-geforce-gtx260-amp.html</a>	
Asus P6T7 WS SuperComputer	N/A	Price is from 2013. Not for sale anymore.	1	€400.00	€400.00	<a href="https://tweakers.net/pricewatch/248378/zotac-geforce-gtx260-amp.html">https://tweakers.net/pricewatch/248378/zotac-geforce-gtx260-amp.html</a>	
Samsung Evo 850 SSD (1TB)	N/A		1	€103.00	€103.00	<a href="https://tweakers.net/pricewatch/422397/samsung-850-evo-1tb.html">https://tweakers.net/pricewatch/422397/samsung-850-evo-1tb.html</a>	
StarTech 2 Port PCI Express SuperSpeed USB 3.0 Card Adapter with UASP Support	Megekko		1	€35.95	€35.95	<a href="https://www.megekko.nl/product/2308/991106/USB-uitbreidingskaarten/StarTech-com-2-poorts-PCI-Express-PCIe-SuperSpeed-USB-3-0-kaartadapter-met-UASP-SATA-voeding">https://www.megekko.nl/product/2308/991106/USB-uitbreidingskaarten/StarTech-com-2-poorts-PCI-Express-PCIe-SuperSpeed-USB-3-0-kaartadapter-met-UASP-SATA-voeding</a>	
Startech 4 Port USB 3.1 PCIe Card - 10Gbps PCI Express Expansion Card / Adapter	Megekko		1	€79.95	€79.95	<a href="https://www.megekko.nl/product/2308/99152/USB-uitbreidingskaarten/StarTech-com-4-poorts-PCI-Express-PCIe-SuperSpeed-USB-3-0-kaartadapter-met-2-speciale-5-Gbps-kanal">https://www.megekko.nl/product/2308/99152/USB-uitbreidingskaarten/StarTech-com-4-poorts-PCI-Express-PCIe-SuperSpeed-USB-3-0-kaartadapter-met-2-speciale-5-Gbps-kanal</a>	
Zotac Geforce GTX 260 Amp Graphics Card	N/A	Price is from 2012. Not for sale anymore.	1	€314.00	€314.00	<a href="https://tweakers.net/pricewatch/248378/zotac-geforce-gtx260-amp.html">https://tweakers.net/pricewatch/248378/zotac-geforce-gtx260-amp.html</a>	
Sweex Power Supply 650 W	N/A	Price is from 2012. Not for sale anymore.	1	€50.00	€50.00	<a href="https://tweakers.net/pricewatch/168868/sweex-power-supply-650w.html">https://tweakers.net/pricewatch/168868/sweex-power-supply-650w.html</a>	
<b>Total PC costs</b>					<b>€1,242.90</b>		
Product	Supplier	Remarks	Amount	Price (€) incl. VAT	Subtotal (€) incl. VAT	URL	
Aluminium profile - 1.11.050050.43L	Alucomp	Length: 400 mm	12	€15.34	€184.11	<a href="https://www.alucomp.nl/11105005043160-aluminium-profiel">https://www.alucomp.nl/11105005043160-aluminium-profiel</a>	
Aluminium profile - 1.11.050050.43L	Alucomp	Length: 500 mm	6	€18.72	€112.31	<a href="https://www.alucomp.nl/11105005043160-aluminium-profiel">https://www.alucomp.nl/11105005043160-aluminium-profiel</a>	
Aluminium profile - 1.11.050050.43L	Alucomp	Length: 600 mm	4	€22.09	€88.38	<a href="https://www.alucomp.nl/11105005043160-aluminium-profiel">https://www.alucomp.nl/11105005043160-aluminium-profiel</a>	
Aluminium profile - 1.11.050050.43L	Alucomp	Length: 1000 mm	4	€35.62	€142.49	<a href="https://www.alucomp.nl/11105005043160-aluminium-profiel">https://www.alucomp.nl/11105005043160-aluminium-profiel</a>	
Aluminium profile - 1.46.204.57571	Alucomp	Corner connector 57 x 57 mm)	24	€6.27	€150.43	<a href="https://www.alucomp.nl/14620438761-2">https://www.alucomp.nl/14620438761-2</a>	
Rose+Krieger Flange Brackets	DigiKey	Length: 40 mm	2	€6.13	€12.27	<a href="https://www.digikey.nl/product-detail/en/rose-krieger/4816702/1758-1019-ND/7200998">https://www.digikey.nl/product-detail/en/rose-krieger/4816702/1758-1019-ND/7200998</a>	
Rose+Krieger SLOT STONE F 30 MM, M5	DigiKey		48	€1.59	€76.08	<a href="https://www.digikey.nl/product-detail/en/rose-krieger/4006711/1758-1040-ND/7201019">https://www.digikey.nl/product-detail/en/rose-krieger/4006711/1758-1040-ND/7201019</a>	
Socket head M5 x 20 mm galvanized	Gamma	12 pieces per pack	1	€2.69	€2.69	<a href="https://www.gamma.nl/assortiment/gamma-inbusbout-m5-x-20-mm-cilinderkop-verzinkt-12-stuks/p/B458107">https://www.gamma.nl/assortiment/gamma-inbusbout-m5-x-20-mm-cilinderkop-verzinkt-12-stuks/p/B458107</a>	
12 mm tempered soda lime glass, 600 x 600 MM	Alkema Technical Glass Solutions	AGC 12 mm Planibel Clearvision glass - low iron concentration, with 92 % light transmission.	1	€105.00	€105.00	<a href="https://www.agc-yourglass.com/nl-BE/merken/planibel-extra-clear">https://www.agc-yourglass.com/nl-BE/merken/planibel-extra-clear</a>	
<b>Total embodiment costs</b>					<b>€873.77</b>		
<b>Total prototype cost</b>					<b>€3,809.06</b>		

Table E.5 - Cost analysis of the presented prototype, containing all components of the prototype.

# Appendix F - Data acquisition evaluation

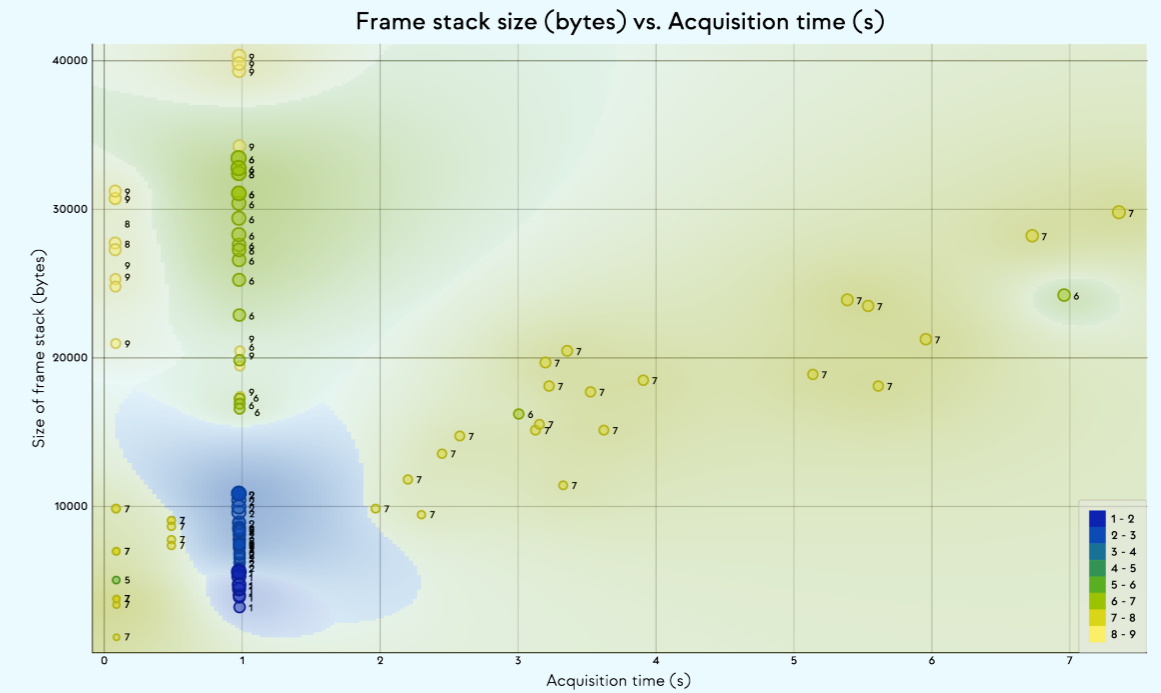


Figure F.1 - A scatterplot of the frame stack size (in bytes) with respect to the acquisition time (in seconds). The colour and labels of the data points represent the amount of connected cameras.

## Appendix F.1 Memory analysis

### Frame stack size (in bytes) vs. Acquisition time (s)

As can be expected from the plot in figure F.1, when more cameras are connected to the system and are used in the data acquisition process, more data is acquired and thus more memory is used.

From the plot in figure F.1, it seems that the memory occupation due to the size of the frame stack is predominantly determined by the number of cameras that are connected to the system. At t = 1 s, clear clusters can be made between the acquisitions with 1 and 2 cameras, and the rest. Remarkable is that the frame stack size with 6 and 9 cameras at this acquisition time varies and shows divergent behaviour.

Focussing only on acquisitions done with 7 cameras, a linear increase in frame stack size can be spotted over time. Figure F.2 shows a regression line that is calculated

over all the associated data points for 7 Intel RealSense cameras. The regression line is a best-fitting line representation of the data on the x-axis (X) and y-axis (Y). It is calculated by:

$$y = mx + b \quad (\text{Eq. F.1})$$

The formula of the slope, m, of the best-fitting line is:

$$m = r \left( \frac{s_y}{s_x} \right) \quad (\text{Eq. F.2})$$

Where r denotes the correlation coefficient between the X and Y. Variables  $s_x$  and  $s_y$  represent the point standard deviations of the x- and y-values, respectively. With  $r = 1.00$ , there is a one-to-one correlation between X and Y, and unknown data can be easily projected.

As figure F.2 shows, the value for r is 0.96, which

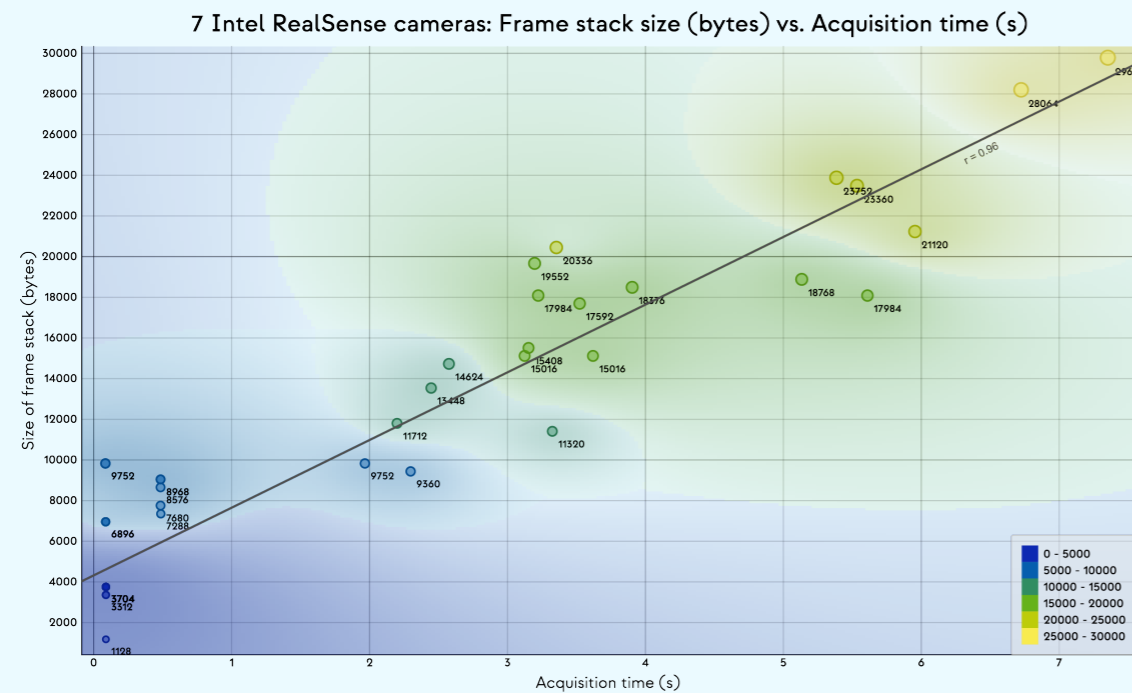


Figure F.2 - A scatterplot of the frame stack size (in bytes) with respect to the acquisition time (in seconds) for only 7 cameras. The colour and labels of the data points represent the amount of connected cameras.

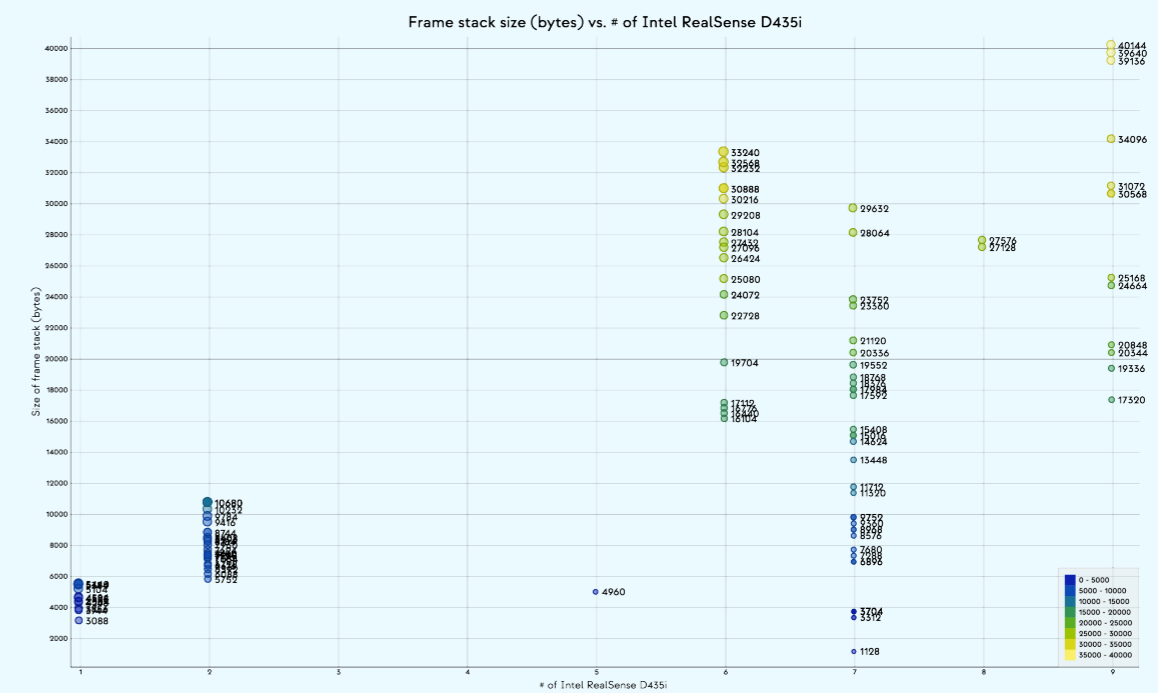


Figure F.3 - A scatterplot of the frame stack size (in bytes) with respect to the number of cameras. The colour of the data points represents the amount of connected cameras. The labels of the data points represent the frame stack size in bytes.

indicates that there is a high correlation between X and Y. Thus, it is possible to estimate a projection of the frame stack size of a data acquisition run with variable acquisition time with relatively large likelihood. This is useful when determining the amount of needed memory for the scanner system, depending on the desired acquisition time.

Unfortunately, the memory analysis does not include a large sample size with larger variation in acquisition time for all other camera configurations.

**Frame stack size (in bytes) vs. Number of cameras**

Figure F.3 clearly shows an increase in frame stack size for each added camera, with a maximum frame stack size of 40144 bytes, which is 40 MB of memory occupancy. Since not all acquisition times for all camera configurations are included in the memory analysis, no conclusions can be made from this plot exclusively. However, when combining this plot data with the plot from figure F.1, it becomes clear that an increase in

cameras does not show an intuitive increase in frame stack size. Since the configurations with 6 and 8 cameras show different behaviour in memory usage than the configuration with 7 cameras.

**Number of frames vs. Acquisition time (s)**

Figure F.4 does not include the frame stack size in bytes. What it does show is the number of frames that is returned over time for different camera configurations.

The configuration with 7 cameras shows behaviour that can be expected: the longer the acquisition time is, the more frames are acquired. The plot is similar to that of figure F.2, also following a linear trend.

It is interesting to observe the data points at t = 1, since most acquisitions with different camera configurations are made at this value for X. Notable is that the configuration with 9 cameras returns the least amount of frames, even though the sensor resolution and frame rate for this camera configuration is the same as that for the other

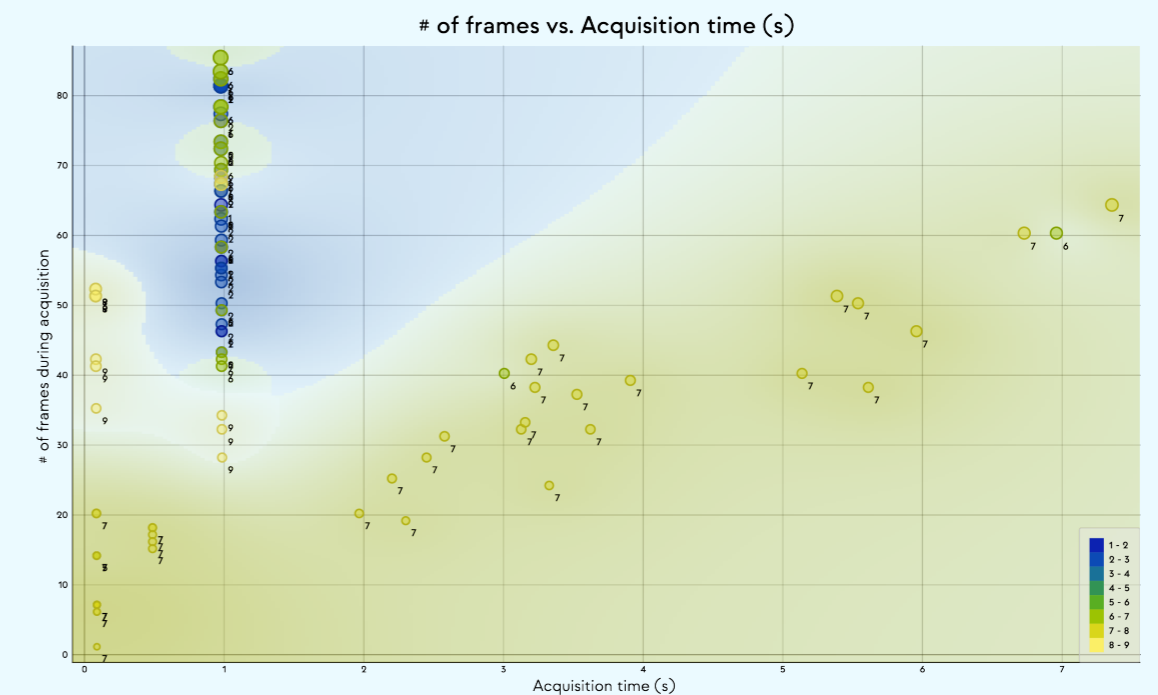


Figure F.4 - A scatterplot of the number of frames with respect to the acquisition time (in seconds). The colour and labels of the data points represent the amount of connected cameras.

camera configurations. Furthermore, it is curious that the camera configuration with 6 cameras is able to output more frames than a configuration with 1 or 2 cameras.

**Appendix F.2 Dynamic acquisition time**

Table F.1 contains all the obtained dynamic scan data.

# Appendix G - Data processing

Below are the transformation matrices that were used for rough alignment of the foot scans to prepare for nonrigid ICP registration.

```
T_C(1) = [-0.86 -0.46 0.22 0.3;...
-0.23 0.74 0.63 0.49;...
-0.45 0.49 -0.75 -0.97;...
0 0 0 1]; % Cam 1
T_C(2) = [-0.83 -0.14 -0.55 -0.12;...
-0.36 0.87 0.32 0.16;...
0.43 0.47 -0.77 -0.78;...
0 0 0 1]; % Cam 2
T_C(3) = [-0.92 -0.4 0.01 0.02;...
-0.24 0.57 0.79 0.4;...
-0.32 0.72 -0.62 -0.8;...
0 0 0 1]; % Cam 3
T_C(4) = [-0.43 -0.09 -0.09 -0.33;...
-0.2 0.98 0 0.07;...
0.88 0.18 -0.44 -0.87;...
0 0 0 1]; % Cam 4
T_C(5) = [0.99 0.03 -0.12 -0.06;...
-0.04 1 -0.05 -0.01;...
0.11 0.06 0.99 -0.02;...
0 0 0 1]; % Cam 5
T_C(6) = [0.99 0.15 -0.05 0.01;...
-0.16 0.98 -0.1 -0.03;...
0.04 0.11 0.99 -0.04;...
0 0 0 1]; % Cam 5
T_C(7) = [0.45 -0.86 0.25 0.13;...
-0.2 -0.37 -0.91 -0.29;...
0.87 0.36 -0.34 -0.64;...
0 0 0 1]; % cam 0
```

# Appendix H - Camera calibration proposal

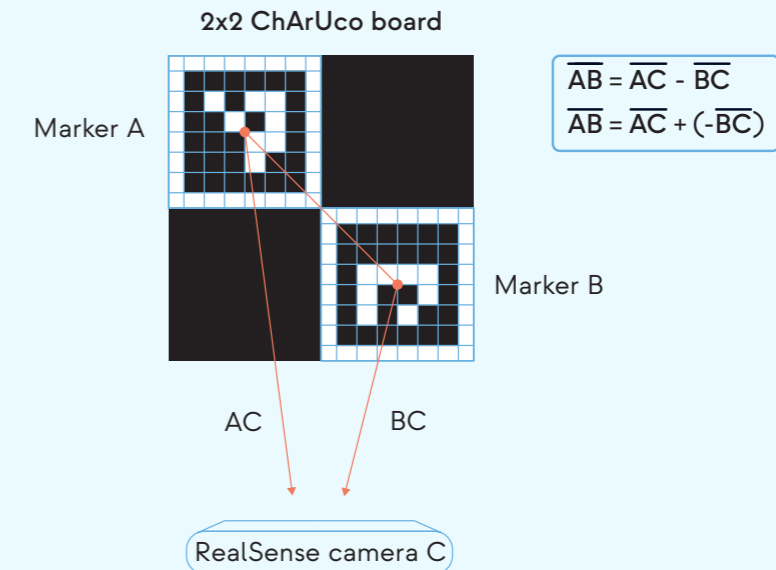


Figure H.1 - A visualization of minimizing the error between marker detection of individual markers.

```
For each camera pair in the system:
  For each camera in a camera pair (c_1, c_2):
    Do detectMarkers() to detect.
    For each detected 2x2 ArUco board:
      Do estimatePoseSingleMarkers() to receive extrinsic camera parameters.
      Calculate BC from AB = AC + (-BC) using Rodrigues Angles to convert the
      rotation vector to matrix form.
      if || Calc(BC)-BC || < threshold: continue
    For each unique markers shared by pair (c_1, c_2):
      Solve PnP problem (Perspective-n-Point) for this marker to acquire transformation
      matrix T.
      Optimize cost function J to find the optimal T.
      Define T with smallest error as transformation matrix T for pair.
    if global error between camera pairs < threshold: return
```

Figure H.2 - Pseudocode of the optimized calibration algorithm draft.

With the proposed closed-loop calibration method, the goal is to minimize the global calibration error of the camera configuration in three steps:

1. **Minimize the error in determining the extrinsic parameters of a camera** - Minimizing the error between the detection of the individual markers can be done since the distance of the marker centers is a known variable. By calculating vector AC, vector BC can be calculated. However, since the camera is not likely to be positioned perpendicular to the markers, the vectors have to be corrected using Rodrigues' Rotation formula.

Using this, the vectors can be properly subtracted and BC can be calculated. This approach is visualized in figure H.1.

2. **Minimize the error of the transformation matrix between camera 1 and camera 2** - The error can be minimized by optimizing a cost function to find the optimal transformation matrix.
3. **Making use of the closed loop system to converge the global error to a minimum** - Pairs can be optimized if they do not match the global error with a certain threshold.